

Chapter 5

Sintering and Densification

(I)—Conventional Sintering Technologies

5.1 Introduction

It is well known that, to produce ceramics, green bodies must be sintered at a certain high temperature for a given time duration to develop required microstructure and thus desired properties. In particular, transparent ceramics must be fully dense to achieve maximum optical transmittance. Sintering process is governed by a number of parameters, which can be used to build up interrelationships among processing, microstructure, properties, and performance. Sintering behavior and microstructure development have been extensively studied. Qualitative understandings include driving forces of sintering, the mechanisms of densification, controlling factors, such as particle size of precursor powders, sintering temperature, time duration and applied pressure, electrical current, and so on.

Thermodynamics indicates that, during sintering process, there is always a decrease in the free energy of the system. Driving forces of sintering are mainly derived from the curvature of free surfaces of the precursor powders. External pressures if applied could also be important driving force. Kinetics of matter transport is concerned, because it determines the sintering time. Matter transport takes place predominantly through the diffusion of atoms, ions or other charged species. The paths of diffusion, corresponding to the mechanisms of diffusion, determine the mechanisms of the sintering. The rate of diffusion is controlled the type and concentration of defects. In this respect, defect chemistry, including defect structures and concentrations of the defect, is an important subject related to sintering. It is also necessary to predict the defect chemistry for different sintering conditions, such as temperature, gaseous atmosphere and dopants. Fundamentals of sintering of ceramics have been described systematically in the literature [1–18].

5.2 Fundamental Aspects of Sintering

5.2.1 Driving Forces of Sintering

Sintering process is an irreversible process, during which the free energy of the system is decreased. The sources responsible for such a decrease are called the driving forces of sintering. There are three potential driving forces, (i) the curvature of particle surfaces, (ii) externally applied pressure, and (iii) chemical reaction.

5.2.1.1 Surface Curvature

Surface curvature is always present as the driving force of sintering, while external stress and chemical reaction may be absent. Therefore, surface curvature is the primary driving force of sintering. For one mole of ceramic powder, comprising of spherical particles with a radius a , the number of particles is given by:

$$N = \frac{3M}{4\pi a^3 \rho} = \frac{3V_m}{4\pi a^3}, \quad (5.1)$$

where ρ is density of the particles (materials), which are assumed to be pore-free, M is molecular weight and V_m is molar volume. The surface area of the powder is given by:

$$S_A = 4\pi a^2 N = \frac{3V_m}{a}. \quad (5.2)$$

If γ_{SV} is used to stand for the specific surface energy, i.e., the surface energy per unit area, of the particles, the surface free energy of the powder can be calculated by:

$$E_S = \frac{3\gamma_{SV} V_m}{a}. \quad (5.3)$$

Therefore, E_S is the quantity of the decrease in surface free energy of the powder, if a fully dense body is formed from the one mole of particles, i.e., it is the driving force of sintering.

5.2.1.2 External Pressure

External pressure can be applied to provide the driving force for sintering in addition to surface curvature, which could be comparatively smaller in this case. The pressure should be applied during the key state of sintering. There are two ways to apply pressure: hot pressing and hot isostatic pressing. By applying an external

pressure, work is done on compact of the powder. For 1 mol of particles, the work done on the compact can be estimated by:

$$W = p_a V_m, \quad (5.4)$$

where p_a is the applied pressure and V_m is molar volume of the materials. W represents the driving force for densification due to the application of an external pressure.

5.2.1.3 Chemical Reaction

Chemical reactions can provide driving force for sintering only when they have contribution to the densification process. The change in free energy of a chemical reaction is given by

$$\Delta G^0 = -RT \ln K_{eq}, \quad (5.5)$$

where R is the gas constant (8.3 J mol^{-1}), T is the absolute temperature, and K_{eq} is the equilibrium constant of the reaction. The value is much higher than the driving force of external pressure.

5.2.2 Defects in Crystalline Solids

The driving forces for sintering are attributed to the transport of matter, through the diffusion of atoms, ions or molecules in crystalline solids, due to the presence of various defects related to their structural imperfections. Properties and concentrations of defects control the rates of matter transport and thus determine the rates of processes, such as sintering, grain growth, and creep. The presence of defects in crystalline solids has structural reasons, i.e., the atoms or ions are not arranged in their lattice sites, and chemical reasons, i.e., the deviation from the stoichiometric composition. Structural defects in crystalline solids can be classified into three groups: (i) point defects, (ii) line defects, and (iii) planar defects. Point defects are associated with one lattice site and its close surroundings, such as missing atoms called vacancies, interstitial atoms at the interstices between atoms, and substitutional atoms on the sites that would normally be occupied by other types of atoms, as shown schematically in Fig. 5.1 for an elemental solid, e.g., pure metal [1]. The point defects in pure crystals, i.e., vacancies and interstitials, are called intrinsic or native defects. Because ceramics can be treated as ionic solids, point defects have more contributions than others to the defect chemistry.

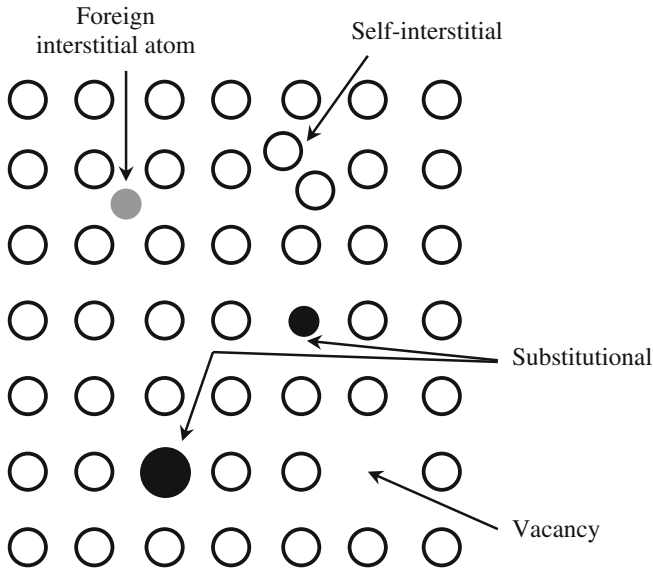


Fig. 5.1 Schematic showing various types of point defects in an elemental solid. Reproduced with permission from [1]. Copyright © 2003, CRC Press

5.2.2.1 Point Defects and Defect Chemistry

Defects in ceramics can be charged, which are different from those in metals. For a simple pure ionic oxide, with a stoichiometric formula of MO , consisting of a metal (M) with valence of $+2$ and an oxygen (O) with valence of -2 , the types of point defects could be vacancies and interstitials of both the M and O , which can be either charged or neutral. Besides the single defects, it is also possible for the defects to associate with one another to form defect clusters. Electronic defects or valence defects, consisting of quasi-free electrons or holes, are also observed in crystalline solids. If there are impurities, e.g., solute atoms M_f , substitutional or interstitial defects of M_f could be formed, which can also be either charged or neutral.

As multicomponent compounds, the compositions of ceramics can be nonstoichiometric, if they are annealed in certain gaseous atmospheres, such as oxygen with controlled partial pressures, which is driven by the tendency to approach an equilibrium state with the surrounding environment. The consequence of the equilibration is the deviation of the composition from stoichiometry and the variation in concentration of the defects. For instance, if MO is annealed at an environment of low oxygen partial pressure, either oxygen-deficient oxide, i.e., MO_{1-x} , or metal excess oxide, i.e., $M_{1+y}O$, could be formed. However, if it is annealed at higher oxygen partial pressures, metal deficient oxide, i.e., $M_{1-y}O$, could be obtained, with metal vacancies to be the predominant defect. However, In this case, it is quite difficult to form oxygen interstitial, due to the large size of the oxygen ions.

Charged defects in solids have interactions with one another, which are similar to the interactions among ions, sometimes involving electrons, in solutions. In the solid-state cases, the crystals are considered to be a neutral medium, which can dissolve the charged defects. Defect chemistry is to study the properties and behaviors of point defects in solid materials. As stated earlier, according to their originality, there are two types of defects: (i) intrinsic and (ii) extrinsic defects. Intrinsic defects are thermally generated in pure compounds, while extrinsic defects are produced by introduction impurities or treatment in gaseous atmospheres.

5.2.2.2 Kroger-Vink Notation

The description of point defects in ionic solids is well represented by a standard notation, known as the Kroger-Vink notation. In this notation system, a defect, which is defined with respect to the perfect lattice, is described by three parts: the main symbol, a subscript, and a superscript. For instance, in the notation, M_L^C , the main symbol M represents the particular atom, or for a vacancy, it is V . The subscript L means the lattice site at which the defect is located. The superscript C describes the effective charge or relative charge of the defect, which is equal to the difference in valence between the species on the L site and the valence of the atom that occupies the L site in the perfect lattice before the formation of the defect. The effective charge could be: (i) positive, $C = \cdot$, (ii) negative, $C = '$ or (iii) neutral, $C = \times$. For electronic defects, a quasi-free electron is represented as e' , while a missing electron or hole is represented as h' . Possible defects in Al_2O_3 are listed in Table 5.1, by using the Kroger-Vink notation. Square brackets are used to represent the concentration of defects, such as $[V_O^{\cdot\cdot}]$ and $[Ti_{Al}^{\cdot}]$. The concentrations of electrons and holes, $[e']$ and $[h']$, are usually simplified as n and p , respectively.

5.2.2.3 Defect Reactions

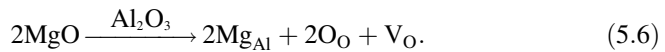
Similarly to chemical reactions, the formation of defects or defect reactions can be constructed according to the following three conservation rules, i.e., (i) mass conservation or mass balance, (ii) electroneutrality or charge balance, and (iii) site ratio conservation or site balance.

Table 5.1 Kroger-Vink notation of potential defects in Al_2O_3

Notation	Defect
$Al_i^{\cdot\cdot}$	Al^{3+} ion at interstitial site
$V_{Al}^{\cdot\cdot\cdot}$	Al^{3+} vacancy
$V_O^{\cdot\cdot}$	O^{2-} vacancy
Mg'_{Al}	Mg^{2+} replacing Al^{3+} at lattice site
Ti^{\cdot}_{Al}	Ti^{4+} replacing Al^{3+} at lattice site
e'	Electron
h'	Hole

A mass balance should be maintained so that mass is neither created nor destroyed in the defect reaction. Vacancies have zero mass, while the effect of electronic defects on the mass balance is neglected. The crystal must be electrically neutral in the defect reaction, which means that, the sum of the positive effective charges should be equal to the sum of the negative effective charges, for the whole reaction. The ratio of the number of regular cation sites to the number of regular anion sites in the crystal must be constant in the defect reaction. For example, in the compound MO_2 , the ratio of the regular M and O sites must always have the ratio of 1:2. Sites may be created or destroyed in the defect reaction, but site ratio in the regular lattice cannot be changed.

For instance, if MgO is used to dope Al_2O_3 , because the ionic radii of Mg^{2+} and Al^{3+} with coordination number of six are very close, the Mg ions can enter the lattice of Al_2O_3 to form solid solution as substitutional defects. Al_2O_3 has the corundum structure, in which one-third of the octahedral sites formed by the close-packed O ions are vacant, so that it is also highly possible for the Mg ions to sit on the interstitial sites. The defects with lower energy are more favorable. In Al_2O_3 , the cation sites and anion sites have a number ratio of 2:3. If substitutional defects are formed, every two Mg atoms on cation sites will replace two Al sites and two O sites are involved. In this case, the third O site should be a vacancy for site conservation. Therefore, on the basis of mass and site balance, the defect reaction is given by:

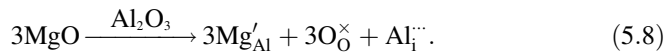


When the defects are fully ionized, with conservation of electroneutrality, there is:

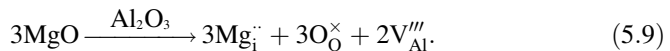


Therefore, all mass, charge, and site ratio are balanced.

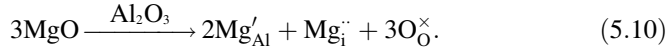
If Al interstitials are formed, instead of O vacancies, the defect reaction is given by:



In this equation, the mass and site ratio are not balanced, so that it is invalid. If the Mg ions take interstitial sites, there is the following defect reaction:



Furthermore, if Mg is self-compensated to form both substitutional and interstitial defects, the reaction is given by:



Although the formation of interstitials does not create new crystal sites, they must be considered for mass and charge conservations.

5.2.2.4 Concentration of Defects

The concentration of defects can be derived from statistical thermodynamics point of view, but it is more convenient to treat the formation of defects as a chemical reaction, so that equilibrium constant of mass action can be applied. For a general reaction, in which the reactants A and B lead to products C and D , the equation is given by:



where a , b are the numbers of moles of the reactants while c and d are those of the products. At a given temperature, when the reaction reaches an equilibrium state, if it is assumed that the activities of the reactants and products are equal to their concentrations, according to the law of mass action, there is an equation that governs the interrelationship among the reactants and products, as following:

$$K = \frac{[C]^c [D]^d}{[A]^a [B]^b}, \quad (5.12)$$

where the square brackets are used to represent the concentrations and K is called the equilibrium constant. The constant K is given by the Arrhenius equation as follows:

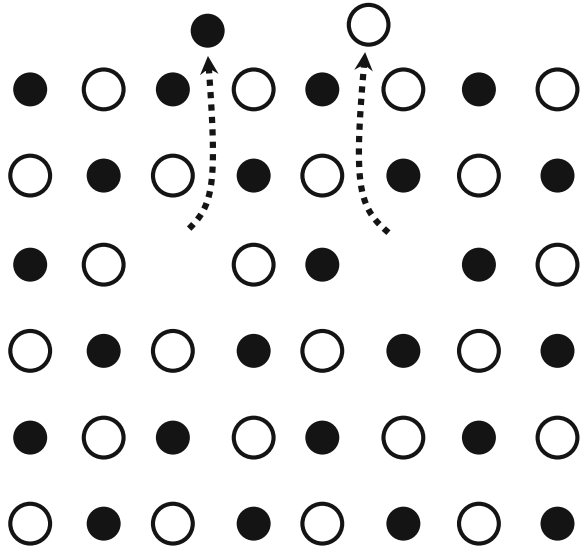
$$K = \exp\left(\frac{-\Delta G}{RT}\right), \quad (5.13)$$

where ΔG is the Gibbs free energy change of the reaction, R is the gas constant, and T is absolute temperature. In defect reactions, concentrations of the defects are usually expressed as fractions of sites, when using Eqs. (5.12) and (5.13). If the concentrations of the defects are sufficiently low, concentrations of the ions at their regular lattice sites are taken as unity. When a reaction involves gas phases, their partial pressures will be used as the concentrations of the gases.

5.2.2.5 Intrinsic Defects

There are two typical intrinsic defects in ionic crystals: (i) Schottky defect and (ii) Frenkel defect.

Fig. 5.2 Schematic diagram illustrating the formation of a Schottky defect. Reproduced with permission from [1]. Copyright © 2003, CRC Press



When a cation and an anion are taken away from their regular lattice sites to an external surface, an extra perfect crystal is formed and a pair of vacancies is left behind, which are called Schottky defect, as shown schematically in Fig. 5.2 [1]. To meet the requirement of electroneutrality balance of the crystal, vacancies must be formed in the stoichiometric ratio.

For simple oxide MO , if the defects are assumed to be fully ionized, the defect formation reaction can be written as:



Here, M_M^{\times} and O_O^{\times} on both sides of the equation can be canceled out, so that the net reaction can be simplified as:

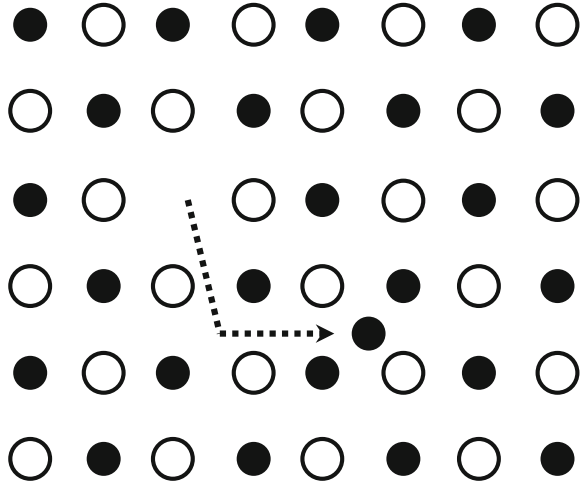


where 0 means that the defects are created from a perfect lattice, which also can be written as null of nil. When the reaction reaches equilibrium, according to the law of mass action, there is:

$$K_S = [V_M''] [V_O^{\cdot\cdot}] = \exp\left(\frac{-\Delta G_S}{RT}\right), \quad (5.16)$$

where K_S is the equilibrium constant and ΔG_S is the Gibbs free energy change of the formation of Schottky defects. For electroneutrality balance, there is $[V_M''] = [V_O^{\cdot\cdot}]$, so that the concentrations of the defects are given by:

Fig. 5.3 Schematic diagram showing the formation of a Frenkel defect. Reproduced with permission from [1]. Copyright © 2003, CRC Press



$$[V_M''] = [V_O^\cdot] = \exp\left(\frac{-\Delta G_S}{2RT}\right). \tag{5.17}$$

When an ion leaves its regular lattice site and stays at an interstitial site, leaving behind a vacant site, Frenkel defect is formed, as shown schematically in Fig. 5.3 [1]. For a simple oxide MO, if the defects are assumed to be fully ionized, the formation of a Frenkel defect at the cation site can be expressed as:



The equilibrium constant of the reaction is given by:

$$K_F = [M_i^\cdot][V_M''] = \exp\left(\frac{-\Delta G_F}{RT}\right). \tag{5.19}$$

Electroneutrality balance requires that the concentration of metallic interstitial should be equal to that of the metallic vacancy, i.e., $[M_i^\cdot] = [V_M'']$. In this case, the concentrations of the defects can be calculated by the following equations:

$$[M_i^\cdot] = [V_M''] = \exp\left(\frac{-\Delta G_F}{2RT}\right). \tag{5.20}$$

Similar equations can be obtained as the Frenkel defects are formed at anion sites. However, anion Frenkel defects are rarely encountered, because anions have relatively large sizes, i.e., there are no interstitial sites for them to stay. Also, the formation of cation and anion Frenkel defects is not controlled by the requirement of electroneutrality balance, so that the concentration of cation interstitial may not

be necessarily equal to that of anion interstitial. In other words, cation and anion can form interstitials independently.

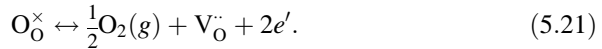
5.2.2.6 Extrinsic Defects

As stated earlier, extrinsic defects are formed due to external influences, such as gaseous atmosphere environment which is usually responsible for nonstoichiometry in composition and impurities which can be intentionally incorporated such as dopants or unintentionally introduced such as impurities.

Nonstoichiometry

Equilibration of ionic solids with an ambient gaseous environment, e.g., metal oxide versus oxygen, can have a significant effect on the structure and behavior of defects. Oxides with elements of fixed valency, such as MgO, Al₂O₃, and ZrO₂, are not easily to deviate from the stoichiometry, while those with elements having variable valence, such as NiO, CoO, FeO, SnO₂, and TiO₂, could be deviated from the stoichiometry.

At a given temperature and composition, oxides are always in equilibrium with a specific oxygen partial pressure or tend to give out or take up oxygen until new equilibrium is reached. When oxides release oxygen, reduction reaction occurs, oxygen vacancies could be created in the lattice, in which with the electrons are liberated within the solid. The overall reaction can be written as:



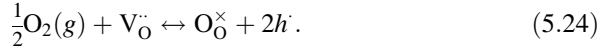
The creation of the oxygen vacancies will change the number ratio to cation to anion, i.e., nonstoichiometry is present. The equilibrium constant for the reaction is given by:

$$K_\text{R} = n^2[\text{V}_\text{O}^\cdot]p_{\text{O}_2}^{1/2} = K_\text{R}^0 \exp\left(\frac{-\Delta G_\text{R}}{RT}\right), \quad (5.22)$$

where the concentration of the oxygen gas is the partial pressure, K_R^0 is the equilibrium constant, and ΔG_R is the free energy change of the reduction. For electroneutrality balance, there is $n = 2[\text{V}_\text{O}^\cdot]$, so that the concentration of oxygen vacancy can be derived from Eq. (5.22), given by:

$$[\text{V}_\text{O}^\cdot] = \left(\frac{K_\text{R}}{4}\right)^{1/3} p_{\text{O}_2}^{-1/6}. \quad (5.23)$$

When the oxides take up oxygen, oxidation reaction takes place, which can be treated as the consumption of oxygen vacancies, with the charge being balanced by combining with an electron, thus leading to a missing electron or hole in the valence band, with defect reaction being expressed as:



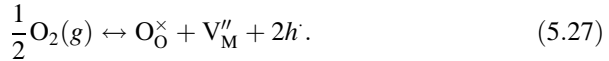
The equilibrium constant is given by:

$$K_\text{O} = \frac{p^2}{[\text{V}_\text{O}^{\bullet\bullet}]^{1/2} p_{\text{O}_2}} = K_\text{O}^0 \exp\left(\frac{-\Delta G_\text{O}}{RT}\right) \quad (5.25)$$

Because oxidation and reduction are reversed reactions each other, which are actually the same process from the thermodynamic point of view, their reaction equations are dependent mutually. For example, if the reduction reaction of Eq. (5.21) is combined with the intrinsic electronic defect equilibrium:

$$0 = e' + h^\cdot, \quad (5.26)$$

which leads to the oxidation reaction of Eq. (5.24). Therefore, the oxidation and reduction reactions can be expressed in a number of different ways, the use of them is determined mainly by the consideration of convenience. For instance, oxidation can also be treated as the creation of oxygen lattice and cation vacancies. When their charges are combined with electrons, holes are formed in the valence band. For simple oxide MO, the reaction can be written as:

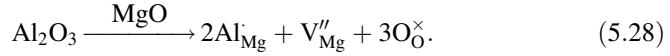


Equation (5.27) can be obtained by adding the Schottky reaction to Eq. (5.24).

Effects of Dopants

Dopants, also known as solutes, with low concentrations, can significantly influence the sintering of ceramics. Dopants sometimes are necessary to create functionalities of ceramics. When the cation valence is different from that of the host cation, the dopant is called aliovalent dopant, whereas if the cation has the same valence as that of the host, it is called an isovalent dopant. For aliovalent dopants, when the valence of the solute cation is higher than that of the host cation, the dopant is known as a donor, otherwise, it is called a acceptor. Therefore, if Al_2O_3 is host, TiO_2 and MgO are donor and acceptor, respectively.

When Al_2O_3 is incorporated into MgO , due to the similarity in ionic radii, it is assumed that the Al will substitute for Mg, with charge balanced achieved by the creation of a vacant Mg site, through the following equation:



If the intrinsic defects in MgO are assumed to be Schottky defects, according to Eq. (5.16), there is:

$$[\text{V}_{\text{O}}^{\cdot}][\text{V}_{\text{Mg}}''] = K_{\text{S}}. \quad (5.29)$$

The condition for charge balance is given by:

$$[\text{Al}_{\text{Mg}}^{\cdot}] + 2[\text{V}_{\text{O}}^{\cdot}] = 2[\text{V}_{\text{Mg}}'']. \quad (5.30)$$

At very low concentration of Al_2O_3 , $[\text{Al}_{\text{Mg}}^{\cdot}] \ll [\text{V}_{\text{Mg}}'']$, so that there is:

$$[\text{V}_{\text{O}}^{\cdot}] = [\text{V}_{\text{Mg}}''] = K_{\text{S}}^{1/2}, \quad (5.31)$$

which means that the concentration of the intrinsic defects are independent on the concentration of Al_2O_3 . In other words, the intrinsic defects are dominant.

When the concentration of Al_2O_3 in solid solution is increased, the extrinsic defects begin to be dominant. The charge balance is given by:

$$[\text{Al}_{\text{Mg}}^{\cdot}] = 2[\text{V}_{\text{Mg}}'']. \quad (5.32)$$

If the Al_2O_3 is completely incorporated, the concentration of Al in solid solution is equal to the total atomic concentration of Al, so that there is:

$$[\text{Al}_{\text{Mg}}^{\cdot}] = [\text{Al}]. \quad (5.33)$$

Because Eq. (5.29) is applicable for the cation and anion vacancies, combination of Eq. (5.29) with Eqs. (5.32) and (5.33) yields:

$$[\text{V}_{\text{O}}^{\cdot}] = \frac{2K_{\text{S}}}{[\text{Al}]}. \quad (5.34)$$

Furthermore, according to Eqs. (5.32) and (5.33), there also is following equation:

$$[\text{V}_{\text{Mg}}''] = \frac{1}{2}[\text{Al}]. \quad (5.35)$$

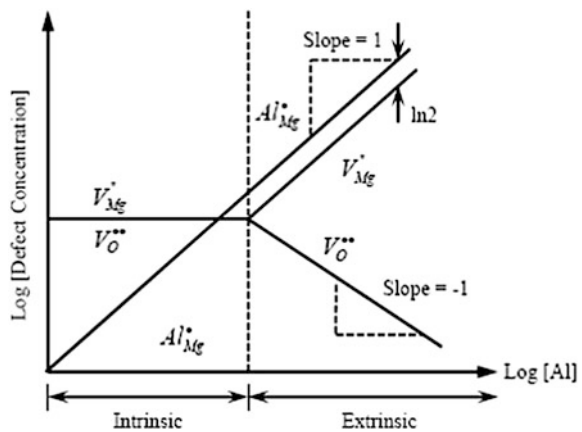
Brouwer Diagram

The variation in concentration of defects as a function of temperature, oxygen partial pressure or dopant concentration can be described semi-quantitatively in terms of a double logarithmic plot, which is known as a Brouwer diagram. Figure 5.4 shows a Brouwer diagram for the effects of Al_2O_3 dopant on the defect chemistry of MgO , as discussed above [1]. Similar plots can be constructed for the variations in concentration of defect with temperature or oxygen partial pressure. The Brouwer diagram shows the net effect, when different defect reactions are considered at the same time. Although there are unlimited number of defect reactions that can be derived for a given system, the number of defects that must be used to describe a given property that is related to defects, such as electrical conductivity or sintering, is actually limited. Also, it is necessary to identify the majority defects that determine the properties of the materials, as well as minority defects that could be relevant to a specific property of interest. The main defects that are usually considered in writing defect reactions include: (i) major intrinsic ionic defects (Schottky or Frenkel), (ii) intrinsic electronic defects, (iii) oxidation or reduction, and (iv) dopants. In addition, an equation for the electroneutrality condition is always necessary.

5.2.2.7 Defect Chemistry and Sintering

With the above discussion, it is summarized that the concentration of the point defects and thus the rate of matter transport through in crystal solids can be controlled by controlling three variables: (i) temperature, (ii) oxygen partial pressure, i.e., the gaseous atmosphere, and (iii) concentration of dopants. In the system of Al_2O_3 -doped MgO discussed above, if the sintering rate of MgO is controlled by the diffusion of oxygen vacancies, the addition of Al_2O_3 will decrease the sintering rate, according to Eq. (5.34). However, if the diffusion of Mg vacancy is the rate-

Fig. 5.4 Brouwer diagram for MgO doped with Al_2O_3 . The defect concentrations are shown as a function of the concentration of Al. Reproduced with permission from [1]. Copyright © 2003, CRC Press



controlling mechanism, the presence of Al_2O_3 will increase the sintering rate, as demonstrated by Eq. (5.35). The factors that affect the sintering rate could be much more complicated in real systems. Also, the mechanisms of rate-controlling of sintering in most cases have not been clarified until now. Furthermore, there could be more than one mechanism during the sintering of a given material system and the rates of transport related to the different mechanisms can be changed with various conditions. There are also other factors, such as particle packing homogeneity, particle size, and size distributions, which could have significant effects on the rates of sintering.

5.2.3 Diffusion in Crystalline Solids

5.2.3.1 Fick's Laws of Diffusion

In the theory of solid-state diffusion, it is usually assumed that the movement of a diffusing species is driven by the gradients in concentration, irrespective with the atomic nature of crystal structure and atomic defects. The concentration can vary as a function of distance and time. When the concentration is changed with time, the diffusion process is described mathematically by the Fick's first law, i.e., the flux of the diffusing species J , which is defined as the number of items crossing per unit area normal to the direction of flux per second, is proportional to the concentration gradient dC/dx , which takes place in the direction of decreasing concentration. The one-dimensional Fick's first law is given by:

$$J_x = -D \frac{dC}{dx}. \quad (5.36)$$

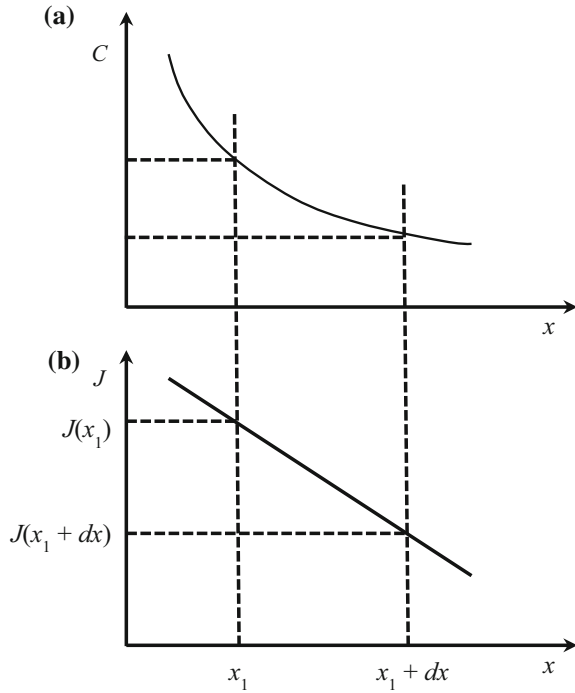
The proportionality D is a constant, which is known as the diffusion coefficient or diffusivity, with a unit of $\text{m}^2 \text{s}^{-1}$ (SI) or $\text{cm}^2 \text{s}^{-1}$. The diffusion coefficient is a property of materials, which is the most useful parameter to characterize the rate of diffusive mass transport, showing a strong dependence on temperature. Although it is also a function of composition, if the diffusing species are significantly diluted, it can be assumed to be independent on the composition.

In practical experiments, it is difficult to maintain a concentration to be independent of time. Therefore, it is more often to characterize the change in concentration as a function of time t , thus leading to Fick's second law. For one dimension, the Fick's second law is given by:

$$\frac{dC}{dt} = D \frac{d^2C}{dx^2}. \quad (5.37)$$

The Fick's second law can be derived from the first law, together with the principle of matter conservation. For one-dimension, a region between the two

Fig. 5.5 Concentration C versus distance x (a) and the resulting flux J versus distance (b). Reproduced with permission from [1]. Copyright © 2003, CRC Press



planes $[x_1, (x_1 + dx)]$ can be considered, as shown in Fig. 5.5 [1]. Figure 5.5a shows the solute concentration C as a function of distance x . Because dC/dx at x_1 is larger than dC/dx at $(x_1 + dx)$, $J(x_1)$ will be larger than $J(x_1 + dx)$, as shown schematically in Fig. 5.5b. Also, because $J(x_1) > J(x_1 + dx)$, if matter conservation is applied, the solute concentration in the region between x_1 and $x_1 + dx$ should increase. Considering a volume element with unit area normal to the x axis and dx in thickness, the rate of change of concentration is given by:

$$\left(\frac{dC}{dt}\right)_{x_1} dx = J(x_1) - J(x_1 + dx). \tag{5.38}$$

If dx is small, $J(x_1 + dx)$ can be related to $J(x_1)$ through the following equation:

$$J(x_1 + dx) = J(x_1) + \left(\frac{dJ}{dx}\right)_{x_1} dx. \tag{5.39}$$

By substituting Eq. (5.39) into Eq. (5.38) and using Eq. (5.36) for J , there is:

$$\frac{dC}{dt} = -\frac{dJ}{dx} = -\frac{d}{dx} \left(-D \frac{dC}{dx}\right) = D \frac{d^2C}{dx^2}. \tag{5.40}$$

Equation (5.37) can be solved with certain boundary conditions that are determined by experiments.

For instance, a common technique to measure diffusion coefficient D is to deposit a very thin layer of a radioactive isotope (or mass isotope) on a flat surface of a thick sample, which is then annealed at a given temperature for a given time duration. By measuring the concentration of the diffusing species as a function of distance, the diffusion coefficient can be determined. In this case, the experimental system is a semi-infinite solid. If the initial thickness of the radioisotope layer is sufficiently small as compared with the diffusing distance of the radioisotope, the solution of Eq. (5.37) is given by:

$$C = \frac{C_0}{(\pi D^* t)^{1/2}} \exp\left(\frac{-x^2}{4D^* t}\right), \quad (5.41)$$

where C is the concentration at a distance x from the surface, t is the annealing time, and C_0 is the initial concentration in moles per unit area of the radioisotope, i.e., at $t = 0$. D^* is the diffusion coefficient of the radioisotope, which is known as the tracer diffusion coefficient.

5.2.3.2 Atomistic Diffusion Processes

Figure 5.6 schematically shows the diffusion of an atom at atomic level, the atom undergoes periodic jumping from one lattice site to another site via an intermediate stage of higher energy, which separates the sites that the atom sits before and after the diffusion process [1]. The energy barrier that must be overcome by the atom at the intermediate state before the jumping takes place is called activation energy. This periodic jumping experienced by the atoms is similar to a Brownian motion, which occurs in a random way over the lattice sites. Therefore, it is also called random diffusion, which can be described similarly to a random-walk problem, in order to determine the relationship between the macroscopic diffusion coefficients and the jump frequencies and jump distances of the atoms.

There are two adjacent planes, A and B , apart with a distance λ , in a crystalline solid that has a concentration gradient along the x axis, as shown schematically in Fig. 5.7 [1]. There are n_A diffusing atoms per unit area in plane A and n_B in plane B . Only the jumps to the left and right, i.e., those causing a change in position along the x axis, are considered. In this case, the probability P that an atom will have sufficiently high energy to overcome the energy barrier q is given by:

$$P = \exp\left(-\frac{q}{kT}\right), \quad (5.42)$$

where k is the Boltzmann constant and T is the absolute temperature. The number of atoms per unit area of plane A that have sufficient energy to overcome the energy barrier from A to B at any instant is $n_A P = n_A \exp(-q/kT)$. If the atoms vibrate about

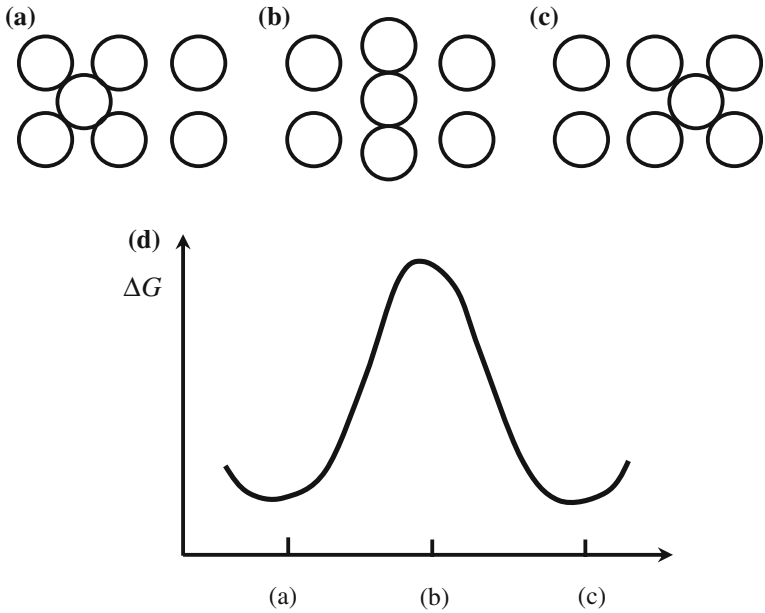
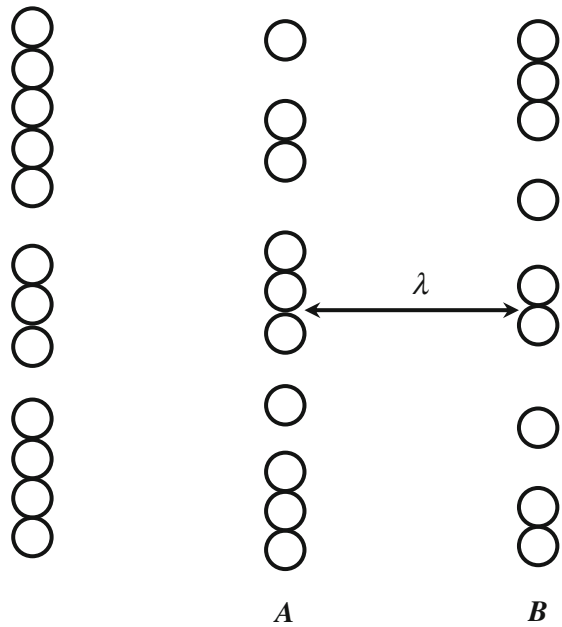


Fig. 5.6 Schematic diagram showing the sequence of configurations when an atom jumps from one lattice site to another (a–c) and the corresponding change in the free energy of the lattice (d). Reproduced with permission from [1]. Copyright © 2003, CRC Press

Fig. 5.7 Planes of atoms with a gradient in their concentration. Reproduced with permission from [1]. Copyright © 2003, CRC Press



their mean positions at a frequency ν , and assuming that the vibration frequency is the same in all six orthogonal directions, the flux of the atoms, i.e., the number jumping across unit area per second, from A to B is $(\nu/6)n_A \exp(-q/kT)$. Similarly, the flux of atoms from B to A is $(\nu/6)n_B \exp(-q/kT)$. Therefore, the net flux of atoms from A to B is therefore given by:

$$J = \frac{\nu}{6}(n_A - n_B) \exp\left(\frac{-q}{kT}\right). \quad (5.43)$$

If λ is the distance between the two adjacent planes, $n_A - n_B$ can be related to their concentrations, which is the number of the atoms per unit volume, with $n_A/\lambda = C_A$ and $n_B/\lambda = C_B$. In this case, the flux is given by:

$$J = \frac{\nu\lambda}{6}(C_A - C_B) \exp\left(\frac{-q}{kT}\right). \quad (5.44)$$

If it is assumed that the change in C is sufficiently slow, there will be $C_A - C_B = \lambda(dC/dx)$, so that Eq. (5.44) becomes:

$$J = \frac{\nu\lambda^2}{6} \exp\left(\frac{-q}{kT}\right) \frac{dC}{dx}. \quad (5.45)$$

This equation is identical to the Fick's first law, with the diffusion coefficient D to be given by:

$$D = \frac{\nu\lambda^2}{6} \exp\left(\frac{-q}{kT}\right). \quad (5.46)$$

Because q is a too small quantity for most diffusing atoms, larger quantities $Q = N_A q$ and $R = N_A k$ are usually used, where Q is the activation energy per mole, N_A is the Avogadro number, and R is the gas constant. Additionally, the term $\nu\lambda^2/6$ is usually represented by D_0 , so that there is:

$$D = D_0 \exp\left(\frac{-Q}{RT}\right). \quad (5.47)$$

In this equation, D has an exponential dependence on temperature, which also has activation energy in the units of J mol^{-1} . Data for the diffusion coefficients of various ceramics can be found in open literatures and handbooks.

Note that the activation energy q is equal to $\Delta h - T\Delta s$, where Δh is the enthalpy and Δs is the entropy for atomic diffusion, Eq. (5.46) then becomes:

$$D = \frac{\nu\lambda^2}{6} \exp\left(\frac{\Delta s}{k}\right) \exp\left(\frac{-\Delta h}{kT}\right), \quad (5.48)$$

which is compared with Eq. (5.47), leading to the following expression:

$$D = \frac{v\lambda^2}{6} \exp\left(\frac{\Delta s}{k}\right). \quad (5.49)$$

Generally, the vibration frequency of atoms about their mean positions, which is usually known as the Debye frequency, is about 10^{13} – 10^{14} s^{-1} and $\lambda \approx 0.2$ nm, so $v\lambda^2/6 \approx 10^{-7}$ $\text{m}^2 \text{s}^{-1}$. The values of D_0 for diffusion by the interstitial and vacancy mechanisms are in the range of 10^{-7} – 10^{-3} $\text{m}^2 \text{s}^{-1}$ [1]. In addition, it has been reported that, for a given group of materials, the values of D_0 and Q/RT_m , with T_m being the melting temperature, are almost the same [19].

5.2.3.3 Diffusion Mechanisms

The types of defects determine the path of matter transport, while the diffusion along the major paths is responsible for the major mechanisms of matter transport. There are three main diffusion types: (i) lattice diffusion (also called volume or bulk diffusion), (ii) grain boundary diffusion, and (iii) surface diffusion.

Lattice Diffusion

Lattice diffusion is related to the movement of point defects over the lattice of crystal solids. Lattice diffusion has vacancy mechanism or interstitial mechanism, depending on the type of defects, vacancy or interstitial, which are most important lattice diffusion mechanisms.

Figure 5.8 shows an example of diffusion by vacancy mechanism, where an atom at a normal lattice site diffuses by exchanging its position with a vacant site [1]. The movement direction of the atom is opposite to that of the vacancy, so that the diffusion of the atom can be tracked, so is the diffusion of the vacancy. Although the diffusion coefficients of the atoms and the vacancies are closely related, they are not necessarily equal to each other. This is because an atom can only jump if a vacancy is located at a lattice site adjacent to it, whereas a vacancy can jump to any of the nearest neighbor sites. As a result, the number of atomic jumps is proportional to the fraction of the sites occupied by vacancies, C_v . The atomic diffusion coefficient D_a and the vacancy diffusion coefficient D_v are related by the following equation:

$$D_a = C_v D_v. \quad (5.50)$$

As discussed above, the concentration of vacancy is determined by temperature, atmosphere and dopants. It is worth mentioning that the flux of vacancies must be compensated by an equal and opposite flux of atoms for vacancy diffusion. Otherwise, the vacancies will be accumulates and form pores in the crystal solids.

In fact, pores can be formed during the interdiffusion of two atoms that have significantly different diffusion coefficients.

Sufficiently small dopants or regular atoms can take interstitial sites of the lattice. When they move to neighboring interstitial sites, interstitial diffusion takes place, as shown schematically in Fig. 5.8b, which can be described by the following equation:

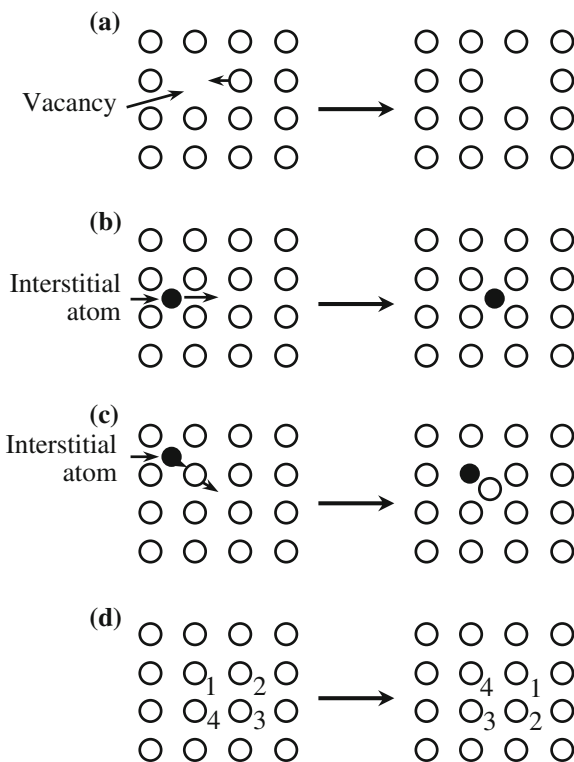
$$D_a = C_i D_i, \tag{5.51}$$

where D_i is now the interstitial diffusion coefficient and C_i is the concentration of the interstitial atoms. This is similar to that of Eq. (5.50).

When the lattice is heavily distorted, interstitial diffusion becomes difficult, so that another diffusion mechanism is present, which is known as interstitialcy mechanism. Interstitialcy diffusion is facilitated by exchanging position between an atom at the regular lattice site with a neighboring interstitial atom, as shown schematically in Fig. 5.8. They can be different types of atoms.

There is another type of lattice diffusion mechanism, called direct exchange or ring mechanism. As shown schematically in Fig. 5.8d, during this diffusion, atoms exchange their positions through rotation in a circle way. There are no any defects involved in this diffusion. This is a multiatomic action. However, this mechanism is

Fig. 5.8 Lattice diffusion by **a** vacancy mechanism, **b** interstitial mechanism, **c** interstitialcy mechanism, and **d** ring mechanism. Reproduced with permission from [1]. Copyright © 2003, CRC Press



rarely observed in ionic crystalline solids, due to the tremendous momentary distortion coupled with the large energy changes arising from the electrostatic repulsion.

Grain Boundary Diffusion

The presence of grain boundaries is one of the most distinct characteristics of polycrystalline ceramics. Grain boundaries are regions that separate the crystals or grains from one another, with lattice mismatching and disordering. Due to the highly defective nature of the grain boundaries, they are expected to have faster diffusion than lattice diffusion in the adjacent grains. Grain boundaries usually have widths of 0.5–1 nm. If the width of grain boundaries is assumed to be a constant, the volume fraction of the grain boundaries will increase with decreasing grain size. Therefore, the rate of grain boundary diffusion has been related to grain size.

Surface Diffusion

As discussed before, the free surface of a crystalline solid is not a perfectly flat plane, which could contain vacancies, terraces, kinks, edges, and adatoms. The migration of vacancies and the movement of adatoms facilitate the mechanisms of surface diffusion. The diffusion process is usually confined to a thin layer near the surface with a thickness of 0.5–1 nm.

Comparison of Diffusion Coefficients

The atoms on the surface are less tightly bound, because they have fewer neighbors than those within the bulk of the lattice. As a result, the activation energy for surface diffusion is less than that for lattice diffusion, which has been confirmed by the available experimental data. Due to its lower activation energy, surface diffusion becomes more and more important as the temperature is decreased, which has a significant effect on sintering. It has often been demonstrated that the diffusion coefficients of lattice diffusion D_l , grain boundary diffusion D_{gb} , and surface diffusion D_s increase in the order of $D_l < D_{gb} < D_s$, while the corresponding activation energies decrease in the order of $Q_l > Q_{gb} > Q_s$. However, these relations are only used as a general trend, which may not be correct for all cases or any case.

5.2.3.4 Types of Diffusion Coefficients

In the literature, there are diffusion coefficients that have been used to describe the diffusion characteristics of a particular species, such as atom, interstitial, or vacancy, a particular diffusion path, such as lattice, grain boundary, or surface diffusion, or a particular process, such as chemical diffusion or ambipolar diffusion.

There are various diffusion coefficients: (i) self-diffusion coefficient, (ii) tracer diffusion coefficient, (iii) lattice diffusion coefficient, (iv) grain boundary diffusion coefficient, (v) surface diffusion coefficient, (vi) defect diffusion coefficients, and (vii) chemical, effective or interdiffusion coefficient.

Self-diffusion coefficient D_{self} is the diffusion coefficient of the host atoms or ions in random diffusion, which is one of the important diffusion coefficients related to sintering. For lattice diffusion by the vacancy or interstitial mechanisms, D_{self} is given by Eq. (5.50) or (5.51).

Tracer diffusion coefficient D_{self} is usually difficult to directly measure. As stated earlier, it is more convenient to measure the diffusion coefficient of a radioactive or mass isotope. This measured coefficient is called the tracer diffusion D^* , which is close to but not the same as D_{self} , because the motion of the tracer atoms is not in a completely random manner. Successive jumps are mutually correlated, so that every jump is dependent on the previous one. Therefore, D_{self} and D^* can be related by the following equation:

$$D^* = fD_{\text{self}}, \quad (5.52)$$

where f is a correlation factor that depends on the crystal structure and the diffusion mechanism. The values for f are in the range 0.6–1.

Lattice diffusion coefficient D_1 represents any diffusion process over the lattice of crystal solids. Grain boundary diffusion coefficient, D_{gb} or D_{b} , describes the diffusions in the grain boundaries. Surface diffusion coefficient D_{s} is to characterize the diffusions over a free surface. Defect diffusion coefficient is used to describe the diffusion of a particular type of defect, such as D_{v} for diffusion coefficient of a vacancy and D_{i} for diffusion coefficient of an interstitial. The diffusion coefficient of a defect is given by Eq. (5.46) or (5.48), which is independent of its concentration. Chemical diffusion coefficient is also known as effective or interdiffusion coefficient. This coefficient \tilde{D} is for the diffusion due to the presence of a gradient in chemical composition or chemical potential, simply because ions will migrate to response any chemical gradient. Interdiffusion takes place when two components of a solid solution migrate in opposite directions down their coupled chemical potential gradients.

5.2.4 Chemical Potential

As discussed previously, matter transport is due to the flux of atoms or vacancies driven by gradients in the concentration, which can be described by using the Fick's first law. This special case of mass transport is not applicable to those with other types of driving forces, such as gradients in pressure, electric potential, and so on. To address this issue, it is necessary to use chemical potential, instead of concentration gradients, as driving force of the diffusions. Definition and description of chemical potential can be found in various textbooks.

5.2.4.1 Chemical Potential

For a phase with a given amount of mass and composition, at variable temperature T and pressure p , as an infinitesimal reversible process occurs, the change in the Gibbs free energy is given by:

$$dG = \left(\frac{\partial G}{\partial T}\right)_p dT + \left(\frac{\partial G}{\partial p}\right)_T dp = -SdT + Vdp, \quad (5.53)$$

where S is the entropy and V the volume of the system. For a phase of variable compositions, consisting of m chemical constituents, in which there are n_1 mol of the substance A_1 , n_2 mol of A_2 , ..., n_m moles of A_m , the change in the Gibbs free energy is now given by:

$$dG = \left(\frac{\partial G}{\partial T}\right)_{p,n_1,n_2,\dots,n_m} dT + \left(\frac{\partial G}{\partial p}\right)_{T,n_1,n_2,\dots,n_m} dp + \left(\frac{\partial G}{\partial n_1}\right)_{p,T,n_2,n_3,\dots,n_m} dn_1 + \dots + \left(\frac{\partial G}{\partial n_m}\right)_{p,T,n_2,n_3,\dots,n_{m-1}} dn_m. \quad (5.54)$$

Because the first two terms on the right-hand side of the equation are at constant mass and composition, Eq. (5.53) can be used. In this case, when a small amount of one constituent, e.g., dn_k moles of the k th constituent, is introduced into the phase, with T , p , and the other n 's remaining constant, the effect on the Gibbs free energy can be expressed as:

$$\mu_k = \left(\frac{\partial G}{\partial n_k}\right)_{p,T,n_1,n_2,\dots,n_{k-1},n_{k+1},\dots,n_m}, \quad (5.55)$$

where μ_k is called the chemical potential of the k th constituent. Equation (5.54) can now be rewritten as:

$$dG = -SdT + Vdp + \sum_i^m \mu_i dn_i. \quad (5.56)$$

If the number of moles of a phase is increased, while T , p , and the composition are kept unchanged, Eq. (5.56) becomes:

$$dG_{T,p} = \sum_i \mu_i dn_i. \quad (5.57)$$

Because the μ_i is dependent only on T, p , and composition and they must be kept to be constant, Eq. (5.57) can be integrated to yield:

$$G = \sum_i \mu_i n_i. \quad (5.58)$$

For a pure substance, Eq. (5.58) can be reduced to:

$$G = \mu n, \quad (5.59)$$

which means that the chemical potential is the Gibbs free energy per mole at the given temperature and pressure.

5.2.4.2 Chemical Potential of Gas Mixtures

For 1 mol ideal gas at constant temperature T , there is:

$$\left(\frac{\partial G}{\partial p}\right)_T = V = \frac{RT}{p}, \quad (5.60)$$

where R is the gas constant and p is the pressure.

Integration of Eq. (5.60) yields:

$$G(T, p) = G_0(T) + RT \ln p, \quad (5.61)$$

where G_0 is the Gibbs free energy at standard pressure at the temperature, which is used as a reference to calculate Gibbs free energy change. The general expression for chemical potential now is given by:

$$\mu(T, p) = \mu_0(T) + RT \ln p. \quad (5.62)$$

For a mixture of ideal gases at constant temperature T and a constant total pressure, following Eq. (5.62), we can write for each component:

$$\mu_i(T, p) = \mu_{0,i}(T) + RT \ln p_i, \quad (5.63)$$

where p_i is the partial pressure of the i th component. To be more useful, the Gibbs free energy or the chemical potential of a particular component is usually related to its concentration, which is defined as:

$$C_i = \frac{n_i}{\sum n_i} = \frac{p_i}{p}, \quad (5.64)$$

where n_i is the number of moles of each component in the mixture and p is the total gas pressure of the system. Equation (5.63) can now be rewritten as:

$$\mu_i(T, p, C_i) = \mu_{0,i}(T, p) + RT \ln C_i, \quad (5.65)$$

Real gases have deviation from the behavior of ideal gas. If the deviation is sufficiently small, Eqs. (5.63)–(5.65) can be used for satisfactory estimations.

5.2.4.3 Chemical Potential of Solids and Liquids

The chemical potential of solid and liquid solutions can be defined as an expression similar to Eq. (5.63), in which the p_i is replaced by a new term a_i , called the activity. In this case, the chemical potential is given by:

$$\mu_i = \mu_{0,i} + RT \ln a_i. \quad (5.66)$$

The activity of pure liquids and solids, under some specified standard conditions of temperature and pressure, is considered to be unity. The activity of a component in mixture systems is expressed as:

$$a_i = \alpha_i C_i, \quad (5.67)$$

where α_i is called the activity coefficient and C_i is the concentration of the component, which is usually described as mole fraction. The chemical potential of the i th species in liquid or solid solutions is therefore given by:

$$\mu_i = \mu_{0,i} + RT \ln(\alpha_i C_i). \quad (5.68)$$

For ideal solutions, $\alpha_i = 1$.

5.2.4.4 Chemical Potential of Atoms and Vacancies in Crystals

It is assumed that vacancies are the only defects in a crystal of a pure element. If the numbers of the atoms and vacancies are N_a and n_v , the total number of lattice sites in the crystal is $N = N_a + n_v$. As a result, the Gibbs free energy of the crystal can be expressed as:

$$G = U + n_v g + pV - TS, \quad (5.69)$$

where U is the internal energy of the crystal and g is the energy required from the vacancy. The configurational entropy of the crystal can be obtained by using the Boltzmann relation, which in this case can be written as:

$$S = k \ln \left[\frac{(N_a + n_v)!}{N_a! n_v!} \right], \quad (5.70)$$

where k is the Boltzmann constant. The chemical potential of the atoms is defined as:

$$\mu_a = \left(\frac{\partial G}{\partial N_a} \right)_{T,p,n_v}. \quad (5.71)$$

The factorials in Eq. (5.70) can be simplified by using the Stirling approximation, which is then applied to Eq. (5.71), leading to the following equation:

$$\mu_a = \mu_{0,a} + p\Omega_a + k \ln \left(\frac{N_a}{N_a + n_v} \right), \quad (5.72)$$

where $\mu_{0,a}$ is a reference value or standard value and Ω_a is the volume of an atom, which is defined as:

$$\Omega_a = \left(\frac{\partial V}{\partial N_a} \right)_{T,p,n_v}. \quad (5.73)$$

If C_a is the fraction of lattice sites occupied by the atoms in the crystal, then Eq. (5.71) can be written as:

$$\mu_a = \mu_{0,a} + p\Omega_a + k \ln C_a. \quad (5.74)$$

This equation means that the chemical potential of atoms in a crystal is dependent on the pressure and the atomic concentration. It is also noted that if the concentration of the vacancy is sufficiently low, the last term on the right-hand side of Eqs. (5.72) and (5.74) can be neglected.

The chemical potential of the vacancies is defined as:

$$\mu_v = \left(\frac{\partial G}{\partial n_v} \right)_{T,p,N_a}. \quad (5.75)$$

Similar to the procedure used for μ_a , the chemical potential of the vacancies is given by:

$$\mu_v = \mu_{0,v} + p\Omega_v + k \ln C_v, \quad (5.76)$$

where C_v is the concentration of the vacancy, which is the fraction of lattice sites occupied by the vacancies. Although the volume of a vacancy Ω_v , can be different from the volume of an atom Ω_a , the rigid lattice approximation can be used to assume that $\Omega_a = \Omega_v = \Omega$, which makes it more convenient for further analysis.

5.2.4.5 Curved Surface

Chemical potentials of the atoms and vacancies beneath curved surfaces are different when the curvatures of the surfaces are different. This difference in chemical potential provides a driving force for the diffusional flux of atoms, in order to reduce the free energy of the system. The understanding of the dependence of chemical potential of atoms on curvature is especially important to the understanding of sintering.

For a pure element solid with adjoining convex and concave surfaces, it is assumed that vacancies are the only type of point defects in the solid. The surface area of the convex surface will be decreased, if the volume of the region beneath it is reduced, which can be achieved by reducing the concentration of the vacancies. Because a decrease in surface area means a decrease in contribution of the surface to the total free energy of the system, the concentration of the vacancy under convex surface is lower than that beneath a flat surface. Similarly, the concentration of the vacancy beneath the concave surface is higher than that under a flat surface. Therefore, the difference in the concentration of the vacancy results in a diffusional flux of vacancies from the concave region to the convex region, while a diffusional flux of atoms from the convex region to the concave region will be observed accordingly.

On a smoothly curved surface, when an infinitesimal hump is created on the surface by taking atoms from beneath the surface and adding them to the surface, the change in surface free energy is approximately given by:

$$\delta \left(\int \gamma_{SV} dS \right) = \int \delta(\gamma_{SV}) dS_0 + \int \gamma_{SV} \delta(dS), \quad (5.77)$$

where δ means a small change in a quantity, γ_{SV} is the specific surface energy, and dS is the change in surface area. It is assumed that the surface is uniform and isotropic, so that the first term on the right-hand side of Eq. (5.77) is zero, while the term $\delta(dS)$ is given by:

$$\delta(dS) = (\sec \psi - 1) dS_0 + \delta z \left(\frac{1}{R_1} + \frac{1}{R_2} \right) dS_0, \quad (5.78)$$

where R_1 and R_2 are the two principal radii of curvature at dS_0 . If Δy is small, R_1 and R_2 can be considered to be constant over the hump. The first term on the right-hand side of Eq. (5.78) can be neglected. When it is put into Eq. (5.77), the following equation can be obtained:

$$\delta \left(\int \gamma_{SV} dS \right) = \gamma_{SV} \left(\frac{1}{R_1} + \frac{1}{R_2} \right) \delta v, \quad (5.79)$$

where δv is the volume of the hump.

The change in the volume term of the free energy due to the creation of the small hump is given by:

$$\delta G_v = -p\delta_v + \mu_v \frac{\delta_v}{\Omega}, \quad (5.80)$$

where p is the mean hydrostatic pressure in the crystal just beneath the surface, μ_v is the chemical potential of a vacancy, and δ_v/Ω represents the number of vacancies created by the transfer of atoms to the hump. In equilibrium, the sum of the energy changes defined by Eqs. (5.79) and (5.80) should be zero, so that the following equation is derived:

$$\mu_v = p\Omega + \gamma_{sv} \left(\frac{1}{R_1} + \frac{1}{R_2} \right) \Omega. \quad (5.81)$$

If the curvature K of the surface is defined as:

$$K = \frac{1}{R_1} + \frac{1}{R_2}, \quad (5.82)$$

where $K > 0$ for a convex surface. Putting K into Eq. (5.81) yields:

$$\mu_v = (p + \gamma_{sv}K)\Omega. \quad (5.83)$$

Generally, chemical potential is measured relative to a reference value $\mu_{0,v}$, and μ_v contains a term of vacancy concentration. The chemical potential of vacancy μ_v , with curvature, pressure and concentration, is given by:

$$\mu_v = \mu_{0,v} + (p + \gamma_{sv}K)\Omega + kT \ln C_v. \quad (5.84)$$

Similarly, the chemical potential of the atoms can be expressed by:

$$\mu_a = \mu_{0,a} + (p + \gamma_{sv}K)\Omega + kT \ln C_a. \quad (5.85)$$

Because C_a is usually very small, the last term can be taken as zero.

In Eqs. (5.84) and (5.85), because C_a and C_v are generally very low, the last terms can be neglected. Therefore, μ_a and μ_v are determined essentially by the hydrostatic pressure in the solid and the curvature of the surface. Since the curvature term $\gamma_{sv}K$ has the same units as pressure or stress, the curvature, and applied pressure effects can be treated with same formulation for the analysis of sintering.

5.2.5 Diffusional Flux Equations

For theoretical analysis of sintering, it is necessary to establish the equations for diffusional mass transport. These equations can be solved when subject to

appropriate boundary conditions. There are two equivalent formulations for sintering: diffusion of atoms or diffusion of vacancies.

In an elemental solid, if the influence of the flux of the neutral atoms can be neglected, the flux of the atoms in one dimension can be expressed as:

$$J_x = -L_{ii} \frac{d\mu}{dx}, \quad (5.86)$$

where the coefficients L_{ii} are called transport coefficients and μ is the chemical potential. By comparing this equation with the Fick's first law, i.e., Equation (5.36), there is:

$$L_{ii} = D \frac{dC}{d\mu}. \quad (5.87)$$

According to the relation between chemical potential and concentration given in Eq. (5.68), there is:

$$\mu = \mu_0 + kT \ln(\alpha C), \quad (5.88)$$

where α is the activity coefficient. For this equation, $dC/d\mu$ can be derived, which is put into Eq. (5.87), there is:

$$L_{ii} = \frac{D_i C}{kT}, \quad (5.89)$$

where D_i is given by:

$$D_i = D \left(1 + \frac{d \ln \alpha}{d \ln C} \right)^{-1}. \quad (5.90)$$

For an ideal system, α is independent of concentration, i.e., $\ln \alpha$ does not vary with $\ln C$, so that the second term in the brackets in Eq. (5.90) is zero. By putting Eq. (5.89) into Eq. (5.86), the atomic flux equation can be derived as follows:

$$J_x = - \frac{D_i C}{kT} \frac{d\mu}{dx}, \quad (5.91)$$

where D_i is given by Eq. (5.90).

5.2.5.1 Atomic Flux

In a pure elemental solid, if the point defects are only vacancies, the total number of lattice sites will not be changed, when the atoms or vacancies diffuse from one region to another. Within a given region, the changes in number of atoms and the

number of vacancies are equal and in opposite direction. The diffusional flux is dependent on the gradients, $\mu_a - \mu_v$, which follows Eq. (5.91), given by:

$$J_a = -\frac{D_a C_a}{\Omega k T} \frac{d(\mu_a - \mu_v)}{dx}, \quad (5.92)$$

where D_a is the atomic self-diffusion coefficient, k is the Boltzmann constant and C_a is the fraction of lattice sites occupied by the atoms. With appropriate boundary conditions, the diffusion response can be derived from Eq. (5.92).

5.2.5.2 Vacancy Flux

Because the atomic flux in sintering is equal and opposite to the vacancy flux, there is:

$$J_a = -J_v, \quad (5.93)$$

where J_v is given by:

$$J_v = -\frac{D_v C_v}{\Omega k T} \frac{d\mu_v}{dx} = -\frac{D_v}{\Omega} \frac{dC_v}{dx}, \quad (5.94)$$

where D_v is the vacancy diffusion coefficient. To determine J_v , it is necessary to have an expression of C_v . If C_v is the equilibrium concentration, there is:

$$\left(\frac{\partial G}{\partial n_v} \right)_{T,p,N_a} = 0, \quad (5.95)$$

so that $\mu_v = 0$. It is assumed that no externally applied pressure is applied, by putting $\mu_v = 0$ into Eq. (5.84), there is:

$$C_v = C_{0,v} \exp\left(-\frac{\gamma_{sv} K \Omega}{k T}\right), \quad (5.96)$$

where $C_{0,v}$ is a reference value, which the vacancy concentration under a flat surface. If $\gamma_{sv} K \Omega \ll k T$, Eq. (5.82) becomes:

$$C_v = C_{0,v} \left(1 - \frac{\gamma_{sv} K \Omega}{k T}\right). \quad (5.97)$$

Under the equilibrium condition, there is:

$$J_a = \frac{D_v}{\Omega} \frac{dC_v}{dx}, \quad (5.98)$$

where C_v is given by Eq. (5.97), which is a fraction of the lattice sites that are occupied by the vacancies.

5.2.6 Vapor Pressure of Curved Surfaces

During sintering process, there is an important matter transport through evaporation and condensation. The rate of the transport is proportional to the equilibrium vapor pressure over the surface, which has been related to the value of $C_a - \mu_v$ beneath the surface. If a number dN_a of atoms is taken away from the vapor and added to the surface, with a corresponding decrease in the number of vacancies beneath the surface. The free energy change due to this virtual operation must be zero, so that there is:

$$\mu_{\text{vap}} = \mu_a - \mu_v, \quad (5.99)$$

where μ_{vap} is the chemical potential of the atoms in the vapor phase. The vapor pressure is proportional to $\exp(\mu_{\text{vap}}/kT)$, so that there is:

$$p_{\text{vap}} = p_0 \exp\left(\frac{\mu_a - \mu_v - \mu_0}{kT}\right), \quad (5.100)$$

where p_0 is a reference value of the vapor pressure, corresponding to the standard value of chemical potential, μ_0 , which is generally the value over a flat surface. According to Eqs. (5.84), (5.85) and (5.96), there is:

$$\mu_a - \mu_v = \mu_0 + \gamma_{\text{SV}}K\Omega. \quad (5.101)$$

When Eq. (5.101) is put into Eq. (5.100), there is:

$$p_{\text{vap}} = p_0 \exp\left(\frac{\gamma_{\text{SV}}K\Omega}{kT}\right), \quad (5.102)$$

This is called the Kelvin equation. If $\gamma_{\text{SV}}K\Omega \ll kT$, it becomes:

$$p_{\text{vap}} = p_0 \left(1 + \frac{\gamma_{\text{SV}}K\Omega}{kT}\right). \quad (5.103)$$

This equation means that, the vapor pressure of a given system under isothermal conditions increases with increasing curvature of the surface.

5.2.7 Diffusion in Ionic Crystals—Ambipolar Diffusion

In above discussion, all the diffusing species have been assumed to be uncharged atoms or vacancies, so that electrostatic effects on the diffusion are not involved, while in practical polycrystalline ceramics, the motion of charged species, such as ions, has significant contribution to matter transport. It is also expected that different ions will have different diffusion rates. When a matter transport occurs from a given source to a given sink, the stoichiometry and electroneutrality of the solid must be preserved in the different regions of the solid, as shown in Fig. 5.9 [1]. Other effects may also have influences on the diffusion. For instance, if the system is subject to an external electric field, the ions will migrate in response to the electric field, besides the diffusion along the concentration gradient. In fact, even no external field is applied, external fields could be formed by the ions themselves, which in turn can influence their motion.

A diffusing species can have a charge z_i , e.g., $z_i = +2$ for a doubly charged magnesium ion, $z_i = +3$ for a triply charged aluminum ion, and $z_i = -2$ for a doubly charged oxygen ion, and so on. In a region with an electric potential of ϕ , the chemical potential of an ion is increased by an amount of $z_i e \phi$, where e is the magnitude of the electron charge. Without the presence of an externally pressure, according to Eq. (5.74), the chemical potential of an ion is given by:

$$\mu_i = \mu_{0,i} + kT \ln C_i + z_i e \phi, \quad (5.104)$$

where C_i is the fraction of sites occupied by the ions in the crystal. When this equation is differentiated with respect to x and is put into Eq. (5.91), the flux of the ions is given by:

$$J_{ix} = -D_i \frac{dC_i}{dx} - B_i C_i z_i e E, \quad (5.105)$$

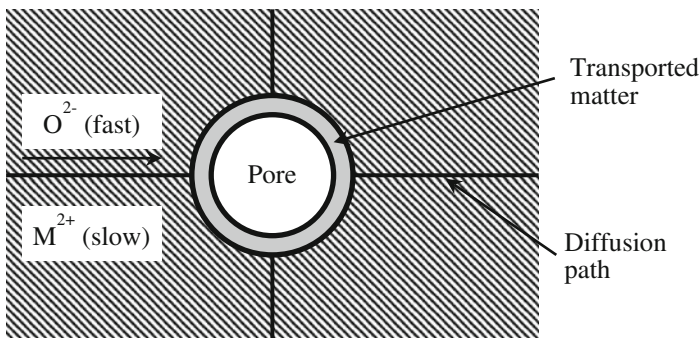


Fig. 5.9 Schematic diagram illustrating that the diffusion of ions in an ionic solid must be coupled to preserve the stoichiometry and electroneutrality of the solid. Reproduced with permission from [1]. Copyright © 2003, CRC Press

where D_i is the diffusion coefficient of the ions, $E = d\phi/dx$ is the electric field strength, and $B_i = D_i/kT$ is the ionic mobility. The first term on the right-hand side of Eq. (5.105) is the diffusion term given by the Fick's first law, while the second term is due to the ion migration caused by the electric field.

Equation (5.105) can be applied to a system, which has two different types of diffusing ions. One type has a positive charge z_+ and the other type has a negative charge z_- , corresponding to metal ions and oxygen ions in a metal oxide respectively. If no net current flows through the system, the electrical current density should be zero, so that there is:

$$z_+J_+ = -z_-J_- \quad (5.106)$$

By considering J_+ and J_- , according to Eq. (5.105), there is:

$$-\left(z_+D_+ \frac{dC_+}{dx} + B_+C_+z_+^2 eE\right) = z_-D_- \frac{dC_-}{dx} + B_-C_-z_-^2 eE \quad (5.107)$$

Rearranging Eq. (5.107) leads to an equation for E , given by:

$$E = -\frac{1}{e(B_+C_+z_+^2 + B_-C_-z_-^2)} \left(z_+D_+ \frac{dC_+}{dx} + z_-D_- \frac{dC_-}{dx} \right) \quad (5.108)$$

According to electroneutrality, there is:

$$C_+z_+ = -C_-z_- \quad (5.109)$$

By differentiating Eq. (5.109) and multiplying by D_+ , there will be:

$$z_+D_+ \frac{dC_+}{dx} = -z_-D_+ \frac{dC_-}{dx} \quad (5.110)$$

When Eq. (5.110) is put into Eq. (5.108), there is:

$$E = -\frac{1}{e(-B_+z_+C_-z_- + B_-z_-C_+z_+)} (D_- - D_+) \frac{dC_-}{dx} \quad (5.111)$$

When Eq. (5.111) for E is put into Eq. (5.105), the flux of the negative ions is given by:

$$J_- = -\frac{B_-z_-D_+ - B_+z_+D_-}{B_-z_- - B_+z_+} \frac{dC_-}{dx} \quad (5.112)$$

By replacing the ionic mobility B_i with D_i/kT , Eq. (5.112) becomes:

$$J_- = -\frac{D_+D_-(z_+ - z_-)}{D_+z_+ - D_-z_-} \frac{dC_-}{dx}. \quad (5.113)$$

When Eqs. (5.106) and (5.109) are put into Eq. (5.113), there is:

$$J_+ = -\frac{D_+D_-(z_+ - z_-)}{D_+z_+ - D_-z_-} \frac{dC_+}{dx}. \quad (5.113)$$

By analogy with the Fick's first law, an effective diffusion coefficient can be defined, which is given by:

$$\tilde{D} = \frac{D_+D_-(z_+ - z_-)}{D_+z_+ - D_-z_-}. \quad (5.115)$$

If all ions are fully ionized in Al_2O_3 , the diffusing species are Al^{3+} and O^{2-} , so that the effective diffusion coefficient is given by:

$$\tilde{D} = \frac{5D_{\text{Al}^{3+}}D_{\text{O}^{2-}}}{3D_{\text{Al}^{3+}} + 2D_{\text{O}^{2-}}}. \quad (5.116)$$

Now, if $D_{\text{O}^{2-}} \gg D_{\text{Al}^{3+}}$, there is:

$$\tilde{D} = \frac{5}{2}D_{\text{Al}^{3+}}, \quad (5.117)$$

while if $D_{\text{Al}^{3+}} \gg D_{\text{O}^{2-}}$, there is:

$$\tilde{D} = \frac{5}{3}D_{\text{O}^{2-}}. \quad (5.118)$$

Equations (5.117) and (5.118) imply that the rate of matter transport is determined by the ion that diffuses more slowly, while the motion of the slower ion is accelerated by faster diffusing ions. Therefore, the concentration gradient of the faster diffusing ion is decreased faster than that of the slower diffusing ion. Generally, only a small amount of such diffusion can build up a large potential gradient. The potential gradient has the same sign as the concentration gradient, so that it decreases the transport rate of the faster ions and increases the transport rate of the slower ions. The potential occurs is set up at the point, where the two fluxes are related by Eq. (5.106). The coupled diffusion of charged species is also called ambipolar diffusion. It has played important roles in determining the mass transport process during the sintering, as well as other mass transport processes, such as creep behaviors of materials.

On the one hand, the slower or slowest diffusing species determine the rate of matter transport. On the other hand, if each ion has multiple diffusion paths, e.g., lattice diffusion and grain boundary diffusion, matter transport will take place through the fastest path. Therefore, the rate-controlling mechanism is determined by the slowest diffusing species along the fastest path. Other factors include the differences in the effective area and path length for mass transport, which should be considered when evaluating the rate-controlling mechanism of a diffusion process.

If the lattice and grain boundary coefficients are additive, for a pure oxide M_xO_y , the effective or ambipolar diffusion coefficient is given by [20–23]:

$$\tilde{D} = \frac{(x+y)(D_1^M + \pi\delta_{gb}D_{gb}^M/G)(D_1^O + \pi\delta_{gb}D_{gb}^O/G)}{y(D_1^M + \pi\delta_{gb}D_{gb}^M/G) + x(D_1^O + \pi\delta_{gb}D_{gb}^O/G)}, \quad (5.119)$$

where δ_{gb} is the width of the grain boundary and G is the grain size. Both the effective lattice and grain boundary diffusion coefficients for one of the species are included. Equation (5.119) indicates that the slowest effective diffusion coefficient is the rate-controlling factor, whereas within each term, the faster one of the two paths dominates, i.e., the rate-controlling mechanism is determined by the slowest diffusing species coupled with its fastest path.

5.3 Solid-State and Viscous Sintering

5.3.1 Brief Description

Sintering processes can be classified into four groups: (i) solid-state sintering, (ii) liquid-phase sintering, (iii) viscous sintering, and (iv) vitrification. Sintering phenomena in polycrystalline materials are much more complex than those in viscous sintering of amorphous materials, because of the possibility of matter transport paths and the presence of grain boundaries. Matter transport in solid-state sintering can occur through at least six different paths, which determine the mechanisms of sintering. In practice, more than one mechanism could be present at any stage of sintering. Therefore, analysis of sintering rates and the determination of the sintering mechanisms becomes more difficult. The most important occurrences related to the grain boundaries are grain growth and pore growth during sintering, which is as coarsening. The coarsening process provides an alternative route to facilitate the reduction in free energy of the powder system. As a consequence, it reduces the driving force for densification. Therefore, there is a competition between sintering (densification) and coarsening.

5.3.2 Sintering Mechanisms

Diffusional transport of matter along specific paths facilitates the sintering of polycrystalline ceramics, through corresponding mechanisms. Matter is transported from the regions of higher chemical potential to the regions of lower chemical potential, with the former and latter known as the source and the sink of matter. There are at least six different mechanisms that govern the sintering of polycrystalline ceramics. Figure 5.10 shows potential mechanisms for the sintering of three spherical particles [24]. The consequence of the sintering is the bonding and growth of the necks between adjacent particles, leading to strengthening of the powder compact.

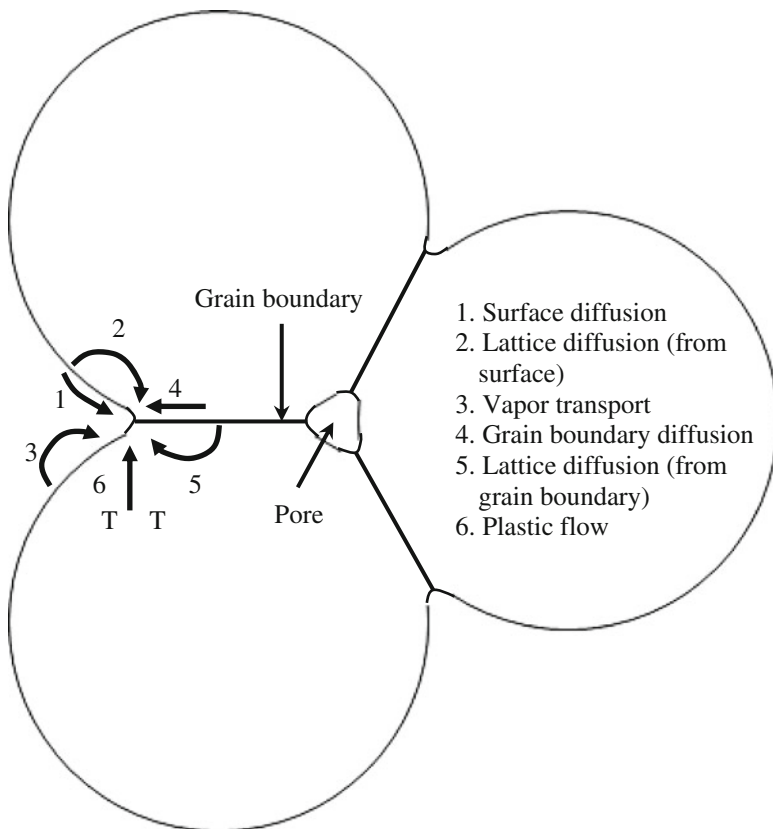


Fig. 5.10 Six distinct mechanisms can contribute to the sintering of a consolidated mass of crystalline particles: 1 surface diffusion (SD), 2 lattice diffusion from the surface, 3 vapor transport, 4 grain boundary diffusion, 5 lattice diffusion from the grain boundary, and 6 plastic flow. Only mechanisms 1 to 3 lead to densification, but all cause the necks to grow and so influence the rate of densification. Reproduced with permission from [24]. Copyright © 2007, Springer

All the mechanisms can be classified into two groups: (i) densifying mechanisms and (ii) nondensifying mechanisms, depending on whether they can cause shrinkage or densification of the compact. Nondensifying mechanisms include surface diffusion, lattice diffusion from the particle surfaces to the neck, and vapor transport, i.e., mechanisms 1, 2, and 3, which lead to neck growth without densification. In contrast, grain boundary diffusion and lattice diffusion from the grain boundary to the pore, i.e., mechanisms 4 and 5, are densifying mechanisms, which are the most important contributions to densification of polycrystalline ceramics. Diffusion from the grain boundary to the pore is benefit to both neck growth and densification. Similarly, plastic flow by dislocation motion, i.e., mechanism 6, also leads to neck growth and densification, but it is more pronounced in the sintering of metal powders. The nondensifying mechanisms reduce the curvature of the neck surface, i.e., the driving force for sintering, so as to reduce the rate of the densifying mechanisms. Therefore, they must be taken into account when discussing the sintering of ceramics. The diffusion of the different ionic species discussed above also has effect on the rate of densification.

Because amorphous materials, such as glasses, have no grain boundaries, their neck growth and densification are caused by viscous flows and the deformation of the particles. In practice, the paths of matter flows are not clearly defined. The geometrical changes caused by the viscous flow could be complex, in which the equations for matter transport can only be established with significantly simplified assumptions. The sintering mechanisms of polycrystalline and amorphous solids are summarized in Table 5.2.

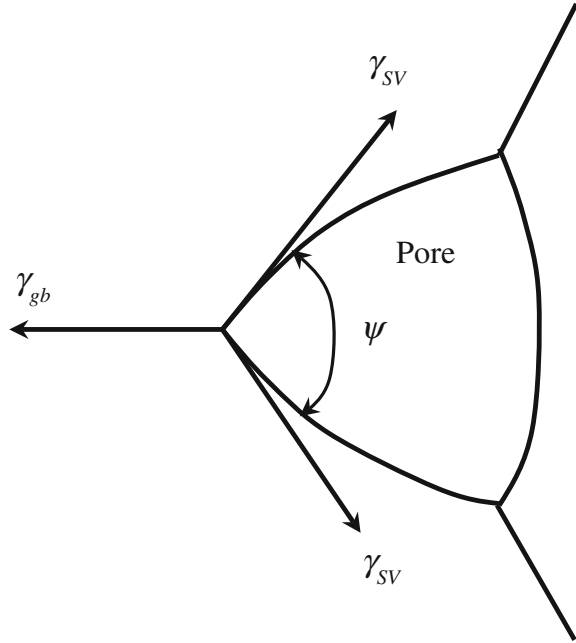
5.3.3 Grain Boundary Effects

Polycrystalline materials have grain boundaries, while amorphous materials haven't, which has been one of the most distinct difference form each other. The grain boundaries determine the equilibrium shapes of the pores and the grains in polycrystalline ceramics. Figure 5.11 shows a hypothetical pore that is enclosed by three grains [1]. The forces must balance at the junctions where the surfaces of the pores meet the grain boundary. These forces are usually represented by the tension at the interfaces, i.e., the tension in the solid–vapor interface and the tension in the

Table 5.2 Sintering mechanisms of polycrystalline and amorphous solid materials

Mechanism	Source of matter	Sink of matter	Densifying	Nondensifying
Surface diffusion	Surface	Neck		×
Lattice diffusion	Surface	Neck		×
Vapor transport	Surface	Neck		×
Grain boundary diffusion	Grain boundary	Neck	×	
Lattice diffusion	Grain boundary	Neck	×	
Plastic/viscous flow	Dislocations	Neck	×	

Fig. 5.11 The equilibrium shapes of the pores in polycrystalline solids are governed by the balance between the surface and interfacial forces at the point where the grain boundary intersects the pore. γ_{SV} is the surface tension, γ_{gb} is the grain boundary tension, and ψ is the dihedral angle. Reproduced with permission from [1]. Copyright © 2003, CRC Press



grain boundary. Similar to the surface tension of liquids, a tension is present due to the increase in energy caused by the increase in the area of the interfaces. At the junction, the tension at the solid–vapor interface is tangential to the interfaces, while that in the grain boundary is along the plane of the boundary. The balance of the forces leads to the following expression:

$$\gamma_{gb} = 2\gamma_{SV} \cos\left(\frac{\psi}{2}\right), \quad (5.120)$$

where ψ is the dihedral angle. While some sintering models consider such dihedral angles [3], it is more common to assume that the pores are sphere holes, i.e., $\psi = 180^\circ$ or $\gamma_{gb} = 0$.

During the sintering of polycrystalline materials, the decrease in energy due to the elimination of free surface area is partly compensated by the energy due to the creation of new grain boundary area, as shown in Fig. 5.10. Therefore, the driving force of sintering is lower than that calculated by using Eq. (5.3), where the grain boundaries are neglected. If ΔA_{SV} and ΔA_{gb} are used to represent the changes in the free surface area and grain boundary area, respectively, the change in energy of the system is given by:

$$\Delta E = \gamma_{SV}\Delta A_{SV} + \gamma_{gb}\Delta A_{gb}, \quad (5.121)$$

where γ_{SV} is the specific surface energy and γ_{gb} is the specific grain boundary energy. The system will evolve toward an equilibrium state governed by the condition of $|\gamma_{gb}\Delta A_{gb}| = |\gamma_{SV}\Delta A_{SV}|$. If there is $|\gamma_{gb}\Delta A_{gb}| > |\gamma_{SV}\Delta A_{SV}|$, the change in energy ΔE in Eq. (5.120) is positive. As a result, the solid–vapor surface area tends to increase, i.e., the pores tend to grow.

The presence of the grain boundaries provides an additional opportunity for the system to decrease energy, which is the decrease in the total grain boundary energy. Grain growth is usually accompanied by pore growth, with the overall process being termed as coarsening, which is present concurrently with sintering. Due to the extreme complexity, there is still no a theory of sintering that is able to analyze three-dimensional behaviors of particles and interaction among the particles, as well the concurrent densification and coarsening related to the various transport mechanisms. In most cases, densification and grain growth are analyzed separately.

5.3.4 Theory of Sintering

Various approaches have been used in the theoretical analysis of sintering. Analytical models are among the earlier attempts to develop quantitative modelings of sintering [21]. The analytical models have provided the basis for the current understanding of sintering, although simple geometry and single mechanism are often assumed. The scaling laws provide a reliable guidance for understanding the dependence of sintering mechanisms on particle size, i.e., scale [25]. Numerical simulations are effective methods, because they can be used to analyze more realistic and complicated geometries and the occurrence of multiple mechanisms. However, numerical methods have high requirement in calculations. The topological models can be used to understand the evolution of microstructure, due to their capability to predict the sintering kinetics. The statistical models and the phenomenological equations have received much less attention [20]. Sintering maps are attempted to demonstrate the changes in the sintering behavior and mechanisms under different conditions, such as temperature and particle size, which have similar limitations to the analytical models.

5.3.5 Scaling Laws

The scaling laws deal with the effect of change in scale on microstructural development during sintering [25]. During the sintering of a powder compact, the particle size is the most fundamental scaling parameter. The scaling laws do not assume a specific geometrical model, but with assumptions that (i) the particle size of the powder system remains the same and (ii) the geometrical changes remain similar. Two systems are geometrically similar, so that the linear dimension of all of the features, such as grains and pores, of system 1, $D_{sys(1)}$ is equal to a numerical factor

times the linear dimension of the corresponding features in system 2, $D_{\text{sys}(2)}$, i.e., there is:

$$D_{\text{sys}(1)} = \lambda D_{\text{sys}(2)}, \quad (5.122)$$

where λ is the numerical factor. Therefore, a simple magnification can be used to relate one system to the other, as shown schematically in Fig. 5.12 [1].

5.3.5.1 Derivation

Figure 5.13 shows a simple system with two spheres in contact, to demonstrate the derivation of the scaling laws [1]. If it takes a time Δt_1 to produce a certain microstructural change, e.g., the growth of a neck to a certain radius X_1 , in system 1, it is necessary to derive the time Δt_2 taken by system 2 to produce a geometrically similar change. For geometrically similar changes, the initial radius of the particle and the neck radius of the two systems are related by:

$$R_2 = \lambda R_1, \quad X_2 = \lambda X_1. \quad (5.123)$$

The time taken to produce a certain change by diffusional flow of matter can be expressed as:

$$\Delta t = \frac{V}{JA\Omega}, \quad (5.124)$$

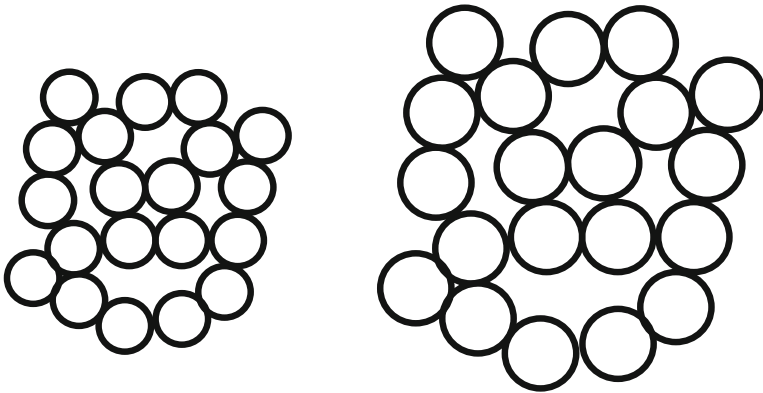
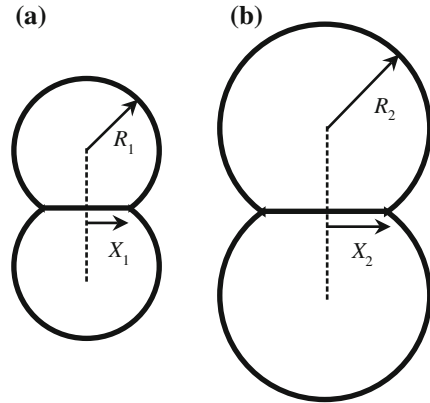


Fig. 5.12 An example of two geometrically similar systems consisting of a random arrangement of circles. The systems differ only in scale and involve a simple magnification of one relative to the other. Reproduced with permission from [1]. Copyright © 2003, CRC Press

Fig. 5.13 Geometrically similar models consisting of two spheres in contact. The linear dimensions of system 2 are a factor λ times those of system 1. **a** System 1, **b** system 2. Reproduced with permission from [1]. Copyright © 2003, CRC Press



where V is the volume of the matter transported, J is the flux, A is the cross-sectional area over which the matter is transported, and Ω is the atomic volume. Accordingly, there is:

$$\frac{\Delta t_2}{\Delta t_1} = \frac{V_2 J_1 A_1}{V_1 J_2 A_2}. \quad (5.125)$$

Equation (5.125) can be used to consider matter transport by volume diffusion.

The volume of the matter transported is proportional to R^3 , where R is the radius of the sphere shown in Fig. 5.13 [1]. As a result, V_2 is proportional to $(\lambda R)^3$, or $V_2 = \lambda^3 V_1$. For lattice diffusion, the area over which the matter diffuses is proportional to R^2 . Therefore, A_2 is proportional to $(\lambda R)^2$, or $A_2 = \lambda^2 A_1$. The flux J is proportional to $\nabla\mu$, which is the gradient of chemical potential. For a curved surface with a radius of curvature r , μ varies as a function of $1/r$. Therefore, J varies with $\nabla(1/r)$ or $1/r^2$. Because J_2 is proportional to $1/(\lambda r)^2$, there is $J_2 = J_1/\lambda^2$. Therefore, the parameters for lattice diffusion are:

$$V_2 = \lambda^3 V_1, \quad A_2 = \lambda^2 A_1, \quad J_2 = J_1/\lambda^2, \quad (5.126)$$

which are put into Eq. (5.125), yielding:

$$\frac{\Delta t_2}{\Delta t_1} = \lambda^3 = \left(\frac{R_2}{R_1}\right)^3. \quad (5.127)$$

Therefore, according to Eq. (5.127), the time taken to produce geometrically similar changes by a lattice diffusion mechanism increases as the cube of the particle size. The scaling laws for the other mass transport mechanisms can be

derived in a similar manner [25]. The laws can also be expressed in the following general form:

$$\frac{\Delta t_2}{\Delta t_1} = \lambda^m = \left(\frac{R_2}{R_1} \right)^m, \quad (5.128)$$

where m is an exponent that depends on the mechanisms of sintering. The values of m for different sintering mechanisms are listed in Table 5.3.

5.3.5.2 Application and Limitation

The scaling laws can be used to determine the dependence of the relative rates of sintering by the different mechanisms on the particle size of the powder, which is useful in controlling the microstructures during the sintering of ceramics. As mentioned earlier, some mechanisms lead to densification while others do not. Therefore, in order to achieve high density, it is necessary to increase the rates of the densifying mechanisms and decrease those of the nondensifying mechanisms.

To determine the relative rates of the different mechanisms, it is more useful to express Eq. (5.128) in terms of rate. For a given change, the rate is inversely proportional to the time, so that Eq. (5.128) can be written as:

$$\frac{(\text{Rate})_2}{(\text{Rate})_1} = \lambda^{-m}. \quad (5.129)$$

For a given powder system, if it is assumed that grain boundary diffusion and vapor transport (evaporation/condensation) are the dominant mass transport mechanisms, the rates of sintering by these two mechanisms vary with the scale of the system with the following relations:

$$(\text{Rate})_{\text{gb}} \sim \lambda^{-4}, \quad (5.130)$$

and

$$(\text{Rate})_{\text{ec}} \sim \lambda^{-2}. \quad (5.131)$$

Table 5.3 Exponents for Herring's scaling laws described by Eq. (5.128)

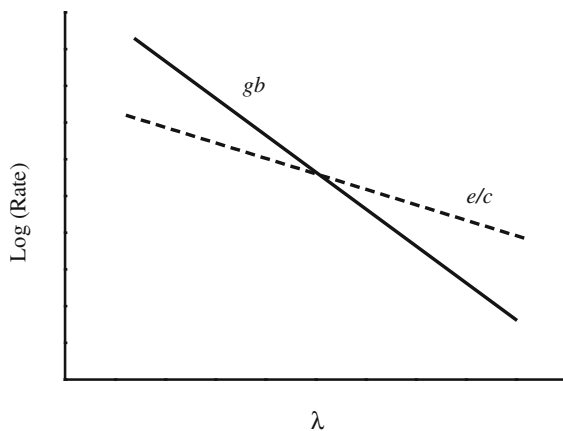
Sintering mechanism	Exponent (m)
Surface diffusion	4
Lattice diffusion	3
Vapor transport	2
Grain boundary diffusion	4
Plastic flow	1
Viscous flow	1

The variation of the rates of sintering with λ for the two mechanisms is shown in Fig. 5.14 [1]. The crossover point of the two lines is arbitrary, but it does not affect the validity of the results. For small λ , i.e., as the particle size is small, the rate of sintering by grain boundary diffusion is higher than that by vapor transport. However, the rate of sintering by vapor transport dominates for large λ , i.e., for large particle sizes. According to the scaling laws, small particle size is beneficial to densification, when grain boundary diffusion and vapor transport are the dominant mechanisms. If surface diffusion and lattice diffusion are the dominant mechanisms, similar treatment indicates that surface diffusion is enhanced as the particle size is decreased. This principle is applicable to other combinations, such as lattice diffusion versus grain boundary diffusion and surface diffusion versus grain boundary diffusion.

In the derivation of the scaling laws, on general approach and simple physical principles are employed. Because the geometric details of the powder system are not involved in the derivation, the laws are applicable to particles of any shape and to all stages of the sintering process. However, the scaling laws also have limitations. During the derivation, the particle sizes of each powder system are assumed to be unchanged during the sintering, while the microstructural changes are geometrically similar in the two systems. The second assumption is a key limitation of the scaling laws, because it is difficult to be achieved in real powder systems. For the scaling laws to be valid, the two systems should be identical in chemical composition so that the mass transport coefficients are the same.

It is noted that the exponent m in Eq. (5.128) or Eq. (5.129) is related to the mechanism of sintering, the measurement of m could provide information on the mechanism of sintering. In practice, determination of the mechanism is a challenging, due to several reasons. One of the major problems is the presence of multiple mechanisms. Therefore, the exponent that is measured experimentally could be an overall result of several mechanisms. Moreover, the sintering mechanism can vary with the size of the particles.

Fig. 5.14 Schematic diagram of the relative rates of sintering by grain boundary diffusion and by evaporation/condensation as a function of the scale (i.e., particle size) of the system. Reproduced with permission from [1]. Copyright © 2003, CRC Press



5.3.6 Analytical Methods

In the analytical models, the mass transport equations of different mechanisms are solved analytically to derive the equations of the sintering kinetics, in which a relatively simple and idealized geometry for the powder system is assumed. However, the microstructure of a real powder compact changes continuously, especially during the sintering. Therefore, it is difficult to find a single geometrical model that can describe the entire process and ensure the simplicity of analysis. To address this issue, the sintering process has to be conceptually divided into different independent stages. At each stage, an idealized geometry that has a rough similarity with the microstructure of the powder system can be assumed.

5.3.6.1 Stages of Sintering

Sintering process can be divided into three sequential stages: (i) initial stage, (ii) intermediate stage and (iii) final stage. In some analyses, an extra stage, zero stage, is included, which describes the instantaneous contact of the particles, when they are first brought together due to the elastic deformation in response to surface energy reduction at the interfaces [26]. A stage represents an interval of time or density, over which the microstructure is assumed to be reasonably well defined. For polycrystalline materials, Fig. 5.15 shows the idealized geometrical structures to represent the three stages [27, 28].

Initial Stage

The initial stage is characterized by a rapid interparticle neck growth through diffusion, vapor transport, plastic flow or viscous flow. The large differences in initial surface curvature among different particles are eliminated at this stage. Also, shrinkage or densification could be observed if the neck growth is due to the densifying mechanisms. For a powder with spherical particles, the initial stage is represented as the transition from Fig. 5.15a, b [27]. The initial stage is not finished until the radius of the neck between the particles reaches 0.4–0.5 of the particle radius. For a powder compact with an initial density of 0.5–0.6 of the theoretical density, this stage will contribute a linear shrinkage of 3–5 %, i.e., the density is increased to about 0.65 of the theoretical, if the densifying mechanisms are dominant.

Intermediate Stage

The intermediate stage starts when the pores reach their equilibrium shapes, according to the surface and interfacial tensions. The pores are still continuous. The

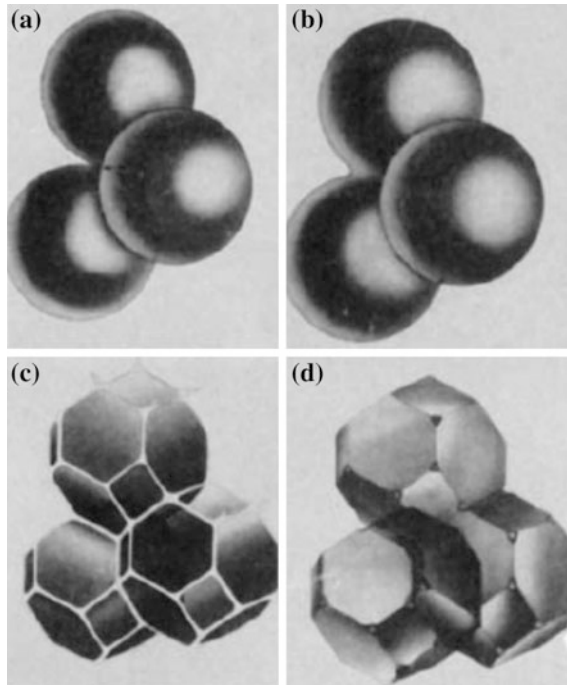


Fig. 5.15 Idealized models for the three stages of sintering. **a** Initial stage: Model structure represented by spheres in tangential contact. **b** Near the end of the initial stage: Spheres have begun to coalesce. The neck growth illustrated is for center-to-center shrinkage of 4 %. **c** Intermediate stage: Dark grains have adopted the shape of a tetrakaidecahedron, enclosing white pore channels at the grain edges. **d** Final stage: Pores are tetrahedral inclusions at the corners where four tetrakaidecahedra meet. Reproduced with permission from [27]. Copyright © 1961, American Institute of Physics

structure is usually idealized, by assuming that the pores are arranged as a spaghetti-like array and located along the grain edges, as shown in Fig. 5.15c [27]. Densification is assumed to take place only due to the shrinkage of the pores. Finally, the pores become unstable and pinch off and only those isolated pores are retained in the sintered body. At this point, the final stage is about to begin. The intermediate stage is the main contribution to the sintering process, which is ended at the relative density of 0.9.

Final Stage

The microstructural development in the final stage can occur in several ways. In a simplest case, the final stage begins when the pores pinch off and there are only isolated pores located at corners of the grains, as shown schematically in Fig. 5.15d.

Table 5.4 Parameters related to the three sintering stages of polycrystalline solids

Stage	Microstructure	Relative density	Model
Initial	Rapid interparticle neck growth	~0.65	Two monosized spheres in contact
Intermediate	Equilibrium pore shape with continuous porosity	0.65–0.9	Tetraikaidecahedron with cylindrical pores of the same radius along the edges
Final	Equilibrium pore shape with isolated porosity	>0.9	Tetraikaidecahedron with spherical monosized pores at the corners of grains

In this case, the pores are assumed to have shrunk continuously and most likely disappear altogether. Main parameters of the three sintering stages are summarized in Table 5.4.

5.3.6.2 Analytical Models

In analytical models, it is assumed that the particles in the initial powder compact are spherical with the same size and uniform packing, which is called the geometrical model [6]. With appropriate boundary conditions, the remainder of the powder system is considered as a continuum, having the same macroscopic properties, such as shrinkage and densification rate, as the isolated unit. The equations of the sintering kinetics can be derived from the established mass transport equations, which are solved under appropriate boundary conditions.

5.3.6.3 Initial Stage Models

Geometrical Parameters

The model of two equal-sized spheres, with radius of a , in contact is used for the initial stage, which is known as the two-sphere model. Two slightly different geometries are used represent the nondensifying mechanisms and the densifying mechanisms, respectively. The two-sphere model for the densifying mechanisms shows shrinkage, i.e., interpenetration of the two spheres, and thus neck growth. The neck is assumed to be circular with a radius X and a surface having a circular cross section with a radius r , which means that that the grain boundary energy is assumed to be zero. The main geometrical parameters of the model are the principal radii of curvature of the neck surface r and X , the area of the neck surface A , and the volume of material transported into the neck V , with $r \approx X^2/4a$, $A \approx \pi^2 X^3/2a$, and $V \approx \pi X^4/8a$. The parameters of the nondensifying model are only slightly different from those of densifying the model, with $r \approx X^2/2a$, $A \approx \pi^2 X^3/a$, and $V \approx \pi X^4/2a$.

Kinetic Equations

Matter transport through diffusion can be described in terms of the flux of atoms or the counterflow of vacancies. The approach based on the counterflow of vacancies driven by a vacancy concentration gradient has been used predominantly in the early development of sintering theory, which is discussed in this subsection first. More general approach based on the flux of atoms driven by a chemical potential gradient will be presented later. The following discussion is started with the mechanism of grain boundary diffusion.

According to Eq. (5.98), the flux of atoms into the neck can be determined, and thus the volume of matter transported into the neck per unit time is given by

$$\frac{dV}{dt} = J_a A_{gb} \Omega, \quad (5.132)$$

where A_{gb} is the cross-sectional area over which the diffusion takes place. Grain boundary diffusion is assumed to occur over a constant thickness δ_{gb} , so that $A_{gb} = 2\pi X \delta_{gb}$, where X is the radius of the neck. By combining Eqs. (5.98) and (5.132) and substituting A_{gb} with $2\pi X \delta_{gb}$, there is:

$$\frac{dV}{dt} = D_v 2\pi X \delta_{gb} \frac{dC_v}{dx}. \quad (5.133)$$

Because the neck radius increases radially in the direction orthogonal to a line joining the centers of the spheres, a one-dimensional solution is adequate. It is assumed that the concentration of vacancy between the neck surface and the center of the neck is constant, so that $dC_v/dx = \Delta C_v/X$, where ΔC_v is the difference in vacancy concentration between the neck surface and the center of the neck. If the concentration of vacancy at the center of the neck is assumed to be equal to that under a flat stress-free surface $C_{v,0}$, according to Eq. (5.97), there is

$$\Delta C_v = C_v - C_{v,0} = \frac{C_{v,0} \gamma_{sv} \Omega}{kT} \left(\frac{1}{r_1} + \frac{1}{r_2} \right), \quad (5.134)$$

where r_1 and r_2 are the two principal radii of curvature of the neck surface. Because there is $r_1 = r$ and $r_2 = -X$ and if it is also assumed that $X \gg r$, Eq. (5.133) becomes

$$\frac{dV}{dt} = \frac{2\pi D_v C_{v,0} \delta_{gb} \gamma_{sv} \Omega}{kTr}, \quad (5.135)$$

By using the relations of V and r , and letting the grain boundary diffusion coefficient D_{gb} to be equal to $D_v C_{v,0}$, there is

$$\frac{\pi X^3}{2a} \frac{dX}{dt} = \frac{2\pi D_{\text{gb}} \delta_{\text{gb}} \gamma_{\text{SV}} \Omega}{kT} \frac{4a}{X^2}. \quad (5.136)$$

Rearranging the equation yields

$$X^5 dX = \frac{16D_{\text{gb}} \delta_{\text{gb}} \gamma_{\text{SV}} \Omega a^2}{kT} dt. \quad (5.137)$$

By integrating and applying the boundary conditions $X = 0$ at $t = 0$, Eq. (5.137) becomes

$$X^6 = \frac{96D_{\text{gb}} \delta_{\text{gb}} \gamma_{\text{SV}} \Omega a^2}{kT} t. \quad (5.138)$$

Equation (5.138) can also be rewritten as

$$\frac{X}{a} = \left(\frac{96D_{\text{gb}} \delta_{\text{gb}} \gamma_{\text{SV}} \Omega}{kT a^4} \right)^{1/6} t^{1/6}. \quad (5.139)$$

Equations (5.138) and (5.139) predict that the ratio of the neck radius to the sphere radius increases as a function of $t^{1/6}$.

For this densifying mechanism, the linear shrinkage, defined as the change in length ΔL divided by the original length L_0 , can also be found, which is given by

$$\frac{\Delta L}{L_0} = -\frac{h}{a} = -\frac{r}{a} = -\frac{X^2}{4a^2}, \quad (5.140)$$

where h is half the interpenetration distance between the two spheres. With Eq. (5.139), the following equation can be obtained:

$$\frac{\Delta L}{L_0} = -\left(\frac{3D_{\text{gb}} \delta_{\text{gb}} \gamma_{\text{SV}} \Omega}{2kT a^4} \right)^{1/3} t^{1/3}, \quad (5.141)$$

which means that the shrinkage increase as a function of $t^{1/3}$.

The mechanism of viscous flow is discussed as follows. For this mechanism, matter transport is governed by the concept of Frenkel's energy balance, i.e., the rate of energy dissipation by the viscous flow is equal to the rate of the energy gained by the reduction in surface area, i.e., $(\text{Rate})_{\text{dis}} = (\text{Rate})_{\text{gain}}$.

With the parameters shown in Fig. 5.16 and assuming that the radius of the sphere remains roughly constant during the viscous flow, the decrease in the surface area of the two spheres is given by

$$S_0 - S = 8\pi a^2 - 4\pi a^2(1 + \cos \theta), \quad (5.142)$$

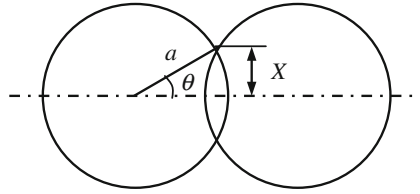


Fig. 5.16 Geometrical parameters of the two-sphere model used in the derivation of the initial stage equation for viscous sintering by Frenkel. Reproduced with permission from [1]. Copyright © 2003, CRC Press

which means that the material removed from the plane of contact is uniformly distributed over the surface of the sphere, instead of accumulating at the neck. For small values of θ , i.e., for small neck radius, $\cos\theta \approx 1 - \theta^2/2$, so that Eq. (5.142) becomes

$$S_0 - S = 2\pi a^2 \theta^2. \quad (5.143)$$

The rate of change in energy due to the reduction in surface area can be expressed as

$$\dot{E}_s = -\gamma_{SV} \frac{dS}{dt} = 4\pi a^2 \gamma_{SV} \frac{d}{dt} \left(\frac{\theta^2}{2} \right), \quad (5.144)$$

where γ_{SV} is the specific surface energy of the solid–vapor interface. According to Frenkel, the rate of energy dissipation by the viscous flow between the two spheres is given by

$$\dot{E}_v = \frac{16}{3} \pi a^3 \eta \dot{u}^2, \quad (5.145)$$

where η is the viscosity of the glass state and \dot{u} is the velocity of motion for the viscous flow which is given by

$$\dot{u} = \frac{1}{a} \frac{d}{dt} \left(\frac{a\theta^2}{2} \right) = \frac{d}{dt} \left(\frac{\theta^2}{2} \right). \quad (5.146)$$

This equation is derived with the assumption that the flow is uniform along the axis joining the centers of the spheres, rather than concentrated near the neck. By putting Eq. (5.146) into Eq. (5.145) for \dot{u} , with $\dot{E}_s = \dot{E}_v$, there is:

$$\frac{16}{3} \pi a^3 \eta \dot{u} \frac{d}{dt} \left(\frac{\theta^2}{2} \right) = 4\pi a^2 \gamma_{SV} \frac{d}{dt} \left(\frac{\theta^2}{2} \right). \quad (5.147)$$

Accordingly, the following relationship is obtained:

$$\dot{u} = \frac{3}{4} \frac{\gamma_{SV}}{\eta a}. \quad (5.148)$$

By putting Eq. (5.148) into Eq. (5.147) for \dot{u} and integrating with the boundary conditions of $\theta = 0$ at $t = 0$, there is

$$\theta^2 = \frac{3}{2} \left(\frac{\gamma_{SV}}{\eta a} \right) t. \quad (5.149)$$

Because $\theta = X/a$, where X is the neck radius, from Eq. (5.149), there is

$$\frac{X}{a} = \left(\frac{3\gamma_{SV}}{2\eta a} \right)^{1/2} t^{1/2}. \quad (5.150)$$

The equation for the shrinkage by this densifying mechanism can be also readily derived.

Equations for initial stage of sintering have been intensively studied in the open literature [20, 21, 29–32]. With the equations for neck growth and the densifying mechanisms, shrinkage can be expressed in the following general forms:

$$\left(\frac{X}{a} \right)^m = \frac{H}{a^n} t, \quad (5.151)$$

$$\left(\frac{\Delta L}{L_0} \right)^{m/2} = - \frac{H}{2^m a^n} t, \quad (5.152)$$

where m and n are numerical exponents that are dependent on the mechanisms of the sintering and H is a function that describes the geometrical and material parameters of the powder system. With the assumptions made in each model, the values for m , n , and the numerical constant in H have been derived for various models [33, 34].

According to the equations of neck growth, it is observed that the plot of $\log(X/a)$ versus $\log(t)$ is a straight line, with the slope to be $1/m$. Therefore, so by fitting experimental data with the theoretical models, the values of m will be obtained. Similarly, shrinkage can be analyzed, if it takes place during the sintering process. Usually, simple systems, such as two spheres, one sphere on a plate, or two wires for neck growth and compacts of spherical particles for shrinkage, are used to collect experimental data for validation of the theoretical models. Because m is dependent on the mechanism of sintering, it is easily concluded that the value of m can be used to identify the mechanism of sintering. However, due to the assumption of single dominant mass transport mechanism in the models, this prediction is not valid for practical material systems.

Also, the descriptions derived with the two-sphere geometry model cannot be simply applied to real powder compacts, unless the particles are spheres with the same size that are packed uniformly. The most effective approach is the assumption of a linear array of spheres for the powders with size distributions [35]. For the dihedral angle model, only when the dihedral angle is larger than 150° , the assumption that that the grain boundary energy is zero can be used as a good approximation [36]. Other assumptions, such as the redistribution of matter transport to the neck, have also been confirmed to be too simple for real sintering process [37].

5.3.6.4 Intermediate Stage Models

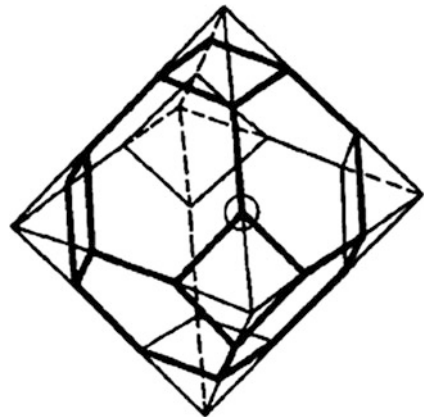
Geometrical Model

For the geometrical model of the intermediate stage, the powder is assumed to consist of a space-filling array of equal-sized tetrakaidecahedra as the particles [27]. The pores are cylindrical, with axis of the cylinder coinciding with the edge of the tetrakaidecahedra, as shown in Fig. 5.15c. The tetrakaidecahedron with cylindrical pores along its edges is taken as the unit cell of the structure. Figure 5.17 shows a tetrakaidecahedron, which is derived from an octahedron by trisecting each edge and joining the points to remove the six edges. The resulting structure has 36 edges, 24 corners, and 14 faces of 8 hexagonals and 6 squares. The volume of the tetrakaidecahedron is given by

$$V_t = 8\sqrt{2}l_p^3, \quad (5.153)$$

where l_p is the edge length of the tetrakaidecahedron. Because each pore is shared by three tetrakaidecahedras, if r is the radius of the pore, the total volume of the pores per unit cell is given by

Fig. 5.17 A tetrakaidecahedron from a truncated octahedron shown by the *dark lines*. Reproduced with permission from [27]. Copyright © 1961, American Institute of Physics



$$V_p = \frac{1}{3}(36\pi r^2 l_p). \quad (5.154)$$

The porosity of the unit cell, V_p/V_t , is therefore given by

$$P_c = \frac{3\pi}{2\sqrt{2}} \left(\frac{r}{l_p} \right)^2. \quad (5.155)$$

Because it has been assumed in the model that the pore geometry is uniform, the nondensifying mechanisms are not present. This is attributed to the fact that the chemical potential is the same everywhere on the surface of the pores. Therefore, only two densifying mechanisms should be considered: lattice diffusion and grain boundary diffusion.

Sintering Equations of Lattice Diffusion

The cylindrical pores along the edges enclose each face of the tetrakaidecahedron, as shown in Fig. 5.18a. Because the vacancy flux from the pores terminates on the faces of the boundary, as shown in Fig. 5.18b, it can be assumed the diffusion is radial from a circular vacancy source while the shape effects on the corner of the tetrakaidecahedron is neglected [27]. To remain the boundary to be flat, the vacancy flux per unit area of the boundary should be the same over the whole boundary. The diffusion flux field can be treated as that of the temperature distribution in a surface-cooled and electrically heated cylindrical conductor. The flux per unit length of the cylinder can be expressed as

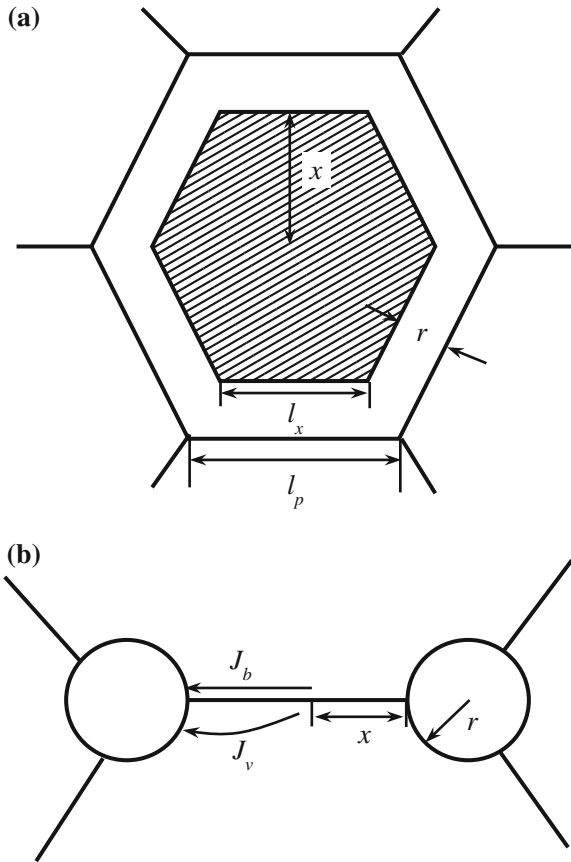
$$\frac{J}{l} = 4\pi D_v \Delta C, \quad (5.156)$$

where D_v is the vacancy diffusion coefficient and ΔC is the difference in concentration of vacancy between the pore or source and the boundary or sink. There are also several other assumptions. First, the flux equation with the dependence on the radius of the pore is not affected by the convergence of the flux to the boundary. Second, the width of the flux field, which is equivalent to l in Eq. (5.156), should be to the diameter of the pore. Third, the flux is increased by a factor of 2, due to the freedom of the vacancy diffusion flux that diverges initially, so as to provide additional available area.

With these assumptions, Eq. (5.156) becomes

$$J = 2(4\pi D_v \Delta C)2r. \quad (5.157)$$

Fig. 5.18 **a** Schematic of the hexagonal neck for intermediate stage sintering equations of polycrystalline ceramics. **b** The section shows a cut through the neck with the atomic flux paths for grain boundary and lattice diffusion. Reproduced with permission from [1]. Copyright © 2003, CRC Press



Because there are 14 faces in a tetrakaidecahedron and each face is shared by two grains, the volume flux per unit cell will be given by

$$\frac{dV}{dt} = \frac{14}{2} J = 112\pi D_v \Delta C. \tag{5.158}$$

Because of the cylindrical pore in the intermediate stage, the two principal radii of curvature are r and ∞ , so that ΔC is given by

$$\Delta C = \frac{C_{v,0} \gamma_{sv} \Omega}{kTr}. \tag{5.159}$$

By putting Eq. (5.159) into Eq. (5.158), $D_1 = D_v C_{v,0}$, where D_1 is the lattice diffusion coefficient, there is

$$dV = \frac{112\pi D_1 \gamma_{SV} \Omega}{kT} dt. \quad (5.160)$$

The integral of dV is equal to the porosity given by Eq. (5.154), which is

$$\int dV = 12\pi r^2 l_p \Big|_{r_0}^r. \quad (5.161)$$

By comparing with Eq. (5.160), there is

$$r^2 \Big|_r^0 \approx -10 \frac{D_1 \gamma_{SV} \Omega}{l_p kT} t \Big|_t^{t_f}, \quad (5.162)$$

where t_f is the time when the pore disappears. By dividing both sides of the equation by l_p^2 and evaluating the integrand, the following expression can be obtained:

$$P_c \approx \frac{r^2}{l_p^2} \approx \frac{10D_1 \gamma_{SV} \Omega}{l_p^3 kT} (t_f - t). \quad (5.163)$$

The model valid until the pores are pinched off and then isolated.

The sintering equations are commonly expressed with densification rates. Porosity P and relative density ρ are related by $P = 1 - \rho$, therefore, by differentiating Eq. (5.163) with respect to time, there is

$$\frac{d}{dt}(P_c) = -\frac{d\rho}{dt} \approx -\frac{10D_1 \gamma_{SV} \Omega}{l_p^3 kT}. \quad (5.164)$$

If l_p is assumed to be equal to the grain size G and the densification rate is expressed in the form of volumetric strain rate, Eq. (5.164) becomes

$$\frac{1}{\rho} \frac{d\rho}{dt} \approx \frac{10D_1 \gamma_{SV} \Omega}{\rho G^3 kT}. \quad (5.165)$$

This equation indicates that the densification rate at a given density is dependent inversely on the cube of the grain size, which is in agreement with the prediction by the Herring's scaling law.

Sintering Equations of Grain Boundary Diffusion

The geometrical model for lattice diffusion can be modified to derive the flux equations for grain boundary diffusion, which is

$$P_c \approx \frac{r^2}{l_p^2} \approx \left(\frac{2D_{gb}\delta_{gb}\gamma_{sv}\Omega}{l_p^4 kT} \right)^{2/3} t^{2/3}. \quad (5.166)$$

Similarly, Eq. (5.166) can be expressed as

$$\frac{1}{\rho} \frac{d\rho}{dt} \approx \frac{4}{3} \frac{D_{gb}\delta_{gb}\gamma_{sv}\Omega}{\rho(1-\rho)^{1/2} G^4 kT}. \quad (5.167)$$

At a given density, the densification rate due to the grain boundary diffusion is inversely proportional to the fourth power of the grain size, which is also coincident with predictions given by the scaling law.

5.3.6.5 Final Stage Models

For the final stage sintering models, the powder system is treated as an array of equal-sized tetrakaidecahedra with spherical pores with the same size located at the corners, as shown in Fig. 5.15d. The tetrakaidecahedron has 24 pores, with one at each corner. Because each pore is shared by four tetrakaidecahedra, the pore volume for every one tetrakaidecahedron is $V_p = (24/4)(4/3)\pi r^3$, with r being the radius of the pore. According to Eq. (5.153), the porosity per tetrakaidecahedron is given by

$$P_s = \frac{8\pi r^3}{8\sqrt{2}l_p^3} = \frac{\pi}{\sqrt{2}} \left(\frac{r}{l_p} \right)^3. \quad (5.168)$$

To be more convenient, the unit cell of the idealized structure can be treated as a thick-walled spherical shell of solid material, with a single pore of radius r to be located at the center, as shown in Fig. 5.19 [1]. The outer radius b of the spherical shell is defined in such a way that the average density of the unit cell is equal to the density of the powder system, which is

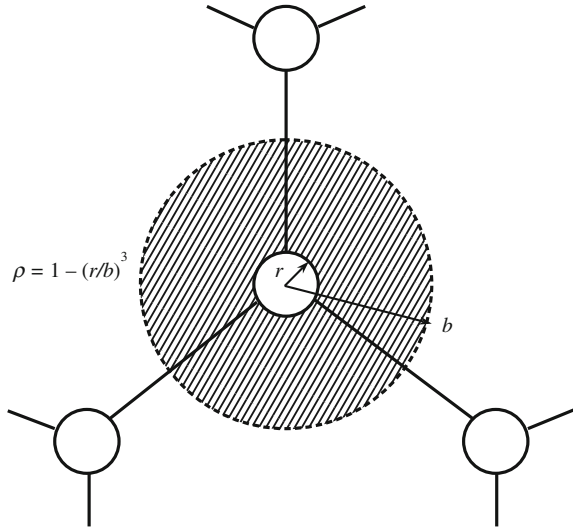
$$\rho = 1 - \left(\frac{r}{b} \right)^3. \quad (5.169)$$

The volume of the solid phase in the unit cell is $(4/3)\pi(b^3 - r^3)$. Because a unit cell contains only one pore, the number of pores per unit volume of the solid phase is given by

$$N = \frac{3}{4\pi} \frac{1-\rho}{\rho r^3}. \quad (5.170)$$

Similar assumptions are made for the final sintering stage, so that nondensifying mechanisms can be neglected, which is similar to that in the intermediate stage model [27, 38]. The procedure to derive the sintering equations for the intermediate

Fig. 5.19 A porous solid during the final stage of sintering can be modeled by constructing a spherical shell centered on a single pore. The outer radius b is chosen such that the density of the shell matches that of the porous solid. Reproduced with permission from [1]. Copyright © 2003, CRC Press



sintering stage can be used for the final stage, but with the atomic flux equation being assumed to be due to the diffusion between concentric spherical shells. The equation in terms of porosity is given by

$$P_s = \frac{6\pi}{\sqrt{2}} \frac{D_1 \gamma_{SV} \Omega}{l_p^3 kT} (t_f - t), \quad (5.171)$$

where P_s is the porosity at a time t , D_1 is the lattice diffusion coefficient, γ_{SV} is the specific energy of the solid–vapor interface, Ω is the atomic volume, l_p is the edge length of the tetrakaidecahedron that is assumed to be equal to the grain size, k is the Boltzmann constant, T is the absolute temperature, and t_f is the time when all the pores disappear. Equation (5.171) is almost the same as Eq. (5.163), with only a very small difference in the value of the numerical constant. As for the final stage sintering equation due to the grain boundary diffusion, the equation should be similar to Eq. (5.166).

5.3.7 Numerical Simulation of Sintering

Because analytical models are based on intensive assumptions, numerical simulations have been developed to provide a more comprehensive description of sintering. For example, in analytical models, it is assumed that the cross section of the neck surface is a circle to be tangential to both the grain boundary and the spherical

surface of the particle, which usually known as circle approximation. In practice, the surface curvature is always changed at the point of tangent between the neck surface and the spherical surface of the particle, so that there should be an abrupt change in chemical potential. Also, analytical models cannot deal with the sintering governed by two or more mechanisms.

5.3.7.1 Sintering

Numerical simulations of sintering with diffusion mechanisms, such as surface diffusion and grain boundary diffusion, have been conducted and reported in the literature [39–43]. In such simulations, the three-dimensional real powder systems are simplified to two-dimensional geometrical models.

Figure 5.20 shows a model consisting of a row of cylinders with same radius, whose neck contours are shown in Fig. 5.21 [40]. Two situations are simulated for matter transport by (i) surface diffusion only and (ii) both surface diffusion and grain boundary diffusion, as shown in Fig. 5.21a, b, respectively. It is found that numerical simulation predicts undercutting and a continuous change in curvature of the neck surface, which is different from that given by the analytical models with the circle approximation. The region of the neck surface influenced by the matter transport also extends far beyond that predicted by the circle approximation. However, if both the surface diffusion and grain boundary diffusion are considered, the extension is less pronounced.

There have also been reports on numerical simulation of the initial stage of sintering, involving grain boundary, lattice, and surface diffusion at the same time [36]. However, this simulation also uses the circle approximation for the neck surface. Furthermore, the chemical potential gradients for the grain boundary diffusion and the lattice diffusion are assumed to be the same. The validity of numerical simulation has been compared with other methods [44, 45].

Fig. 5.20 Geometry of the neck formed between two cylindrical particles during sintering. Reproduced with permission from [40]. Copyright © 1979, Elsevier

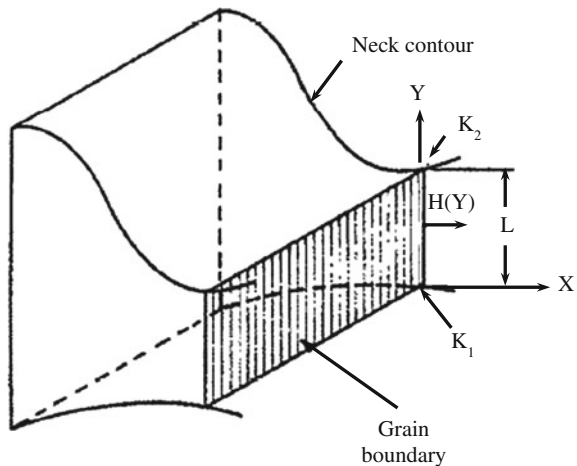
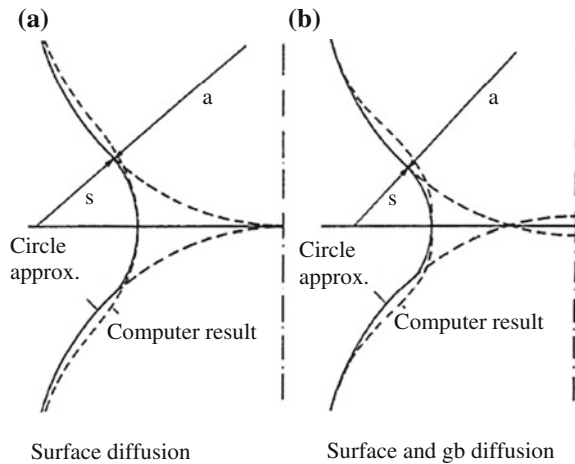
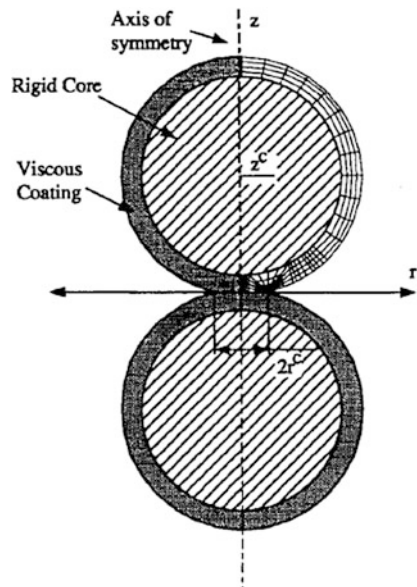


Fig. 5.21 Contours of necks between cylinders for sintering by **a** surface diffusion and **b** simultaneous surface and grain boundary diffusion. From Ref. [27]. Reproduced with permission from [40]. Copyright © 1979, Elsevier



Numerical simulation with finite element modeling has been used to study viscous sintering [42, 43, 46–50]. It is predicted that the flow is axially downward and radially outward near the neck, with most of the energy dissipated near the neck, which is in a qualitative agreement with the Frenkel model [46, 48]. Another example is the simulation of the sintering of two rigid particles that are coated with an amorphous layer, as shown in Fig. 5.22 [51]. Similar finite element modeling is used in this study. The simulation results indicate that full density can be achieved at a rate comparable to a packing of particles without a rigid core, if the coatings are sufficiently thick.

Fig. 5.22 Finite element simulation of viscous sintering of two rigid particles coated with an amorphous layer. Reproduced with permission from [51]. Copyright © 1994, John Wiley & Sons



5.3.8 Phenomenological Sintering Equations

Phenomenological approach is the development of empirical equations that can be used to fit the experimental data of sintering, in terms of density or shrinkage, as a function of time. Phenomenological sintering equations are useful to some numerical models, when equations for densification of a powder system are necessary. There is a simple expression that can be used to fit sintering and hot pressing data, which is given by

$$\rho = \rho_0 + K \ln \frac{t}{t_0}, \quad (5.172)$$

where ρ_0 is the density at an initial time t_0 , ρ is the density at time t , and K is a temperature-dependent parameter, which is known as semi-logarithmic law. Using rate equation of Coble's intermediate or final stage model for sintering through lattice diffusion, e.g., Eq. (5.165), there is [27]

$$\frac{d\rho}{dt} = \frac{AD_1\gamma_{SV}\Omega}{G^3kT}, \quad (5.173)$$

where A is a constant that is dependent on the stage of sintering. If it is assumed that the grains grow following a cubic law, i.e.,

$$G^3 = G_0^3 + \alpha t \approx \alpha t, \quad (5.174)$$

and that the initial grain size is very small, i.e., $G^3 \gg G_0^3$, Eq. (5.173) can be simplified as

$$\frac{d\rho}{dt} = \frac{K}{t}, \quad (5.175)$$

where $K = AD_1\gamma_{SV}/(\alpha kT)$. Integration of Eq. (5.175) leads to Eq. (5.172), which is expected to be valid for both the intermediate and final stages of sintering, because Eq. (5.174) has the same form for both sintering stages.

In most cases, if grain growth is significantly prohibited, shrinkage data can be fitted by the following equation:

$$\frac{\Delta L}{L_0} = Kt^{1/\beta}, \quad (5.176)$$

where K is a temperature-dependent parameter and β is an integer. This equation has the same form as the initial stage shrinkage equations derived from the analytical models.

There are also various empirical sintering equations that can be found in the open literature. One of them is as follows:

$$\frac{V_0 - V_t}{V_0 - V_f} = Kt^n, \quad (5.177)$$

where V_0 is the initial volume of the powder compact, V_t is the volume after sintering for time t , V_f is the volume of the fully dense solid, and K is a temperature-dependent parameter. Depending on materials, n has values between 0.5 and 1.0. Another equation is as follows:

$$\frac{V_t^P}{V_0^P} = (1 + C_1 mt)^{-1/m}, \quad (5.178)$$

where V_0^P is the initial pore volume of the compact, V_t^P is the pore volume after sintering for time t , while C_1 and m are constants. Although these empirical equations are successful in fitting various experimental sintering data, it is difficult for the fitted parameters to have physical meanings [52]. Therefore, it is necessary to be careful when using these empirical equations, before any meaningful understanding is available.

5.3.9 Sintering Diagrams

As discussed earlier, more than one mechanism commonly operates simultaneously during the sintering of polycrystalline systems. Besides the numerical simulations that can provide theoretical frameworks for the analysis of sintering with multiple mechanisms, sintering diagrams are even more practical approaches [33, 34]. Sintering diagrams demonstrate the dominant mechanism of sintering and the net rate of neck growth, for a given temperature and neck size, or density, to show the densification.

To construct a sintering diagram, it is necessary to have neck growth equations for specified geometrical models, usually geometrical models discussed above, and data of the material properties, such as diffusion coefficients, surface energy, and atomic volume, which included in the equations [33]. Numerical methods are used to construct the sintering diagrams, with the assumption that the total neck growth rate is the sum of all the neck growth rates for the individual mechanisms. In this respect, sintering diagrams are very close to the analytical models discussed earlier. In practice, a slight variation in the characteristics of the powders can cause significant changes in the material parameters, e.g., diffusion coefficients, so that each system should have its specific sintering diagrams.

5.3.10 Sintering at Pressures

The application of an external stress or pressure to the powder system during heating has been widely used to promote the sintering of ceramics. Various techniques have been developed for such a purpose, which can be classified into three types: (i) hot pressing, (ii) hot isostatic pressing, and (iii) hot forging. There have been models for hot pressing by considering the diffusional mass transport under the driving forces of surface curvature and applied stress [53].

5.3.10.1 Hot Pressing Models

Analytical sintering models are based on the idealized models for the three stages of sintering shown in Fig. 8.8. Because the vacancy concentration under the neck surface is not affected by the external stress, Eq. (5.134) is still valid, i.e., there is

$$\Delta C_v = C_v - C_{v,0} = \frac{C_{v,0}\gamma_{SV}\Omega}{kT} \left(\frac{1}{r_1} + \frac{1}{r_2} \right) = \frac{C_{v,0}\gamma_{SV}\Omega K}{kT}, \quad (5.179)$$

where K is the curvature of the pore surface. For the initial stage of sintering, $K = 1/r = 4a/X^2$, while for the intermediate and final stages, $K = 1/r$ and $2/r$, respectively, where r is the radius of the pores, a is the radius of the particles, and X is the radius of the neck. The stress p_a applied to the powder compact produces a stress p_e on the grain boundaries. Due to the presence of the pores, p_e is higher than p_a , which can be expressed as

$$p_e = \phi p_a, \quad (5.180)$$

where ϕ is a factor, which is also known as the stress intensification factor. The compressive stress on the grain boundary means that the concentration of vacancy is less than that of a flat stress-free boundary, so that there is

$$\Delta C_{v,b} = -\frac{C_{v,0}p_e\Omega}{kT} = -\frac{C_{v,0}\phi p_a\Omega}{kT}. \quad (5.181)$$

In the two-sphere model at the initial stage of sintering, ϕ is usually assumed to be equal to the area of the sphere projected onto the punch of the hot pressing die divided by the cross-sectional area of the neck, i.e., $\phi = 4a^2/\pi X^2$, while in those at the intermediate and final stages, it is supposed that $\phi = 1/\rho$, where ρ is the relative density of the body to be sintered.

Using the parameters for K and ϕ , the variations of $\Delta C_{v,p}$ and $\Delta C_{v,b}$ can be obtained [53]. For hot pressing, the difference in the concentration of vacancy between the neck surface and the grain boundary is given by $\Delta C = \Delta C_{v,p} - \Delta C_{v,b}$, therefore, for the initial stage, there is

$$\Delta C = \frac{C_0 \Omega 4a}{kTX^2} \left(\gamma_{SV} + \frac{p_a a}{\pi} \right). \quad (5.182)$$

This equation indicates that, at the initial stage, ΔC for hot pressing is similar to that for normal sintering, but $\gamma_{SV} + p_a a/\pi$ is used instead of γ_{SV} . Because p_a and a are constant, hot pressing equations can be derived from the sintering equations by simply changing γ_{SV} into $\gamma_{SV} + p_a a/\pi$.

Creep equations can be appropriately modified as models of intermediate and final stages of sintering. For simplicity, the matter transport during creep of a dense solid is considered first. For a pure single crystal solid with cubic structure, which is a rod with a cross section of length L . Normal stresses p_a are applied to the rod on the sides, as shown in Fig. 5.23a. It is assumed that self-diffusion within the crystal

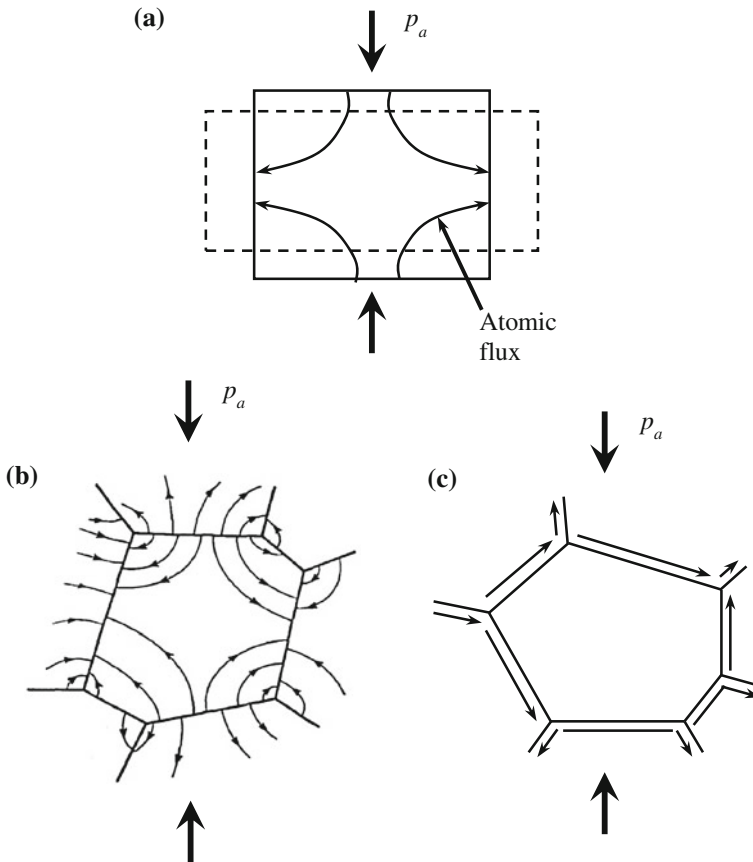


Fig. 5.23 a A single crystal subjected to a uniaxial stress, showing the direction of atomic flux. A representative grain in polycrystalline solids, showing the expected atomic flux by lattice diffusion (b) and grain boundary diffusion (c). a, c Reproduced from [1]. Copyright © 2003, CRC Press. b Reproduced with permission from [54]. Copyright © 1950, American Institute of Physics

solid causes it to deform, i.e., creep, so as to relieve the stresses [54]. During the creep, the atoms diffuse from interfaces subjected to a compressive stress, where they have a higher chemical potential, toward those regions subjected to a tensile stress, where they have lower chemical potential. This concept of creep can be extended to polycrystalline ceramics, i.e., the self-diffusion within the individual grains causes atoms to diffuse from the grain boundaries under compression toward the boundaries under tension, as shown in Fig. 5.23b. Creep by lattice diffusion is usually known as Nabarro-Herring creep, with the creep rate being given by

$$\dot{\epsilon}_c = \frac{40 D_l \Omega p_a}{3 G^2 k T}, \quad (5.183)$$

where D_l is the lattice diffusion coefficient, Ω is the atomic volume, p_a is the applied stress, G is the grain size, k is the Boltzmann constant, and T is the absolute temperature. The creep rate is a linear strain rate, defined as $(1/L)dL/dt$, where L is the length of the solid and t is time.

As shown in Fig. 5.23c, creep in ceramics can also be caused by the diffusion along the grain boundaries, with the creep equation being given by [55, 56]:

$$\dot{\epsilon}_c = \frac{47.5 D_{gb} \delta_{gb} \Omega p_a}{G^3 k T}, \quad (5.184)$$

where D_{gb} is the grain boundary diffusion coefficient and δ_{gb} is the thickness of the grain boundaries. In Eqs. (5.183) and (5.184), the creep rate is linearly dependent on p_a , which has different dependences on the grain size and different numerical constants.

If the applied stress is sufficiently high, dislocations could be produced in some ceramics, which can facilitate matter transport as a mechanism of sintering, with creep rate given by

$$\dot{\epsilon}_c = \frac{AD\mu b}{kT} \left(\frac{p_a}{\mu} \right)^n, \quad (5.185)$$

where A is a numerical constant, D is diffusion coefficient, μ is the shear modulus, and b is the Burgers vector, while the exponent n is dependent on the mechanism of the dislocation motion, with values in the range of 3–10.

Hot pressing equations can be derived from the creep equations with certain modifications. In practices, sintering data are usually present as density versus time to obtain densification rate. Because sintering compacts are porous before they are fully densified, the creep equations developed for dense solids should be modified to be suitable for hot pressing equations. First, the creep rate that is a linear strain rate should be related to the densification rate which is a volumetric strain rate. Second, the porosity should be compensated. In hot pressing, the mass M of the powder and the cross-sectional area A of the die, are constants, while the density

D increases and the sample thickness L decreases, with the relation of D and L being given by

$$\frac{M}{A} = LD = L_0D_0 = L_fD_f, \quad (5.186)$$

where the subscripts 0 and f stand for the initial and final states. Differentiating Eq. (5.186) with respect to time gives

$$L \frac{dD}{dt} + D \frac{dL}{dt} = 0. \quad (5.187)$$

Rearranging Eq. (5.187), there is:

$$-\frac{1}{L} \frac{dL}{dt} = \frac{1}{D} \frac{dD}{dt} = \frac{1}{\rho} \frac{d\rho}{dt}, \quad (5.188)$$

where ρ is relative density. Equation (5.188) indicates that the densification rate is related to the linear strain rate of the body during the hot pressing. The linear strain rate can be measured directly by monitoring movement of the punch during the hot pressing.

In Coble's initial stage hot pressing model, the effective stress applied to the grain boundaries, p_e , is related to the externally applied stress, p_a , which is by Eq. (5.180). In that model, the total driving force (DF) is a linear combination of two effects: (i) external applied stress and (ii) surface curvature, which determines the densification rate, and it is

$$DF = p_e + \gamma_{SV}K = p_a\phi + \gamma_{SV}K, \quad (5.189)$$

where K is the curvature of the pore, which is equal to $1/r$ for intermediate stage model and $2/r$ for final stage model of the sintering. When this DF is used to replace the applied stress p_a in the creep equations for dense solids, hot pressing equations for sintering can be derived.

The modified creep equations should be further elaborated for real scenario of hot pressing sintering of ceramics, due to the differences between the two processes, such as those in the atomic flux field and the path length for diffusion. For example, in the creep models, the atomic flux is terminated at the grain boundaries under tension, while in hot pressing it is terminated at the surfaces of pores. During the creep of dense solids, because the grain size is not changed, the areas of grain boundaries are kept unchanged. However, during the hot pressing sintering, but both the areas of the grain boundaries and the path length for diffusion are increased with time.

5.3.10.2 Hot Pressing Mechanisms

There is no significant difference in mechanism between the normal sintering and hot pressing sintering. However, due to the application of an external stress, the densifying mechanisms are largely enhanced, while the nondensifying mechanisms are almost not affected. Therefore, it is not necessary to consider all the nondensifying mechanisms. This difference in the effect of the applied stress can be used to identify the mechanisms of densification, on the one hand, while on the other hand, new densification mechanisms could be brought out.

Figure 5.24 shows a schematic cross-sectional view of a representative system, consisting of three grains with an ideal hexagonal shape [1]. This diagram can be used to describe the overall shape change of powder compacts during hot pressing. Within the hot pressing die with fixed diameter, the powder compact would contract only in the direction of the external pressure, thus leading to flattening of the grains, as shown in Fig. 5.24, which is accompanied by sliding of grains and grain boundaries. Therefore, the major mechanisms that govern the sintering during hot pressing include rearrangement, lattice diffusion, grain boundary diffusion, viscous flow, plastic deformation through dislocation motion and grain boundary sliding.

If the applied stress is much higher than the driving force due to the curvature, the densification rate during hot pressing can be expressed as

$$\frac{1}{\rho} \frac{d\rho}{dt} = \frac{HD\phi^n}{G^m kT} P_a^n, \quad (5.190)$$

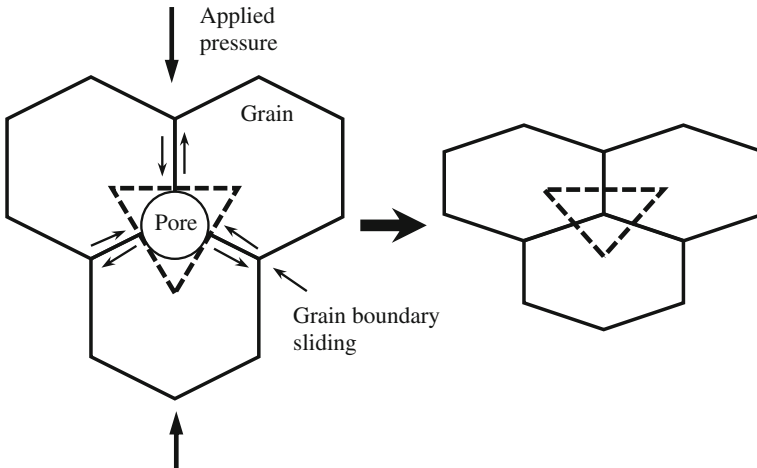


Fig. 5.24 Sketch illustrating the change in shape of the grain that occurs during hot pressing. The grains are flattened in the direction of the applied pressure. When matter transport occurs by diffusion, grain boundary sliding is necessary to accommodate the change in grain shape. Reproduced with permission from [1]. Copyright © 2003, CRC Pressing

where H is a numerical constant, D is the diffusion coefficient of the rate-controlling species, ϕ is the stress intensification factor, G is grain size, k is the Boltzmann constant, T is absolute temperature, while the exponents m and n are dependent on the mechanism of the densification. For example, lattice diffusion mechanism has $m = 2$ and $n = 1$, while for grain boundary diffusion, there are $m = 3$ and $n = 1$.

Equation (5.190) indicates that the plot of densification rate versus p_a can be used to derive the exponent n , so that the mechanism of densification can be identified. The applied pressures for commonly used hot pressing are 10–50 MPa, with which $n \approx 1$ is usually observed for many ceramics, corresponding to the diffusion mechanism for densification [57, 58]. High values of n are occasionally observed, indicating the possibility of dislocation mechanisms [59, 60]. The dominant densification mechanism can be varied with the applied pressure, temperature, and grain size. Similar to the sintering maps discussed above, there are also hot pressing maps to demonstrate the dominant mechanisms versus processing conditions.

5.3.11 Stress Intensification Factor

As mentioned before, there is an important factor, ϕ , in the hot pressing models, which is known as stress intensification factor or stress multiplication factor. It is used to relate the mean stress applied to the grain boundary, p_e , to the externally applied stress, p_a . The significance of ϕ is such that while p_a is the stress that is measured, p_e is its counterpart that influences the rate of matter transport. The factor ϕ is geometrically dependent on the porosity and the shape of the pores of the ceramic compacts.

When a hydrostatic pressure p_a is applied to the external surface of a powder compact, it can be represented by using a model, as shown schematically in Fig. 5.25a [1]. In this case, the applied pressure exerts a load on the surface of the solid, which is $F_a = A_T p_a$, where A_T is the total external cross-sectional area of the solid, including areas pores. Due to presence of porosity at the grain boundaries, the actual grain boundary area A_e is smaller than the total external area. If a force balance is maintained across any plane of the solid, the following expression is valid:

$$p_a A_T = p_e A_e. \quad (5.191)$$

Therefore, stress intensification factor is given by

$$\phi = \frac{p_e}{p_a} = \frac{A_T}{A_e}. \quad (5.192)$$

If the pores are assumed to be spherical and randomly distributed in a porous solid, the factor ϕ can be obtained through the following steps. It is assumed that there is

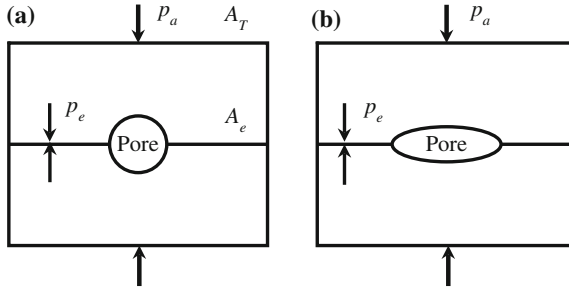


Fig. 5.25 **a** The effective stress applied to the grain boundary p_e is higher than the externally applied stress p_a , due to the presence of the pores at the grain boundaries. The stress intensification factor ϕ is defined as the ratio of the total external area to the actual grain boundary area. **b** ϕ is dependent on the porosity and the pore shape, with stronger dependence on porosity for pores with smaller dihedral angles, e.g., elliptical pores. Reproduced with permission from [1]. Copyright © 2003, CRC Press

an arbitrary plane through the solid, with the area fraction of porosity in the plane being equal to the volume fraction of porosity in the solid. If A_T is unity, there is $A_e = 1 - P$, where P is the porosity of the solid. Because $1 - P$ is also equal to the relative density, there is the following relation:

$$\phi = \frac{1}{\rho}. \quad (5.193)$$

This equation is valid for polycrystalline ceramics with equilibrium shapes of the isolated pores to be nearly spherical, i.e., dihedral angles are larger than 150° . Once the pores become nonspherical, the expression of ϕ could have very complicated form. If the shapes of the pores are dramatically changed, as shown in Fig. 5.25b [1], although the volume is the same, the value of ϕ could be changed, because it is now dependent on not only the porosity but also the shape of the pores. When the pore shape is not spherical, the dihedral angles are reduced, so that the actual area of the grain boundary is decreased, therefore, ϕ will be decreased.

An analysis of simulation results of a continuous network of pores with equilibrium shapes indicates that ϕ can be approximated using a simple expression, which is [59, 61, 62]:

$$\phi = \exp(\alpha P), \quad (5.194)$$

where α is a factor that is dependent on the dihedral angle and P is the porosity. The factor α can be determined with simulation results, while the equation has been verified by some experimental results. However, further studies are necessary to increase the significance of ϕ [63–66].

5.3.12 Sintering Stress

The densification rate for the diffusion-controlled mechanisms may be expressed as a general form, which is given by

$$\frac{1}{\rho} \frac{d\rho}{dt} = -\frac{3}{L} \frac{dL}{dt} = \frac{3}{\eta_\rho} (p_a \phi + \sigma), \quad (5.195)$$

where $(1/L)dL/dt$ is the linear strain rate of the sintering compact, η_ρ has the dimensions of a viscosity that can be called densification viscosity, while σ is the effective stress applied to the atoms under the pore surface, which is given by the Young and Laplace equation:

$$\sigma = \gamma_{SV} \left(\frac{1}{r_1} + \frac{1}{r_2} \right), \quad (5.196)$$

where r_1 and r_2 are the two principal radii of curvature of the pore surface. The quantity σ is the thermodynamic driving force for sintering. It has the units of a pressure or stress, which is usually known as sintering pressure or sintering potential. The equation of σ is actually more complex for polycrystalline ceramics, because the pores are in contact with the grain boundaries. It has two contributions, one from the pores and the other from the grain boundaries [67]. For an idealized final stage microstructure, where the pores and grains are assumed to be spherical in shape, σ is given by [68]

$$\sigma = \frac{2\gamma_{gb}}{G} + \frac{2\gamma_{SV}}{r}, \quad (5.197)$$

where γ_{gb} is the specific energy of the grain boundary, G is the grain size, and r is the radius of the pore. The driving force for sintering is also influenced by the dihedral angle and the mass transport mechanism, which has been calculated for a simple geometry, consisting of a line of spherical particles [69].

Another form of Eq. (5.195) is

$$\frac{1}{\rho} \frac{d\rho}{dt} = \frac{3\phi}{\eta_\rho} (p_a + \Sigma), \quad (5.198)$$

where $\Sigma = \sigma/\phi$ has the units of stress, which known as sintering stress. Because Σ has a linear relationship with the externally applied stress p_a , it can be used to represent the equivalent externally applied stress, with an effect on sintering as same as those of the curved surfaces of pores and grain boundaries.

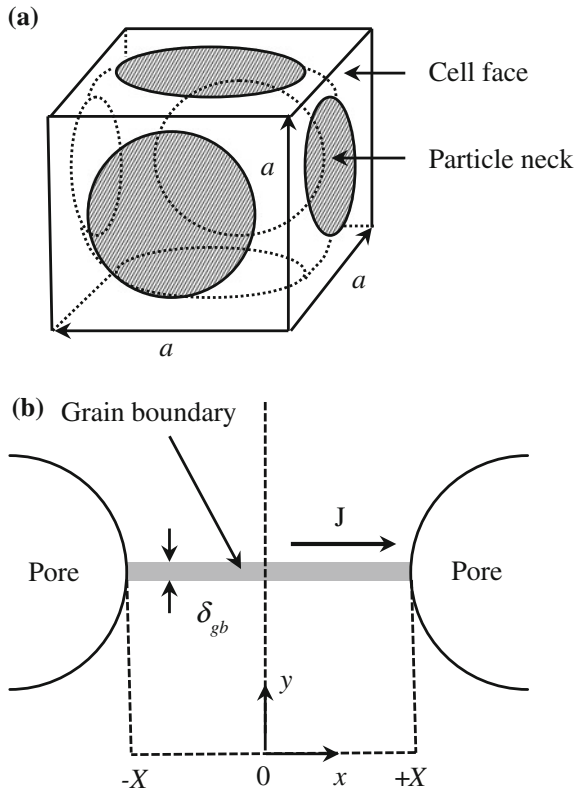
5.3.13 Alternative Sintering Equations

Besides those discussed above, the sintering equations can be derived in an alternative way by solving the differential equations of the atomic flux that is subject to appropriate boundary conditions [70].

5.3.13.1 Grain Boundary Diffusion

A simple geometrical model consisting of spherical particles with a diameter a , arranged as a simple cubic pattern, as shown in Fig. 5.26a, is used to derive the sintering equations for the mechanism of grain boundary diffusion [70]. It is

Fig. 5.26 **a** Schematic of the cell surrounding a spherical particle showing the neck or grain boundary section with an adjoining particle. Reproduced with permission from [70]. Copyright © 1991, John Wiley & Sons.
b Geometrical parameters for matter transport through grain boundary diffusion. Reproduced with permission from [1]. Copyright © 2003, CRC Press



assumed that the grain boundary is flat, with a constant width δ_{gb} , as shown in Fig. 5.26b [1]. From Eq. (5.92), the flux of atoms as a function of distance along the neck can be expressed as

$$j(x) = -\frac{D_{\text{gb}}}{\Omega kT} \nabla \mu, \quad (5.199)$$

where D_{gb} is the grain boundary diffusion coefficient, Ω is the atomic volume, k is the Boltzmann constant, T is the absolute temperature, and μ is the chemical potential of the atoms. The total number of atoms crossing the neck at a radius x per unit time is given by

$$J(x) = 2\pi x \delta_{\text{gb}} j(x) = -\frac{2\pi x D_{\text{gb}} \delta_{\text{gb}}}{\Omega kT} \nabla \mu. \quad (5.200)$$

Because the displacement of the boundary must be independent of x , the rate to approach of the centers of the particle, dy/dt , is related to $J(x)$ through the following expression:

$$J(x) = \frac{\pi x^2}{\Omega} \frac{dy}{dt}. \quad (5.201)$$

From Eqs. (5.200) and (5.201), there is

$$\frac{d\mu}{dx} = -2Ax, \quad (5.202)$$

where

$$A = -\frac{kT}{4D_{\text{gb}} \delta_{\text{gb}}} \frac{dy}{dt}. \quad (5.203)$$

Integrating Eq. (5.202) yields:

$$\mu(x) = -Ax^2 + B, \quad (5.204)$$

where B is a constant. The chemical potential μ is related to the normal stress applied to the boundary σ by $\mu = \sigma\Omega$, so that Eq. (5.204) becomes

$$\sigma(x) = \frac{-Ax^2 + B}{\Omega}, \quad (5.205)$$

where the constants A and B can be derived from the corresponding boundary conditions. For the first boundary condition, the stresses must be balanced at $x = X$ and $x = -X$. According to the definition of sintering stress, the effects of the pores and grain boundaries are replaced by using an equivalent external stress Σ . Therefore, the stress applied to the surface of the pore should be equal to zero. In

this case, the second boundary condition is $\sigma = 0$ at $x = \pm X$. Substituting either of them into Eq. (5.205) yields

$$B = Ax^2. \quad (5.206)$$

The second boundary condition also means that the average stress applied to the grain boundary is equal to $\phi\Sigma$, where ϕ is the stress intensification factor. This condition can be expressed as

$$\frac{1}{\pi X^2} \int_0^{2\pi} \int_0^x \sigma(x) dx d\theta = \phi\Sigma. \quad (5.207)$$

Substituting $\sigma(x)$ and integrating the equation yield

$$-\frac{AX^2}{2} + B = \Omega\phi\Sigma. \quad (5.208)$$

Together with Eq. (5.206), there are

$$A = \frac{\Omega\phi\Sigma}{X^2}, \quad B = 2\Omega\phi\Sigma. \quad (5.209)$$

From Eq. (5.200), the total flux at the surface of the neck between two particles is thus given by

$$J(X) = \frac{8\pi D_{\text{gb}} \delta_{\text{gb}} \phi\Sigma}{kT}. \quad (5.210)$$

When $J(X)$ is related to the shrinkage of the system, the total volume transported out of one neck in a time Δt is given by

$$\Delta V = -J(X)\Omega\Delta t = \pi X^2 \Delta a, \quad (5.211)$$

where Δa is the corresponding change in the center-to-center distance between the particles. The total volumetric shrinkage in all three orthogonal directions is given by

$$\frac{\Delta V}{V} = \frac{3\Delta a}{a}, \quad (5.212)$$

and because $V = a^3$, the rate of change of the cell volume is given by

$$\frac{dV}{dt} = \frac{\Delta V}{\Delta t} = 3a^2 \frac{\Delta a}{\Delta t}. \quad (5.213)$$

From Eq. (5.211), $\Delta a/\Delta t$ is obtained, which is put into Eq. (5.213), there is

$$\frac{dV}{dt} = -3a^2 \frac{J(X)\Omega}{\pi X^2}. \quad (5.214)$$

By definition, $\phi = a^2/(\pi X^2)$, so that the instantaneous volumetric strain rate is given by

$$\frac{1}{V} \frac{dV}{dt} = -\frac{3J(X)\Omega\phi}{a^3}. \quad (5.215)$$

The linear densification strain rate $\dot{\epsilon}_\rho$ is defined as $(-1/3 V) dV/dt$, which is used to substitute $J(X)$ in Eq. (5.210), there is

$$\dot{\epsilon}_\rho = \frac{8\pi D_{\text{gb}}\delta_{\text{gb}}\Omega}{a^3 kT} \phi^2 \Sigma. \quad (5.216)$$

5.3.13.2 Lattice Diffusion

The sintering equation for lattice diffusion can be derived in a similar way. The linear densification strain rate can also be derived from Eq. (5.216) by replacing $\pi D_{\text{gb}}\delta_{\text{gb}}$ with $2XD_1$, where D_1 is the lattice diffusion coefficient [71]. Because there is $\phi = a^2/(\pi X^2)$, the linear densification strain rate is given by

$$\dot{\epsilon}_\rho = \frac{16D_1\Omega}{\pi^{1/2}a^2 kT} \phi^{3/2} \Sigma. \quad (5.217)$$

5.3.13.3 General Isothermal Sintering Equation

For matter transport by diffusion, a general equation for the linear densification strain rate can be expressed as

$$\dot{\epsilon}_\rho = \frac{H_1 D \Omega \phi^{(m+1)/2}}{G^m kT} (\Sigma + p_h), \quad (5.218)$$

where H_1 is a numerical constant that is dependent on the geometry of the model, p_h is the hydrostatic component of an externally applied stress, G is the particle or grain size, k is the Boltzmann constant, T is the absolute temperature, and Ω is the atomic volume. At the same time, $D = D_{\text{gb}}\delta_{\text{gb}}$ and $m = 3$ for grain boundary diffusion, while $D = D_1$ and $m = 2$ for lattice diffusion.

5.4 Liquid-Phase Sintering

5.4.1 *Brief Introduction*

The sintering processes discussed above are all solid-state sintering, in which the materials remain in solid state throughout the sintering process. However, if there is a liquid phase present during the sintering, the sintering process can be significantly enhanced, which is known as liquid-phase sintering [72]. Usually, liquid-phase sintering is used to enhance densification rates, achieve accelerated grain growth, or produce specific grain boundary properties. The distributions of the liquid phase and the resulting solidified phases produced on cooling after densification are critical to achieving the required properties of the sintered ceramics. In most cases, the amount of liquid formed during sintering should be small, which can make it quite difficult to precisely control the composition of the liquid.

Liquid-phase sintering is more effective for ceramics that have a high degree of covalent bonding, and thus are difficult to densify through solid-state sintering. A disadvantage of liquid-phase sintering is the formation of glassy intergranular phase due to the solidification of the liquid phase, which could degrade the properties of the final ceramics. Because optical properties are especially sensitive as compared with other properties, it should be very careful when using liquid-phase sintering to process transparent ceramics.

A related process is called activated sintering, in which the additives segregate at grain boundaries to enhance the mass transport rates and thus accelerate densification. If sufficient amount of liquid is present with contents in the range of 25–30 vol.%, rearrangement of the solid phase coupled with liquid flow can lead to a fully dense material. Such large volume fractions of liquid are rarely used in transparent ceramics. In this case, the sintering process is known as vitrification.

5.4.2 *Characteristics of Liquid-Phase Sintering*

5.4.2.1 **Densification Enhancement**

The enhancement in densification during the liquid-phase sintering can be attributed to the (i) enhanced rearrangement of particles due to surface wetting effect and (ii) enhanced matter transport through the liquid due to its low viscosity. The microstructural characteristics of liquid-phase sintering can be compared with those of solid-state sintering by using the idealized two-sphere model, as shown in Fig. 5.27 [1]. If the liquid phase can wet the particles and has sufficient quantity to cover the particle surfaces, all the particles are separated one another by a liquid layer, which can greatly decrease the friction between every two adjacent particles. As a result, the particles would have higher mobility, thus making their rearrangement more easily. In contrast, solid-state sintering has no such effect. For grain boundary

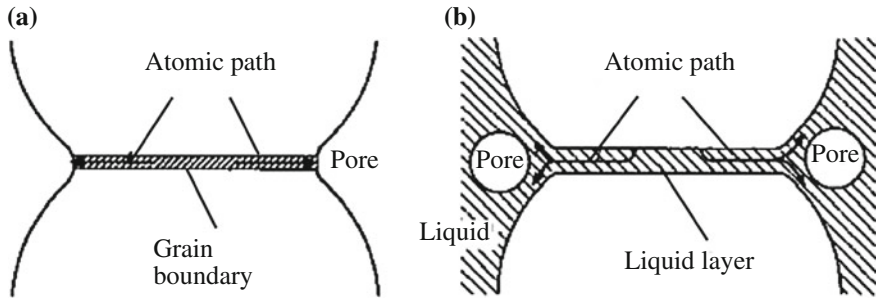


Fig. 5.27 Schematic diagrams of the idealized two-sphere model showing microstructural characteristics of **a** solid-state sintering and **b** liquid-phase sintering. Reproduced with permission from [1]. Copyright © 2003, CRC Press

diffusion, the rate of diffusion for solid-state sintering is controlled by the product of the grain boundary diffusion coefficient D_{gb} and the grain boundary thickness δ_{gb} , whereas that for liquid-phase sintering is determined by the product of the diffusion coefficient D_L of the species in the liquid and the thickness of the liquid layer δ_L . Because $\delta_L > \delta_{gb}$ and $D_L > D_{gb}$, $\delta_L D_L \gg \delta_{gb} D_{gb}$, i.e., the liquid can promote matter transport.

5.4.2.2 Driving Force for Densification

Because the liquid wets and spreads over the solid surfaces, pores will be formed in the liquid. The reduction of the liquid–vapor interfacial area provides the driving force for shrinkage or densification of the compact. If the pore in the liquid is assumed to be spherical with radius of r , the pressure difference across the curved surface is given by the Young and Laplace equation:

$$\Delta p = -\frac{2\gamma_{LV}}{r}, \quad (5.218)$$

where γ_{LV} is the specific surface energy of the liquid–vapor interface. The pressure applied to the liquid phase is lower than that applied to the pore, which leads to a compressive capillary stress to the particles. Therefore, the effect of the compressive stress due to the liquid is equivalent to the application of an external hydrostatic pressure to the system, as the driving force for sintering.

5.4.2.3 Formation of Liquid Phase

The formation of liquid phase during the liquid-phase sintering is schematically shown in Fig. 5.28 [73]. It is started from a mixture of two powders, i.e., the major component and an additive. The additive is molten to liquid phase or reacts with the

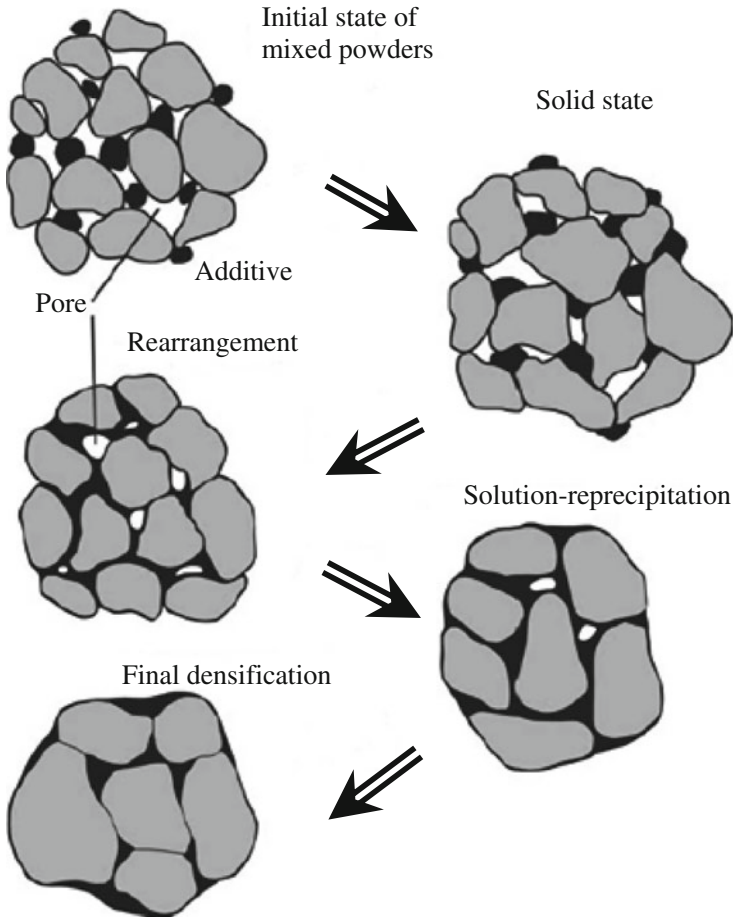


Fig. 5.28 Schematic of the microstructure variation in a liquid-phase sintering, starting with mixed powders, and pores between the particles. During heating the particles are sintered, but when a melt forms and spreads, the solid grains rearrange. Subsequent densification is accompanied by coarsening. In many cases, there is pore annihilation as diffusion in the liquid to accelerate the change in grain shape, so that pores are removed. Reproduced with permission from [73]. Copyright © 2009, Springer

major component to form a eutectic liquid. If it is preferred to form eutectic liquids, the additive and the firing conditions should be properly selected. Due to the small quantity of the liquid phase, the structure of the compact can be well remained, because the particles are held together by the capillary stress created by the liquid. However, the system has lower effective viscosity than its counterparts without a liquid phase. If the liquid is present throughout the sintering process, it is called persistent liquid-phase sintering, where the liquid precipitates at grain boundaries as glass phase after the sintering. Otherwise, it is called transient liquid-phase sintering, in which the liquid might disappear due to (i) incorporation into the solid

phase to form solid solutions, (ii) formation of crystal phase through crystallization, or (iii) evaporation.

5.4.2.4 Microstructures

The ceramics fabricated using liquid-phase sintering contains two phases, i.e., (i) the major phase of crystalline grains and (ii) the grain boundary phase resulting from the liquid. In most cases, the grain boundary phase is amorphous. The quantity of the liquid phase determines the characteristics of the grain boundaries and thus the properties of the grains, such as grain shape, size, and morphology.

5.4.3 Stages of Liquid-Phase Sintering

Because chemical reactions between the particles and the liquid phase can be neglected, the sintering rate is mainly controlled by the interfacial energies. In this case, liquid-phase sintering generally has three stages, as shown in Fig. 5.28 [73]. The first stage is the rearrangement of the particles caused by the capillary stress gradients due to the redistribution of the liquid phase. At the second stage, the compact experiences densification, through the solution-re/precipitation process. Finally, the compact undergoes grain coarsening and further densification before the whole sintering is finished.

5.4.4 Thermodynamic and Kinetic Factors

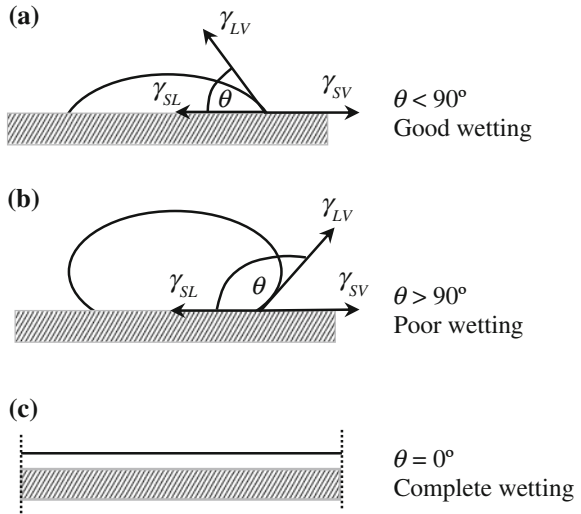
Several kinetic and thermodynamic factors, as well as processing parameters, determine the microstructures of the ceramics by using liquid-phase sintering.

5.4.4.1 Wetting and Spreading of the Liquid

The capability of the liquid to wet and spread over the surface of the solid particle determines the effectiveness of liquid-phase sintering. The wetting capability of a liquid is dependent on its surface tension, i.e., lower the surface tension, the high the wetting capability the liquid has, which is usually characterized by a parameter, known as contact angle.

The contact angle is determined by the various interfacial energies of the solid–liquid–vapor systems, which is demonstrated using a droplet of liquid on the surface of a flat solid, as shown schematically in Fig. 5.29. When the specific energies

Fig. 5.29 Wetting behavior between a liquid and a solid showing **a** good wetting, **b** poor wetting, and **c** complete wetting for a liquid with a contact angle of θ



of the liquid–vapor, solid–vapor, and solid–liquid interfaces are represented with γ_{LV} , γ_{SV} , and γ_{SL} , respectively, at equilibrium state, there is

$$\gamma_{SV} = \gamma_{SL} + \gamma_{LV} \cos \theta. \tag{5.219}$$

Therefore, the contact angle is given by

$$\cos \theta = \frac{\gamma_{SV} - \gamma_{SL}}{\gamma_{LV}}. \tag{5.220}$$

5.4.4.2 Dihedral Angle

Figure 5.30 shows a two-dimensional diagram for a liquid in contact with the corner of two grains, where the grain boundaries intersect the surface of the liquid [73]. The angle between the solid–liquid interfacial tensions is defined as dihedral angle. Similar to Eq. (5.220), the dihedral angle can be obtained by the following expression:

$$\cos \frac{\psi}{2} = \frac{\gamma_{SS}}{2\gamma_{SL}}. \tag{5.221}$$

The solid–solid interfacial tension γ_{SS} is the same as the interfacial tension in the grain boundary γ_{gb} in the solid-state sintering.

The penetration of the liquid into the grain boundary is described by the dihedral angle ψ , which is determined by the ratio γ_{SS}/γ_{SL} . With $\gamma_{SS}/\gamma_{SL} < 2$, the dihedral angle has values of 0–180° and the liquid cannot penetrate the grain boundary, as shown in Fig. 5.31 [74]. In this case, solid-state processes are actually dominant.

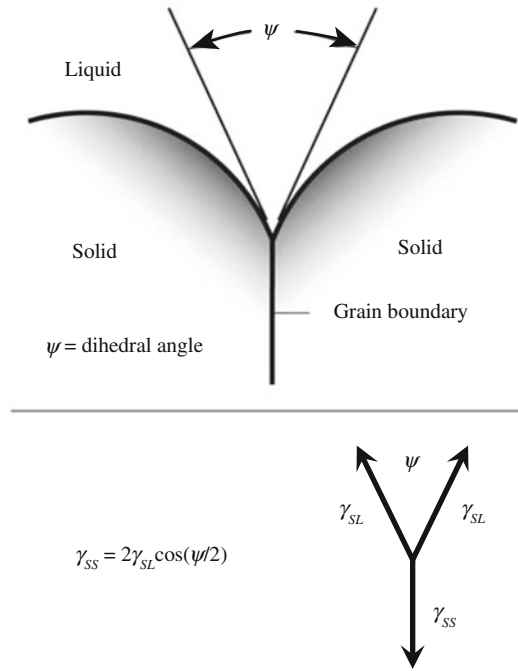


Fig. 5.30 Dihedral angle ψ for a liquid at a grain boundary. Reproduced with permission from [73]. Copyright © 2009, Springer

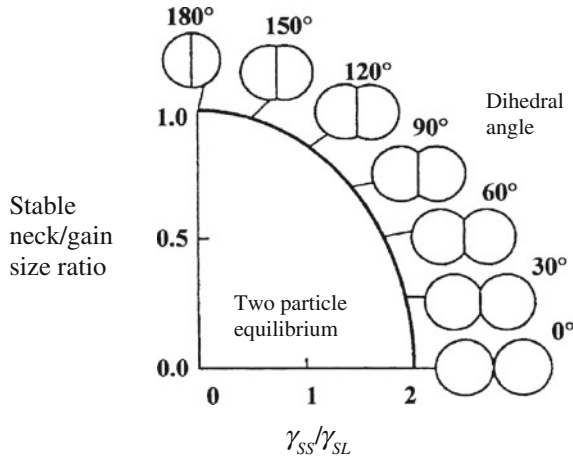


Fig. 5.31 Sketches of two particle contact geometries for various dihedral angles (and interfacial energy ratios). During liquid-phase sintering, the stable neck size to grain size ratio is determined by the equilibrium dihedral angle. Reproduced with permission from [74]. Copyright © 2001, Springer

Therefore, $\gamma_{SS}/\gamma_{SL} = 2$ is the critical value for complete penetration of the liquid into the grain boundary. If $\gamma_{SS}/\gamma_{SL} > 2$, Eq. (5.221) is not valid, indicating an entire penetration of the grain boundary. In other words, $\gamma_{SS}/\gamma_{SL} > 2$ corresponds to the fact that the total specific energy of the two solid–liquid interfaces is lower than that of the solid–solid interface. As a result, the overall energy of the system is decreased due to the penetration of the grain boundary by the liquid. The consequence of the complete penetration is the reduction in mechanical strength of the system.

Shape of the liquid and the grains are closely related to the dihedral angle. It has been accepted that the interfacial tensions at the three-grain junctions in a granular structure are in a balanced state, which determines the equilibrium distribution of second phases [75]. If the system is assumed to have no porosity, the shape of the liquid phase at equilibrium can be derived [61, 62, 76, 77]. Figure 5.32 shows two-dimensional shapes of a small quantity of liquid phase within the three-grain junctions with different dihedral angles [73]. With $\psi = 0$, the liquid entirely penetrates the grain boundary, so that there is no solid–solid contact. With increasing ψ , the penetration depth of the liquid phase along the grains decreases, while the

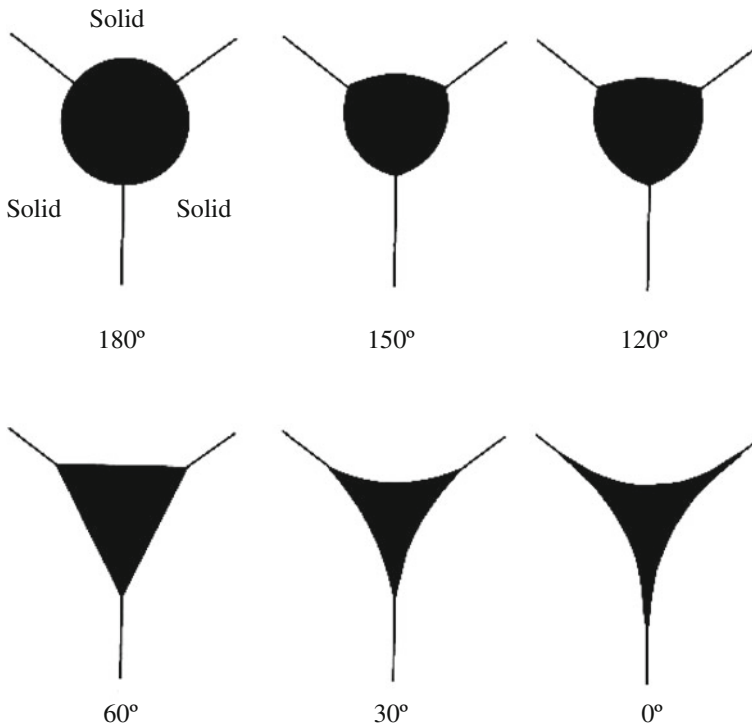


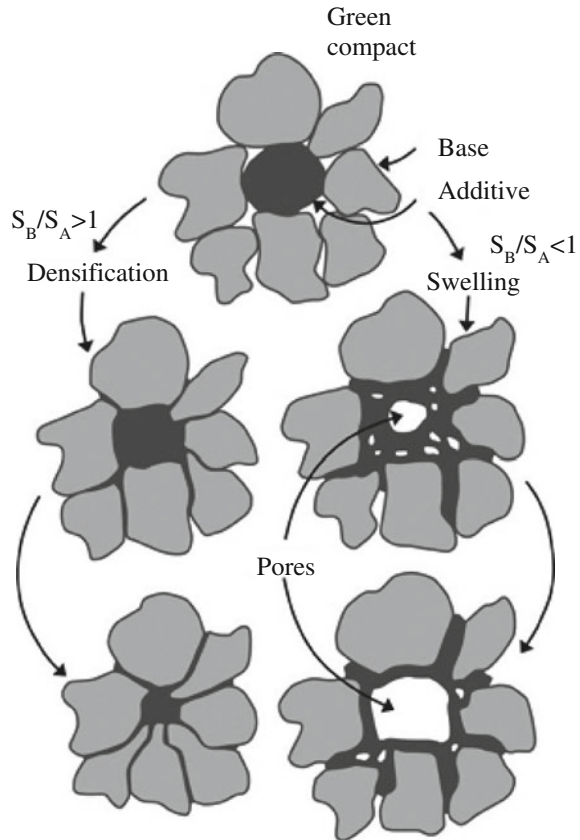
Fig. 5.32 At low liquid contents, the liquid phase forms pockets at the triple points where three-grain boundaries meet. The shape of the liquid pocket is dependent on the dihedral angle. Reproduced with permission from [73]. Copyright © 2009, Springer

amount of solid–solid contact, i.e., grain boundary area, increases accordingly. At $\psi = 60^\circ$, the liquid is still able to be present along the three-grain edges to a very low degree. Once ψ is larger than 60° , the liquid phase is entirely isolated at the junction region of the grains.

5.4.4.3 Effect of Solubility

In a solid–liquid two phase system, the solid can be dissolved in the liquid and the liquid can also be dissolved in the solid. A high solubility of the solid in the liquid will facilitate potentially a high mass transport rate through the liquid layer, which is the basic requirement of liquid-phase sintering. However, the dissolving of the liquid in the solid is totally prevented, otherwise the compact would be severely swelling due to the formation of transient liquid phases. The effect of solubility on densification and swelling of the compact is demonstrated schematically in Fig. 5.33 [73].

Fig. 5.33 Schematic diagram comparing the effects of solubility on densification or swelling during liquid-phase sintering, with S_A and S_B being solubility of the base and additive, respectively. Reproduced with permission from [73]. Copyright © 2009, Springer



The solubility is also affected by particle size of the compact. If the solubility is assumed to be equivalent to concentration, the relationship between the solute concentration and radius of the particle is given by

$$\ln\left(\frac{S}{S_0}\right) = \frac{2\gamma_{SL}\Omega}{kTa}, \quad (5.222)$$

where S is the solubility of the particle with a radius a in the liquid, S_0 is the equilibrium solubility of the solid in the liquid at planar interface, γ_{SL} is the specific energy of the solid–liquid interface, Ω is the atomic volume, k is the Boltzmann constant, and T is the absolute temperature. Equation (5.222) clearly indicates that the solubility increases with decreasing radius of the particle, due to the formation of a mass reservoir. This is the reason why matter transport always takes place from small particles to large particles. Such a process is known as Ostwald ripening. Additionally, rough regions of the particles have smaller radius of curvature and thus tend to be dissolved, whereas irregularities or defects between adjacent particles, such as pits and crevices, have negative radii of curvature, which have significantly low solubility, thus leading to precipitate in those regions.

5.4.4.4 Capillary Forces

When a liquid completely wets a solid, a compressive stress created due to the pressure deficit in the liquid that is defined by Eq. (5.218) will be applied to the particle. It has been shown that several factors, including contact angle, volume of the liquid, separation of the particles, and the particle size, have influences on the magnitude and nature of the compressive stress. The effects of these factors on the capillary force applied by the liquid can be evaluated by the idealized two-sphere model. The two-sphere particles in the model have same radius a , which are separated by a distance h by a liquid with a contact angle, as shown in schematically in Fig. 5.34 [73]. The shape of the liquid meniscus is called a nodoid. The analytical solution for the shape is in terms of elliptical integrals. Because the calculations of the meniscus shape and the capillary force are very complicated, it is assumed to have a circular shape, with the liquid meniscus being part of a circle. In this case, the pressure difference across the liquid–vapor meniscus is given by

$$\Delta p = \gamma_{LV} \left(\frac{1}{Y} - \frac{1}{r} \right), \quad (5.223)$$

where Y and r are the principal radii of curvature of the meniscus.

The force applied to the two spheres is the resultant contribution of two factors: (i) the pressure difference Δp across the liquid–vapor meniscus and (ii) the surface

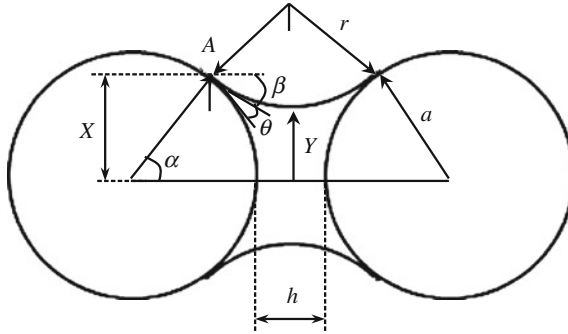


Fig. 5.34 Geometrical parameters for an idealized model of two spheres separated by a liquid bridge. Reproduced with permission from [73]. Copyright © 2009, Springer

tension of the liquid [61, 78, 79]. Therefore, at point A in Fig. 5.34, the force equation can be expressed as:

$$F = -\pi X^2 \Delta p + 2\pi X \gamma_{LV} \cos \beta, \quad (5.224)$$

where F is positive when the force is compressive.

Putting Δp Eq. (5.224) and letting $X = a \sin \alpha$, there is

$$F = -\pi a^2 \gamma_{LV} \left(\frac{1}{Y} - \frac{1}{r} \right) \sin^2 \alpha + 2\pi a \gamma_{LV} \sin \alpha \cos \beta. \quad (5.225)$$

The distance between the two spheres is given by

$$h = 2[r \sin \beta - a(1 - \cos \alpha)], \quad (5.226)$$

while the angles are related by the following expression:

$$\alpha + \beta + \theta = \pi/2. \quad (5.227)$$

By putting Eq. (5.227) into Eq. (5.226) and rearranging, there is

$$r = \frac{h + 2a(1 - \cos \alpha)}{2 \cos(\theta + \alpha)}. \quad (5.228)$$

The positive radius of curvature of the meniscus is given by

$$Y = a \sin \alpha - r[1 - \sin(\theta + \alpha)]. \quad (5.229)$$

Putting Eq. (5.228) into Eq. (5.229) yields

$$Y = a \sin \alpha - \frac{h + 2a(1 - \cos \alpha)}{2 \cos(\theta + \alpha)} [1 - \sin(\theta + \alpha)]. \quad (5.230)$$

The volume of the liquid bridge is thus given by

$$V = 2\pi(r^3 + r^2Y)\{\cos(\theta + \alpha) - [\pi/2 - (\theta + \alpha)]\} + \pi Y^2 r \cos(\theta + \alpha). \quad (5.231)$$

Equation (5.224) reveals that F is a function of the interparticle distance h for a given volume fraction of the liquid, which can be used to identify the inter-relationship between the contact angle and the efficiency of the particle rearrangement processes. It is found that a small contact angle is always desirable to achieve high degree of densification.

5.4.5 Grain Boundary Films

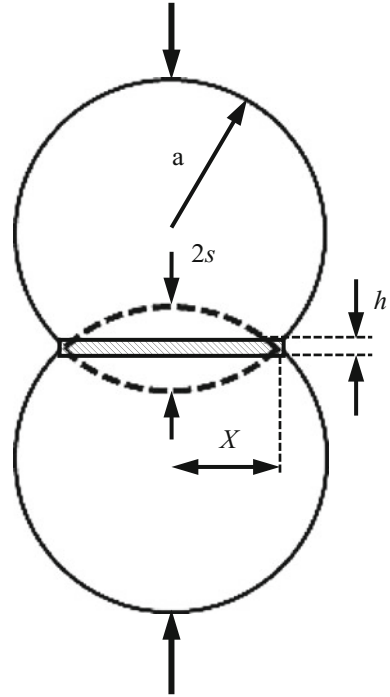
As discussed above, the presence of the liquid layer applies a compressive capillary force to the particles. The liquid layer evolves during the sintering process. Once the densification through the solution-precipitation mechanism starts, the thickness of the liquid layer gradually decreases with time. When the liquid capillary becomes too narrow for the liquid to flow, the solution-precipitation nearly stops. In this case, the rate of reduction in thickness of the liquid layer due to viscous flow will compete with the rate of densification. Therefore, because the flow of the liquid through the capillary is sufficiently slow, there is a thin layer of the liquid to be remained after densification, which has a thickness of 0.5–2 nm for most ceramics.

The theory for two flat plates separated by a liquid layer has been used to calculate the rate of reduction in thickness of the liquid layer that separates two-sphere particles during the liquid-phase sintering [80]. The rate of approach of two plates separated by a Newtonian viscous liquid is expressed as [81]

$$\frac{dh}{dt} = -\frac{2\pi h^5}{3\eta A^2 h_0^2} F, \quad (5.232)$$

where h is the thickness of the liquid layer at time t , h_0 is the initial thickness of the liquid layer, F is the compressive force applied to the plates, η is the viscosity of the liquid, and A is the contact area between the liquid and the plate. The application of Eq. (5.232) to the liquid-phase sintering is shown as the model in Fig. 5.35, in which two spheres are held together through a liquid bridge due to the capillary force [1]. In practice, it is more convenient to use the time that is taken by the liquid to be depleted. Letting $y = h/h_0$ and integrating Eq. (5.232), the time for y to be zero is given by

Fig. 5.35 Parameters of an idealized two-sphere model separated by a liquid layer of thickness h used to analyze the change in the thickness of the layer during sintering. Reproduced with permission from [1]. Copyright © 2003, CRC Press



$$t_f = \frac{3\eta A^2}{8\pi h_0^2 F} \left(\frac{1}{y^4} - 1 \right). \quad (5.233)$$

This equation indicates that the time for $y = 0$ is $t_f = \infty$. In other words, there will always be liquid to be remained between the particles. However, when the liquid layer is too thin, e.g., several nm, other effects, such as structural and chemical forces and charge interactions, will become dominant instead of viscous flow. The equilibrium thickness of the liquid layer between adjacent grains can be explained in terms of the balance between two forces, i.e., (i) the attractive van der Waals forces of the grains and (ii) the short-range repulsive forces due to the resistance to deformation of the liquid phase [82].

5.4.6 Mechanisms of Liquid-Phase Sintering

Similarly, the mechanisms of liquid-phase sintering can be described by dividing the process into three stages. The first stage involves the redistribution of the liquid

phase and rearrangement of the particles, the second stage is densification process through solution reprecipitation, while the third/last stage is known as Oswald ripening.

5.4.6.1 Stage 1

The capillary pressures developed during the liquid-phase sintering of fine particles forces the particles to rearrange as the viscosity of the system is still sufficiently low. Due to the presence of gradients in capillary pressure, the liquid phase will flow from regions with larger pores to regions with smaller pores, which is called liquid-phase redistribution, which has been confirmed experimentally in various systems [83]. Generally, the liquid phase fills from small pores to large pores.

A two-dimensional model of circular particles has been developed to describe the liquid redistribution behaviors, which assumes that the chemical potential of the liquid in all the pores in a given particle array is the same at equilibrium [84]. When an atom is located under the surface of a liquid–vapor meniscus, with an average radius of curvature r , its chemical potential is given by

$$\mu = \mu_0 + \frac{\gamma_{LV}\Omega}{r}, \quad (5.234)$$

where μ_0 is the chemical potential of the atom under a flat surface, γ_{LV} is the liquid–vapor surface energy, and Ω is the atomic volume. Therefore, the assumption of same chemical potential implies that the radius of the liquid menisci should be the same.

Figure 5.36 shows the two-dimensional model of liquid-phase redistribution, which is a regular array of circles with threefold coordinated pores and without shrinkage occurs [84]. The liquid phase can be redistributed in two ways. At very low volume fractions, the liquid phase is usually distributed evenly in the necks formed by the particles, as shown in Fig. 5.36a. There is a critical volume fraction, below which the distribution of the liquid phase is not affected the by the volume fraction and above which some of the pores are entirely filled with the liquid, as shown in Fig. 5.36b. This distribution is attributed to the requirement of minimizing the surface area. Therefore, the amount of the liquid phase located at the necks is not increased with increasing volume fraction of the liquid phase, because the increased amount of the liquid phase is all used to fill the pores. The range of the liquid volume for even distribution of the liquid in the necks decreases with increasing contact angle. Once some of the pores are filled, it is highly possible to form inhomogeneous liquid-phase distributions, such as that shown in Fig. 5.36c, which cannot be back to the homogeneous distribution.

Figure 5.37 shows the model with pores of both threefold and sixfold coordinations, which is used to mimic the inhomogeneously packed powder systems that are encountered in practical applications [84]. The results of free energy

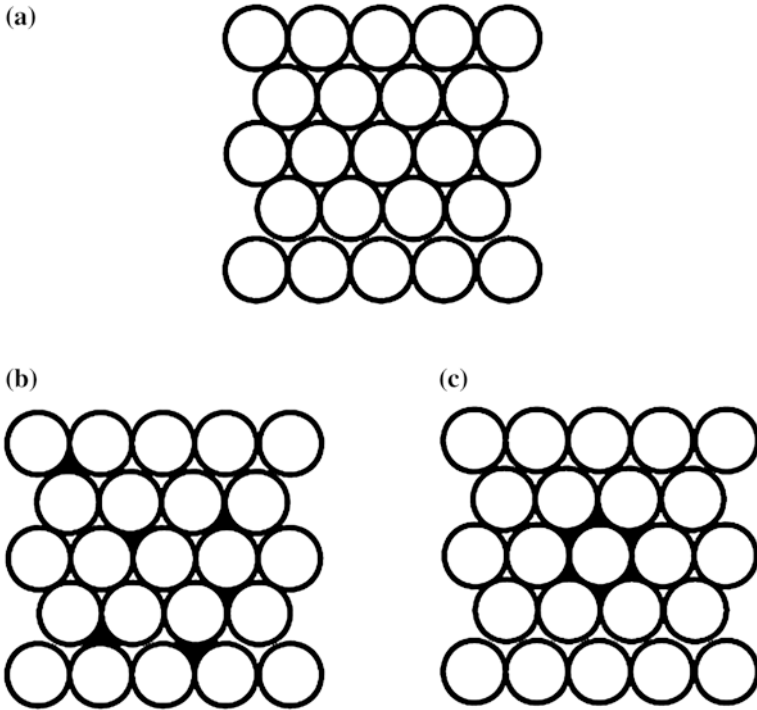


Fig. 5.36 Possible equilibrium configurations that can be adopted by a liquid in a close-packed two-dimensional array of particles with same size. **a** Isolated necks filled with liquid, **b** fraction of pores completely filled with liquid with homogeneous distribution, and **c** with inhomogeneous distribution. Reproduced with permission from [84]. Copyright © 1986, John Wiley & Sons

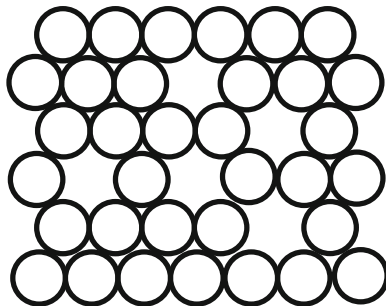


Fig. 5.37 Example of a two-dimensional arrangement of pores that contains threefold and sixfold coordinated pores. Reproduced with permission from [84]. Copyright © 1986, John Wiley & Sons

calculations, e.g., the fraction of the particles forming the sixfold coordinated pores as a function of the volume fraction of the liquid phase, can be used to describe the liquid-phase distribution behaviors.

It is found that the pores in the simple model are sequentially filled. In a real powder compact, the pores have a wide size distribution. In this case, the filling of the pores is started from those with smallest coordination number, because they have highest surface to volume ratios, so that largest solid–vapor interfacial areas are eliminated for a given volume of liquid. However, in practice, not all small pores can be filled, because the liquid might not be able to access to some of them. In addition, if particles to create the liquid phase are too large, huge voids will be left when the particles are molten. Therefore, in this respect, it is desirable to have powders with uniform particle size and homogeneous mixing of basic components and additives.

Once the liquid phase is formed, particles will start to rearrange almost immediately, which is finished in a few minutes. This rearrangement is responsible for the initial densification and affects the initial microstructure of the compact, which could have significant influence on further densification and microstructure development. Theoretical analysis of the rearrangement, especially for compacts with randomly packed particles, remains a challenge until now [85–88]. A simple kinetic relationship to describe the shrinkage as a function of time has been developed, by assuming that the surface tension forces to drive the densification are balanced by the viscous forces that resist the rearrangement, which is given by [89, 90]

$$\frac{\Delta L}{L_0} \sim t^{1+y}, \quad (5.235)$$

where ΔL is the change in length, L_0 is the original length, and y is a positive constant that is less than one.

The rearrangement process usually experiences two stages: primary rearrangement and secondary rearrangement. Primary rearrangement is a rapid process nearly immediately after the formation of the liquid phase, due to the surface tension forces of the liquid bridge applied to the particles. At this stage, if $\gamma_{SS}/\gamma_{SL} > 2$, the liquid can penetrate the grain boundaries, leading to fragmentation of the particles. The fragmented particles will further experience a rearrangement process, which is known as the secondary rearrangement. The secondary rearrangement is slower than the primary one, because it is dependent on the dissolving rate of the grain boundaries.

Full densification can be achieved through the rearrangement, if the content of the liquid phase is sufficiently high. The relative quantities of the solid and the liquid required for full densification is determined by the rearranged density of the particles. For a powder compact with a relative density of 60 %, i.e., 40 % porosity, if the particles rearrange to 64 % relative density through the rearrangement, full densification is achieved, when the liquid volume fraction is 36 %. Otherwise, further processes, e.g., solution-precipitation, are necessary to obtain full densification. In practice, rearrangement to full densification is quite rare, because the liquid-phase content is usually low, e.g., <5 vol.%. Moreover, the particles generally have irregular shapes.

5.4.6.2 Stage 2

With the gradual diminishment of the rearrangement process, solution precipitation starts to be dominant process, leading to further densification and coarsening. The densification and coarsening take place concurrently, which could be accompanied by accommodation in grain shape if the liquid phase has a small volume fraction. At the same time, coarsening and grain-shape accommodation are contributed by the coalescence of small grains in contact with large grains, besides the solution-precipitation. There are two models for densification: (i) contact flattening and (ii) Ostwald ripening.

Due to presence of the compressive capillary force, the solubility at the contact points between the particles is higher than that at other surfaces of the particles [89, 90]. Because of this difference in solubility, matter transport occurs from the contact points to other places, so as to form a flat contact region, as shown in Fig. 5.38 [1]. With increasing radius of the contact region, the stress along the interface decreases, so that the densification slows down. The rate of the matter transport is controlled by the slower one of the two mechanisms: (i) diffusion through the liquid layer and (ii) solution-precipitation via interface reaction.

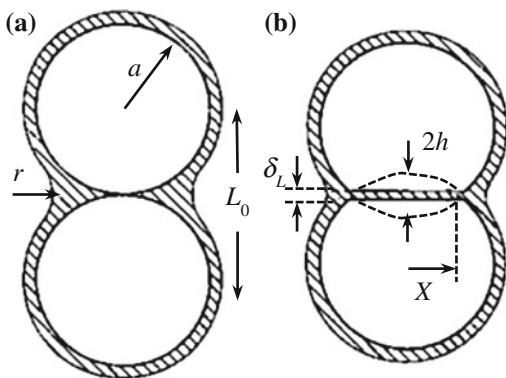
The rate control by diffusion through the liquid layer can be described by using the two spherical particle model. The two particles have the same radius a , if each sphere is dissolved away along the center-to-center line by a distance h to form a circular contact region with radius X , these parameters can be related through the following expression:

$$h \approx \frac{X^2}{2a}. \quad (5.236)$$

The volume of material removed from each sphere is given by $V \approx X^2h/2$, which is combined with Eq. (5.236), there is

$$V \approx \pi ah^2. \quad (5.237)$$

Fig. 5.38 Idealized two-sphere model for densification by contact flattening. Reproduced with permission from [1]. Copyright © 2003, CRC Press



Similar to the intermediate stage of solid-state sintering, the flux from the boundary per unit thickness is given by

$$J = 4\pi D_L \Delta C, \quad (5.238)$$

where D_L is the diffusion coefficient for the solute atom in the liquid and ΔC is the difference in solute concentration between the contact region, C and at flat stress-free surface, C_0 . If the thickness of the liquid layer is δ_L , the rate of consumption of the solid is given by

$$\frac{dV}{dt} = \delta_L J = 4\pi D_L \delta_L \Delta C. \quad (5.239)$$

If ΔC is small, there is

$$\frac{\Delta C}{C_0} = \frac{p\Omega}{kT}, \quad (5.240)$$

where p is the local stress applied to an atom, Ω is volume of the atom, k is the Boltzmann constant, and T is absolute temperature. The capillary pressure Δp due to a spherical pore in the liquid is given by Eq. (5.218), which is equivalent to an externally applied hydrostatic pressure so that the resulting interparticle force is equal to that produced by the liquid layer. Because the area of the contact region is smaller than that of the rest of the particles, the local pressure is magnified at the contact area. If a simple force balance is assumed, the local pressure p at the contact region is given by

$$pX^2 = k_1 \Delta p a^2, \quad (5.241)$$

where k_1 is a geometrical constant. When Eq. (5.241) is combined with Eqs. (5.218) and (5.236), there is

$$p = k_1 \frac{\gamma_{LV} a}{rh}. \quad (5.242)$$

It is assumed that the radius of the pore is proportional to the radius of the sphere, i.e., $r = k_2 a$, where k_2 is assumed to remain constant during sintering, Eq. (5.242) becomes

$$p = \frac{k_1 \gamma_{LV}}{k_2 h}. \quad (5.243)$$

According to Eqs. (5.238), (5.240) and (5.243), there is

$$\frac{dV}{dt} = \frac{4\pi k_1 D_L \delta_L C_0 \Omega \gamma_{LV}}{k_2 h k T}. \quad (5.244)$$

Because dV/dt is also equal to $(2\pi ah) dh/dt$ according to Eqs. (5.237) and (5.244) can also be rewritten as

$$h^2 dh = \frac{2k_1 D_L \delta_L C_0 \Omega \gamma_{LV}}{k_2 a k T} dt. \quad (5.245)$$

With the boundary condition of $h = 0$ at $t = 0$, integration of Eq. (5.245) yields

$$h = \left(\frac{6k_1 D_L \delta_L C_0 \Omega \gamma_{LV}}{k_2 a k T} \right)^{1/3} t^{1/3}. \quad (5.246)$$

Because there is $h/a = \Delta L/L_0 = -(1/3)\Delta V/V_0$ for small $\Delta L/L_0$, where $\Delta L/L_0$ and $\Delta V/V_0$ are the linear shrinkage and the volumetric shrinkage of the powder compact, respectively, the following expression can be obtained

$$-\frac{\Delta L}{L_0} = -\frac{1}{3} \frac{\Delta V}{V_0} = \left(\frac{6k_1 D_L \delta_L C_0 \Omega \gamma_{LV}}{k_2 a^4 k T} \right)^{1/3} t^{1/3}. \quad (5.247)$$

This equation indicates that, if the diffusion through the liquid layer is the rate-controlling step, the shrinkage increases as functions of time as $t^{1/3}$, starting particle size as $a^{-4/3}$ and thickness of the liquid layer as $\delta_L^{1/3}$.

If the interface reaction is the rate-controlling mechanism, in which the solid phase is dissolved into the liquid phase through reaction, the rate of mass transport is proportional to the contact area and the increased activity of the solid phase at the contact region due to the capillary pressure, which is given by

$$\frac{dV}{dt} = k_3 \pi X^2 (a - a_0) = 2\pi k_3 h a (C - C_0), \quad (5.248)$$

where k_3 is the rate constant of the phase boundary reaction, while a and a_0 are activities of the solid phase at the contact region and at flat surface, which are equal to their corresponding concentrations. In a similar way for the diffusion control, the shrinkage of the interface reaction control is given by

$$-\frac{\Delta L}{L_0} = -\frac{1}{3} \frac{\Delta V}{V_0} = \left(\frac{2k_1 k_3 C_0 \Omega \gamma_{LV}}{k_2 a^2 k T} \right)^{1/2} t^{1/2}. \quad (5.249)$$

This equation means that the shrinkage is proportional to $t^{1/2}$ and $1/a$.

The second mechanism of densification, i.e., densification accompanied by Ostwald ripening, can be described with an idealized model as shown in Fig. 5.39

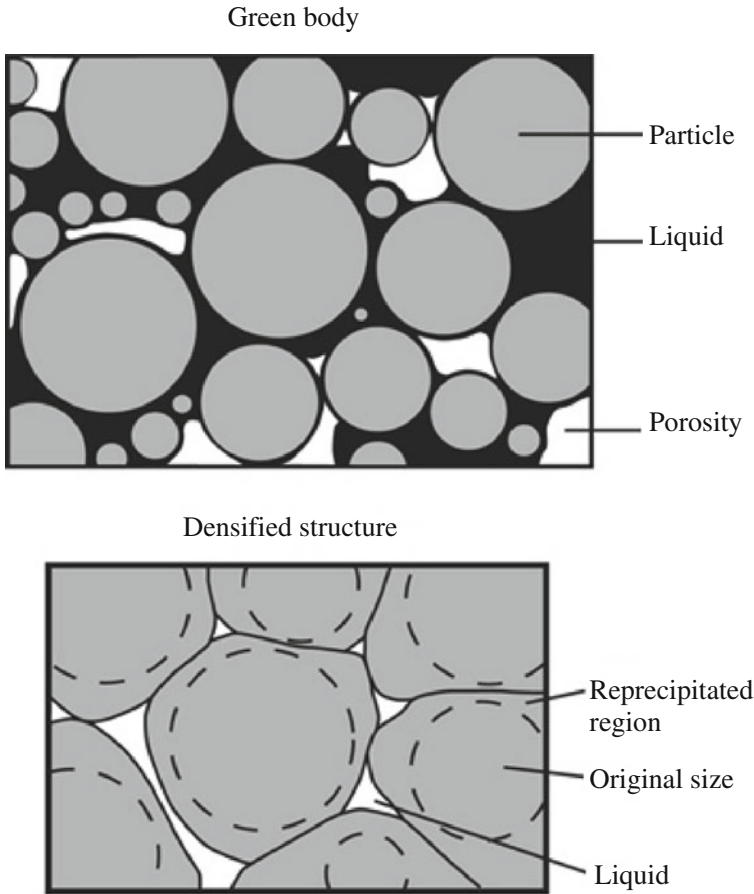


Fig. 5.39 Conceptual outline of the changes associated with solution-precipitation densification where both grain growth (Ostwald ripening) and grain-shape accommodation act to release liquid to fill residual pores. Reproduced with permission from [73]. Copyright © 2009, Springer

[73]. The smaller grains are dissolved into the liquid phase and then precipitate onto the larger grains from the contact points, thus facilitating shrinkage or densification. By assuming the Ostwald ripening to be diffusion controlled, the shrinkage rate can be expressed by the following expression [61]:

$$-\frac{\Delta L}{L_0} = -\frac{1}{3} \frac{\Delta V}{V_0} = \left(\frac{48D_L C_0 \Omega \gamma_{LV}}{a^3 kT} \right)^{1/3} t^{1/3}. \quad (5.250)$$

The content of the liquid phase plays a key role in determining whether there is grain-shape accommodation or not in a liquid-phase sintering. In a given system, there is a critical content of the liquid phase, below which grain-shape accommodation occurs, while above the grain-shape accommodation is absent. When the

content of the liquid phase is not sufficiently high to fill all the pores between the particles, if the particles have rounded or spheroidal shape, grain-shape accommodation takes place, which produces particles with polyhedral shapes with flat contact surfaces, so that the particles will have a more efficient packing. In this case, the liquid phase will be released from the well-packed regions to flow into the pores.

From energy point of view, grain-shape accommodation only occurs when the energy of the system is decreased because of it. For a given volume, the compact made of particles with polyhedral shapes has a larger surface area than that consisting of spherical particles. Therefore, only when the decreased interfacial energy caused by the filling of the pores is more than the increased interfacial energy due to the formation of the polyhedral particles, the grain-shape accommodation can take place. If the amount of the liquid phase is sufficiently high, the capillary pressure is too low to drive contact flattening. As a result, shape accommodation is much less pronounced, so that the particles remain to be spheroidal.

Coalescence-induced coarsening takes place when grains are pulled together due to the capillary force produced by the liquid phase [69, 91]. Coalescence usually experiences three steps: (i) contact formation between the grains, (ii) neck growth, and (iii) migration of the grain boundary, as shown schematically in Fig. 5.40 [73].

As shown in Fig. 5.41 [73], this curvature r depends on the dihedral angle ψ , and grain sizes G_1 and G_2 ($G_1 > G_2$) as

$$r = \cos\left(\frac{\psi}{2}\right) \left(\frac{G_1 G_2}{G_1 - G_2}\right) \quad (5.251)$$

Different mechanisms have been observed in coalescence, including solid-state grain boundary migration, liquid-film migration, and solution-precipitation through the liquid, as shown in Fig. 5.42 [73]. For small dihedral angle, liquid only partially penetrates the grain boundary. In this case, the grain boundary energy is increased during the movement of the boundary, so that coalescence is impeded. However, the small grain is absorbed by large grain through solution precipitation, which overcomes the energy barrier. For large dihedral angles, the liquid cannot penetrate the grain boundary, so that coalescence will become dominant. The larger the difference in size between the particles, the stronger the coalescence will be. Therefore, coalescence is most pronounced during the earlier period of the solution-precipitation process.

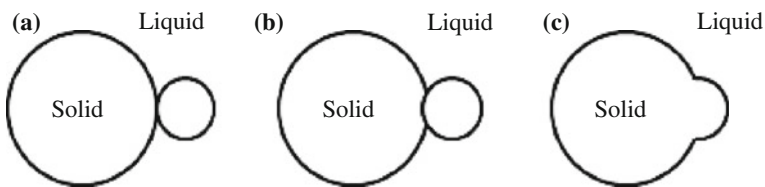


Fig. 5.40 Schematic diagram showing the grain growth by coalescence of small and large grains. Reproduced with permission from [73]. Copyright © 2009, Springer

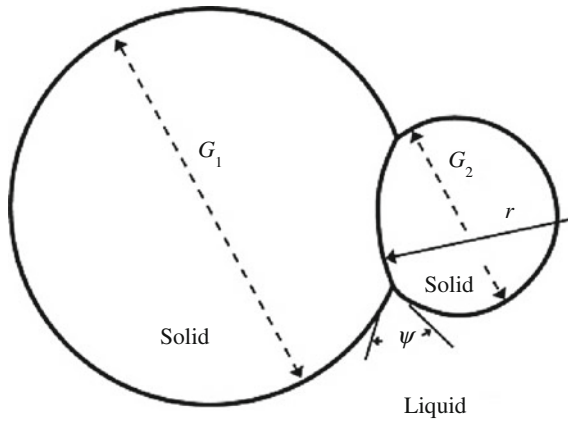


Fig. 5.41 The radius of curvature r of the grain boundary between contacting grains depends on the dihedral angle ψ and the grain size ratio (G_1/G_2). A large ratio induces a high curvature that aids rapid grain coalescence during liquid-phase sintering. Reproduced with permission from [73]. Copyright © 2009, Springer

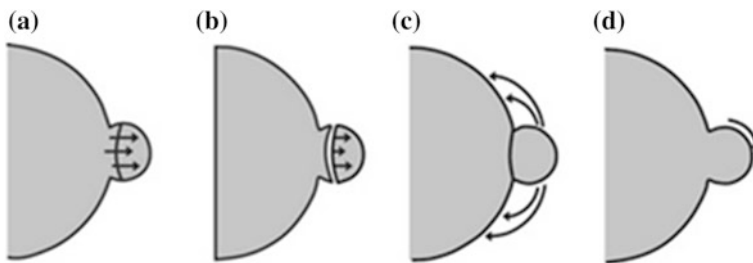


Fig. 5.42 Coalescence between two contacting grains by possible mechanisms: **a** solid-state grain boundary motion of curved grain boundaries, **b** liquid-film migration with diffusion across the film from the small to large grain, **c** solution reprecipitation from the small grain to the large grain through the surrounding liquid, and **d** small grain rotation to a lattice coincidence orientation where there is no grain boundary. Reproduced with permission from [73]. Copyright © 2009, Springer

Contact flattening is the first mechanism, which can be sketched in Fig. 5.43a [73]. A compressive force at the grain contacts from the wetting liquid pulls the grains together. This capillary stress causes preferential dissolution of solid at the contact point with reprecipitation at regions away from the contact. Densification results from the grain center-to-center motion [92]. The key step is solid diffusion in the liquid to areas away from the contact zone. For small grains, the contact zone stresses are quite large, so contact flattening tends to dominate LPS [93]. However, contact flattening does not explain grain growth and the decrease in the number of grains. When grain growth is inhibited there is less grain-shape accommodation [94–96].

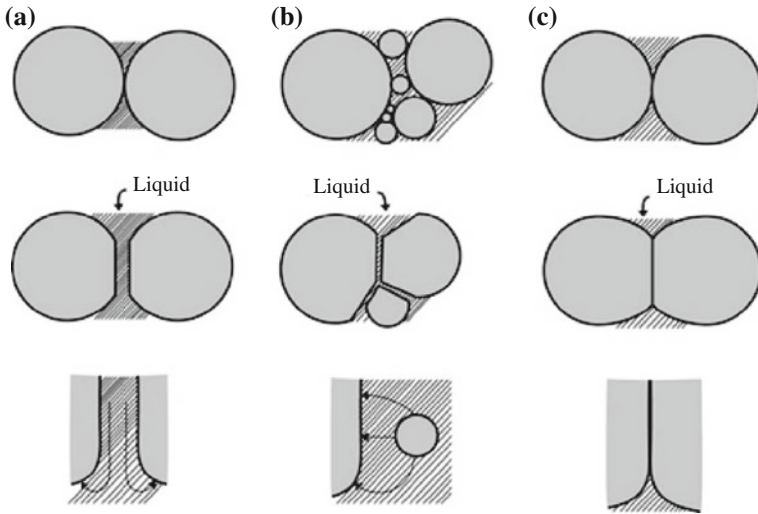


Fig. 5.43 The three mechanisms of grain-shape accommodation and neck growth during solution reprecipitation controlled densification of liquid-phase sintering: **a** contact flattening, **b** dissolution of small grains, and **c** solid-state bonding. Reproduced with permission from [73]. Copyright © 2009, Springer

The second densification mechanism involves dissolution of small grains with reprecipitation on large grains. Small grains disappear while large grains grow and undergo shape accommodation. Diffusion in the liquid is the controlling transport mechanism, as sketched in Fig. 5.43b [73]. This mechanism does not involve shrinkage, so it is not an explanation for densification, except that grain-shape accommodation enables better packing of the solid.

The third mechanism involves growth of the intergrain contact by diffusion along the liquid-wetted grain boundary [97–99], which is shown representatively in Fig. 5.43c [73]. The contact zone enlarges to change the grain shape with simultaneous shrinkage of the grains. This does not involve grain coarsening, but it does require a cooperative redistribution process of the mass deposited where the grain boundary intersects the liquid [37].

These three mechanisms are different in the source of the solid and in the detailed transport path, but they together can be used to explain grain-shape accommodation, grain growth, and densification. Grain growth takes place along with densification. Grain size and density tend to follow a common trajectory for most liquid-phase sintering systems, showing more rapid grain growth when pores are eliminated. Although neck growth is initially active, it is not sufficient to explain all microstructural developments. In addition, contact flattening and small grain dissolution are coupled to explain the microstructure and density progression that are typically observed during liquid-phase sintering.

5.4.6.3 Stage 3

At stage 3, densification slows down while coarsening becomes the dominant process. For $\gamma_{SS}/\gamma_{SL} > 2$, the grains are completely separated by the liquid layer. If $\psi > 0$, a rigid skeleton is gradually formed due to the solid–solid contacts. As a result, the isolated pores present in the liquid phase cannot be eliminated. The formation of the solid–solid contacts triggers solid-state sintering and coarsening. However, solution precipitation is still dominant over solid-state transport processes, because the matter transport through the liquid is much faster. Two events are dominant at this stage: (i) densification through pore filling and (ii) microstructural coarsening.

At low concentrations of the liquid phase, the elimination of isolated pores is continued at a reduced rate, due to the solution precipitation and grain-shape accommodation. If the volume fraction of the liquid is sufficiently high, the filling of the isolated pores could be discontinuous [95, 100]. In this case, grain growth, rather than grain-shape accommodation, is responsible for the filling of the pores.

As shown in Fig. 5.44, a large pore remains unfilled because of the preferential wetting of the necks between the particles [101]. As the grains continue to grow, the liquid phase reaches a favorable condition for filling the pore as determined by the curvature of the liquid–vapor meniscus [61, 76, 101]. From Fig. 5.45, the radius of curvature of the meniscus is given by [101]

$$r_m = a \frac{1 - \cos \alpha}{\cos \alpha}, \quad (5.252)$$

where a is the radius of the grain that is assumed to be spherical, so that r_m increases with increasing grain size. For zero contact angle, the critical point for pore filling to occur is that r_m is equal to the pore radius r , because after this point r_m cannot increase, so that the capillary pressure surrounding the pore will be reduced. Liquid is drawn from the numerous menisci at the surface of the sample, with very slight change in radii because only small volume of liquid is required to

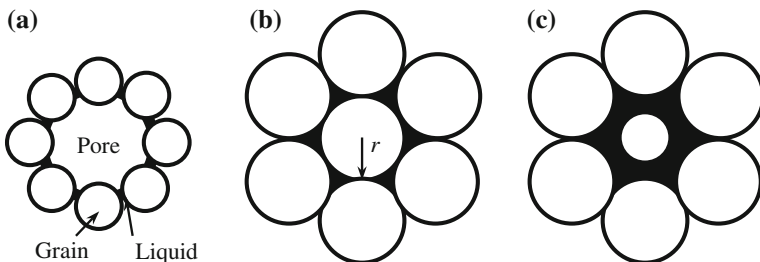


Fig. 5.44 Pore filling during the grain growth. A large pore is stable until grain growth increases the liquid meniscus radius sufficiently for capillary refilling of the pore. Reproduced with permission from [101]. Copyright © 1984, Springer

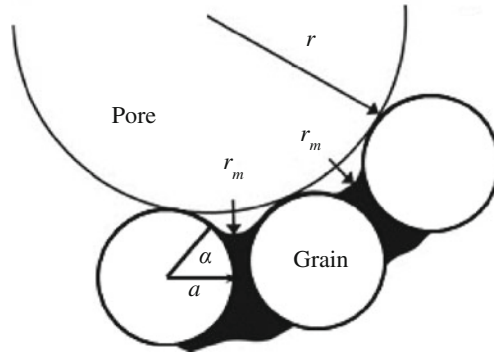


Fig. 5.45 Calculation model for pore refilling based on spherical grains surrounding the pore. Pore refilling depends on the liquid meniscus radius exceeding the pore radius. Reproduced with permission from [101]. Copyright © 1984, Springer

fill the pore. If the contact angle is larger than zero, r_m must be larger than r to facilitate the pore filling.

The most important theory to describe the Ostwald ripening mechanism for microstructural coarsening in the liquid-phase sintering is the Lifshitz-Slyozov-Wagner theory, usually known as the LSW theory. According to the LSW theory, the increase in the average grain size G with time t is given by

$$G^m = G_0^m + Kt, \quad (5.253)$$

where G_0 is the initial average grain size, K is a temperature-dependent constant, and the exponent m is dependent on the grain growth mechanism: $m = 3$ for diffusion through the liquid layer and $m = 2$ for interface reaction. For many ceramics, the exponent m is close to 3, implying that grain growth of ceramics is most likely governed by diffusion coarsening mechanism.

According to Arrhenius equation, the solubility of the solid in the liquid and the diffusion of the dissolved species through the liquid layer would increase with increasing temperature. Therefore, the rate of coarsening usually increases with increasing temperature. An increase in the dihedral angle leads to a decrease in the contact area between the solid and the liquid, so that the grain boundary area is increased accordingly. Obviously, matter transport through liquid is faster than through solid-state diffusion. Therefore, a reduction in the solid-liquid contact area means a reduced solution-precipitation process, thus leading to a reduction in the rate of grain growth.

Given that the content of the liquid phase is sufficiently high to isolate the grains/particles, decrease in volume fraction of the liquid phase means a decrease in thickness of the liquid-phase layer and thus shorter diffusion distance. Therefore, it is expected that the rate of matter transport would increase with decreasing content of the liquid phase, so that the rate of grain growth is increased correspondingly

[102]. Theories have been proposed to explain the dependence of grain growth on volume fraction of liquid phase, one of them is as follows [103, 104]:

$$K = K_i + \frac{K_L}{V_L^{2/3}}, \quad (5.254)$$

where K_i and K_L are the rate constant at infinite dilution, K_L is a microstructure-dependent parameter, and V_L is the volume fraction of the liquid phase.

5.4.7 Hot Pressing with Liquid Phase

Liquid-phase sintering has also been applied to ceramics with hot pressing. Because chemical potential of the atoms under the contact surfaces increases with increasing stress, matter transport from the contact regions to the pores is enhanced, so that the densification rate is increased [105].

The densification kinetics, with a solution-precipitation mechanism in which diffusion through the liquid layer is rate-controlling, can be described similarly by using the Coble's equation for grain boundary diffusion-controlled solid-state sintering, as discussed earlier. In this case, it is only necessary to replace the grain boundary thickness δ_{gb} , the grain boundary diffusion coefficient D_{gb} and the solid-vapor interfacial energy δ_{SV} with the thickness of the liquid layer δ_L , the diffusion coefficient for the solute in the liquid D_L and the liquid-vapor interfacial energy δ_{LV} , respectively. As the applied pressure p_a is much higher than the capillary pressure due to the liquid meniscus, the densification rate is given by

$$\frac{1}{\rho} \frac{d\rho}{dt} = \frac{AD_L\delta_L\Omega}{G^3kT} p_a\phi, \quad (5.255)$$

where A is a geometrical constant, which is equal to 47.5 for the intermediate stage of sintering, Ω is the atomic volume of the rate-controlling species, G is the grain size, k is the Boltzmann constant, T is the absolute temperature, and ϕ is the stress intensification factor.

5.4.8 Phase Diagrams in Liquid-Phase Sintering

Phase diagrams play an important role in selecting the powder compositions and sintering parameters for liquid-phase sintering. Because diagrams predict phases that are at equilibrium state, the reaction kinetics during liquid-phase sintering are often too fast for equilibrium to be achieved, so the phase diagrams should therefore serve only as a guide.

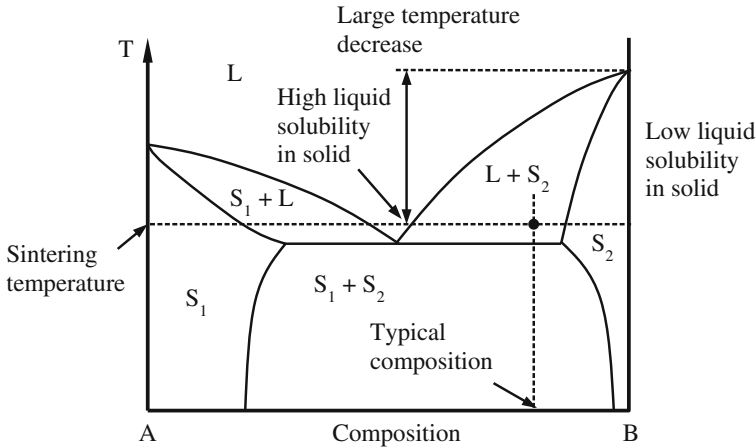


Fig. 5.46 Model binary phase diagram showing the composition and sintering temperature associated with liquid-phase sintering in the $L + S_2$ phase field. The favorable characteristics for liquid-phase sintering include a suppression of the melting temperature, high solid solubility in the liquid, and low liquid solubility in the solid. Reproduced with permission from [73]. Copyright © 2009, Springer

Figure 5.46 shows an idealized binary phase diagram, consisting of a major component, i.e., B and a liquid-producing additive, i.e., A , in which desirable composition and temperature characteristics for liquid-phase sintering have been indicated [73]. Importantly, there should be a large difference in melting temperature between the eutectic and the major component B . The system should have compositions away from the eutectic point, so that the volume of the liquid phase is increased gradually with temperature, so as to avoid the formation of all the liquid in the short time span. Usually, the sintering temperature is slightly above the eutectic temperature, which the composition of the system is in the $(L + S_2)$ region, e.g., the dot shown in the figure.

5.4.9 Activated Sintering and Vitrification

When powder compacts containing small amounts of a eutectic-forming additive are sintered, enhanced densification rates, as compared with that of the pure powder, could be observed well before the eutectic temperature is reached. This effect is generally known as activated sintering, which has been observed in various materials with a wide range of additives [106–110]. Currently, there is no clear difference in principles involved in activated sintering and liquid-phase sintering from the activated systems with a small content of additives, e.g., <1 wt%, at a sintering temperature below the eutectic temperature [111]. Although the mechanism of activated sintering has not been clearly identified, if the additive segregates

at the grain boundaries, enhanced subeutectic densification rates could be observed, grain boundary transport rates are enhanced by the additive. The additive should also be able to form low-melting phases or eutectic with the major component and the major component should have a high solubility in the additive. When the grain boundaries are rich in the eutectic-forming additive, their transport rates will be enhanced, because of their relative melting points. For example, when ZnO was added with Bi₂O₃, Bi-enriched intergranular amorphous films with a thickness of ~ 1 nm thick were formed. Because these amorphous films accelerated mass transport, activated sintering was triggered [109].

If the densification of liquid-phase sintering is achieved due to the viscous flow of a liquid that is able to fill up the pore spaces between the solid grains, it is called vitrification [112–114]. The driving force for vitrification is the reduction of solid–vapor interfacial energy, because the flow of the liquid covers the surfaces of the solid. Traditional clay-based ceramics are usually densified through vitrification. However, it is very unlikely to be observed in the processing of transparent ceramics, because the content of liquid phase must be controlled to a limited level.

5.5 Concluding Remarks

Matter transport during the sintering of polycrystalline ceramics takes place through a thermally activated process, known as diffusion, with various paths in the solid, corresponding to the different mechanisms of diffusion, i.e., (i) lattice, (ii) grain boundary, and (iii) surface diffusion. The rate of atomic or ionic diffusion is dependent on temperature and the concentration of defects in the solid. The concentration of defects can be controlled by doping or introducing impurities. Mass transport during the sintering involves the flux of atoms and ions or the counterflow of vacancies. The flux of the diffusing species is attributed to the gradients in concentration in particular or in the chemical potential in general. The rate of sintering and other mass transport processes are controlled by the slowest diffusing species along its fastest path.

The sintering phenomena of polycrystalline ceramics are very complex, with mass transport having at least six paths that determine the mechanisms of sintering. There are also densifying mechanisms and nondensifying mechanisms. Analytical models have been developed to describe the dependence of the sintering rate on various variables, including particle size, temperature, and external pressure. However, due to the drastic simplification used in their development, the models can provide only a qualitative description of sintering. Numerical simulations are more effective in analyzing the complexities of sintering.

The presence of liquid phase could enhance densification through grain rearrangement and faster matter transport. Liquid-phase sintering involves three overlapping stages, including (i) rearrangement of grains/particles, (ii) solution precipitation, and (iii) Ostwald ripening. The efficiency of liquid-phase sintering is

dependent on several parameters, e.g., low contact angle, low dihedral angle, high solid solubility of the solid in the liquid, homogeneous packing of the particulate solid, uniform distribution of the liquid-producing additive, and fine particle size. Activated sintering and vitrification are unlikely encountered in transparent ceramics due to the limited quantity of additives.

References

1. Rahaman MN (2003) Ceramic processing and sintering, 2nd edn. CRC Press, New York
2. Kemethmueller S, Hagymasi M, Stiegelschmitt A, Roosen A (2007) Viscous flow as the driving force for the densification of low-temperature co-fired ceramics. *J Am Ceram Soc* 90:64–70
3. Pino-Munoz D, Bruchon J, Drapier S, Valdivieso F (2014) Sintering at particle scale: an Eulerian computing framework to deal with strong topological and material discontinuities. *Arch Comput Methods Eng* 21:141–187
4. Chaim R, Levin M, Shlayer A, Estournes C (2008) Sintering and densification of nanocrystalline ceramic oxide powders: a review. *Adv Appl Ceram* 107:159–169
5. Fang ZZ, Wang H (2008) Densification and grain growth during sintering of nanosized particles. *Int Mater Rev* 53:326–352
6. German RM (2002) Computer modeling of sintering processes. *Int J Powder Metall* 38:48–66
7. Green DJ, Guillon O, Roedel J (2008) Constrained sintering: a delicate balance of scales. *J Eur Ceram Soc* 28:1451–1466
8. Hareesh US, Johnson R (2007) Rate controlled sintering: a unique concept for microstructural control. *Trans Indian Ceram Soc* 66:157–166
9. Lu K (2008) Sintering of nanoceramics. *Int Mater Rev* 53:21–38
10. Pan JZ (2003) Modelling sintering at different length scales. *Int Mater Rev* 48:69–85
11. Wakai F (2006) Modeling and simulation of elementary processes in ideal sintering. *J Am Ceram Soc* 89:1471–1484
12. Bordia RK, Scherer GW (1988) On constrained sintering, 1. Constitutive model for a sintering body. *Acta Metall* 36:2393–2397
13. Bordia RK, Scherer GW (1988) On constrained sintering, 2. Comparison of constitutive models. *Acta Metall* 36:2399–2409
14. Bordia RK, Scherer GW (1988) On constrained sintering, 3. Rigid inclusions. *Acta Metall* 36:2411–2416
15. Dudnik EV, Zaitseva ZA, Shevchenko AV, Lopato LM (1995) Sintering of ultradisperse powders based on zirconium dioxide (review). *Powder Metall Met Ceram* 34:263–271
16. Haviar M (1985) The mechanisms involved in solid-phase sintering. *Silikaty* 29:363–377
17. Kuang X, Carotenuto G, Nicolais L (1997) A review of ceramic sintering and suggestions on reducing sintering temperatures. *Adv Perform Mater* 4:257–274
18. Olevsky EA (1998) Theory of sintering: from discrete to continuum. *Mater Sci Eng R-Rep* 23:41–100
19. Brown AM, Ashby MF (1980) Correlations for diffusion constants. *Acta Metall* 28:1085–1101
20. Kuczynski GC (1949) Self-diffusion in sintering of metallic particles. *Trans Am Inst Min Metall Eng* 185:169–178
21. Shaler AJ, Udin H, Kuczynski GC, Bever M (1949) Self-diffusion in sintering metallic particles—discussion. *Trans Am Inst Min Metall Eng* 185:896–897
22. Gordon RS (1973) Mass-transport in diffusional creep of ionic solids. *J Am Ceram Soc* 56:147–152

23. Hg W (1973) Gordon RS. Effect of oxygen partial-pressure on creep of polycrystalline Al_2O_3 doped with Cr, Fe or Ti. *J Am Ceram Soc* 56:140–147
24. Carter CB, Norton MG (2007) *Ceramics materials: science and engineering*. Springer, Berlin
25. Herring C (1950) Effect of change of scale on sintering phenomena. *J Appl Phys* 21:301–303
26. Johnson KL, Kendall K, Roberts AD (1971) Surface energy and contact of elastic solids. *Proc Ro Soc London Ser A-Math Phys Sci* 324:301–313
27. Coble RL (1961) Sintering crystalline solids. 1. Intermediate and final state diffusion model. *J Appl Phys* 32:787–793
28. Coble RL (1961) Sintering crystalline solids. 2. Experimental test of diffusion models in powder compacts. *J Appl Phys* 32:793–799
29. Johnson DL, Cutler IB (1963) Diffusion sintering. 1. Initial stae sintering models and their application to shrinkage of powder compacts. *J Am Ceram Soc* 46:541–545
30. Johnson DL, Cutler IB (1963) Diffusion sintering. 2. Initial sintering kinetics of alumina. *J Am Ceram Soc* 46:545–550
31. Coble RL (1958) Initial sintering of alumina and hematite. *J Am Ceram Soc* 41:55–62
32. Kuczynski GC (1949) Study of the sintering of glass. *J Appl Phys* 20:1160–1163
33. Ashby MF (1974) First report on sintering diagrams. *Acta Metall* 22:275–289
34. Swinkels FB, Ashby MF (1981) Overview 11—A 2nd report on sintering diagrams. *Acta Metall* 29:259–281
35. Coble RL (1973) Effects of particle-size distribution in initial-stage sintering. *J Am Ceram Soc* 56:461–466
36. Johnson DL (1969) New method of obtaining volume grain-boundary and surface diffusion coefficients from sintering data. *J Appl Phys* 40:192–200
37. Swinkels FB, Ashby MF (1980) Role of surface redistribution in sintering by grain-boundary transport. *Powder Metall* 23:1–7
38. Coleman SC, Beere WB (1975) Sintering of open and closed porosity in UO_2 . *Phil Mag* 31:1403–1413
39. Nichols FA, Mullins WW (1965) Morphological changes of a surface of revolution due to capillarity-induced surface diffusion. *J Appl Phys* 36:1826–1835
40. Bross P, Exner HE (1979) Computer-simulation of sintering processes. *Acta Metall* 27:1013–1020
41. Exner HE, Bross P (1979) Material transport rate and stress-distribution during grain-boundary diffusion driven by surface-tension. *Acta Metall* 27:1007–1012
42. Ross JW, Miller WA, Weatherly GC (1981) Dynamic computer-simulation of viscous-flow sintering kinetics. *J Appl Phys* 52:3884–3888
43. Ross JW, Miller WA, Weatherly GC (1982) Computer-simulation of sintering in powder compacts. *Acta Metall* 30:203–212
44. Svoboda J, Riedel H (1995) Quasi-equilibrium sintering for coupled grain-boundary and surface-diffusion. *Acta Metall Mater* 43:499–506
45. Svoboda J, Riedel H (1995) New solution describing the formation of interparticle necks in solid-state sintering. *Acta Metall Mater* 43:1–10
46. Jagota A, Dawson PR (1988) Micromechanical modeling of powder compacts 1. Unit problems for sintering and traction induced deformation. *Acta Metall* 36:2551–2561
47. Jagota A, Dawson PR (1988) Micromechanical modeling of powder compacts 2. Truss formulation of discrete packings. *Acta Metall* 36:2563–2573
48. Jagota A, Dawson PR (1990) Simulation of the viscous sintering of two particles. *J Am Ceram Soc* 73:173–177
49. Djohari H, Martinez-Herrera JI, Derby JJ (2009) Transport mechanisms and densification during sintering: I. Viscous flow versus vacancy diffusion. *Chem Eng Sci* 64:3799–3809
50. Martinezherrera JI, Derby JJ (1995) Viscous sintering of spherical-particles via finite-element analysis. *J Am Ceram Soc* 78:645–649
51. Jagota A (1994) Simulation of the viscous sintering of coated particles. *J Am Ceram Soc* 77:2237–2239

52. Pejovnik S, Smolej V, Susnik D, Kolar D (1979) Statistical-analysis of the validity of sintering equations. *Powder Metall Int* 11:22–23
53. Coble RL (1970) Diffusion models for hot pressing with surface energy and pressure effects as driving forces. *J Appl Phys* 41:4798–4807
54. Herring C (1950) Diffusional viscosity of a polycrystalline solid. *J Appl Phys* 21:437–445
55. Coble RL (1963) A model for boundary diffusion controlled creep in polycrystalline materials. *J Appl Phys* 34:1679–1682
56. Paladino AE, Coble RL (1963) Effect of grain boundaries on diffusion-controlled processes in aluminum oxide. *J Am Ceram Soc* 46:133–136
57. Harmer MP, Brook RJ (1980) The effect of MgO additions on the kinetics of hot-pressing in Al_2O_3 . *J Mater Sci* 15:3017–3024
58. Beere W (1975) Diffusional flow and hot-pressing—study on MgO. *J Mater Sci* 10:1434–1440
59. Vieira JM, Brook RJ (1984) Kinetics of hot-pressing—the semilogarithmic law. *J Am Ceram Soc* 67:245–249
60. Vieira JM, Brook RJ (1984) Hot-pressing high-purity magnesium-oxide. *J Am Ceram Soc* 67:450–454
61. Beere W (1975) Unifying theory of stability of penetrating liquid-phase and sintering pores. *Acta Metall* 23:131–138
62. Beere W (1975) Second stage sintering kinetics of powder compacts. *Acta Metall* 23:139–145
63. Helle AS, Easterling KE, Ashby MF (1985) Hot-isostatic pressing diagrams—new development. *Acta Metall* 33:2163–2174
64. Oyane M, Shima S, Tabata T (1978) Consideration of basid equations and their application in forming of metal powders and porous metals. *J Mech Working Technol* 1:325–341
65. Shima S, Oyane M (1976) Pasticity theory for porous metals. *Int J Mech Sci* 18:285–291
66. Dutton RE, Shamasundar S, Semiatin SL (1995) Modeling the hot consolidation of ceramic and metal powders. *Metall Mater Trans A-Phys Metall Mater Sci* 26:2041–2051
67. Kingery WD, Niki E, Narasimhan MD (1961) Sintering of oxide and carbide-meal compositions in presence of a liquid phase. *J Am Ceram Soc* 44:29–35
68. Huppmann WJ, Riegger H (1977) Liquid-phase sintering of model system W-Ni. *Int J Powder Metall* 13:243–247
69. Kaysser WA, Takajo S, Petzow G (1984) Particle growth by coalescence during liquid-phase sintering of Fe-Cu. *Acta Metall* 32:115–122
70. Chu MY, Rahaman MN, Dejonghe LC, Brook RJ (1991) Effect of heating rate on sintering and coarsening. *J Am Ceram Soc* 74:1217–1225
71. Raj R, Ashby MF (1975) Intergranular fracture at elevated-temperature. *Acta Metall* 23:653–666
72. German RM (1990) Supersolidus liquid-phase sintering, 1. Process review. *Int J Powder Metall* 26:23–34
73. German RM, Suri P, Park SJ (2009) Review: liquid phase sintering. *J Mater Sci* 44:1–39
74. Liu JX, German RM (2001) Microstructure effect on dihedral angle in liquid-phase sintering. *Metall Mater Trans A-Phys Metall Mater Sci* 32:165–169
75. Smith CS (1948) Grains, phases, and interfaces—an interpretation of microstructure. *Trans Am Inst Min Metall Eng* 175:15–51
76. Park HH, Kwon OJ, Yoon DN (1986) The critical grain-size for liquid flow into pores during liquid-phase sintering. *Metall Trans A-Phys Metall Mater Sci* 17:1915–1919
77. Park HH, Yoon DN (1985) Effect of dihedral angle on the morphology of grains in a matrix phase. *Metall Trans A-Phys Metall Mater Sci* 16:923–928
78. Hwang KS, German RM, Lenel FV (1987) Capillary forces between spheres during agglomeration and liquid-phase sintering. *Metall Trans A-Phys Metall Mater Sci* 18:11–17
79. Zovas PE, German RM, Hwang KS, Li CJ (1983) Activated and liquid-phase sintering—process and problems. *J Metals* 35:28–33

80. Lange FF (1982) Liquid-phase sintering—are liquids squeezed out from between compressed particles. *J Am Ceram Soc* 65:C23–C24
81. Eley DD (1961) Adhesion. Oxford University Press, Oxford
82. Clarke DR (1987) On the equilibrium thickness of intergranular glass phases in ceramic materials. *J Am Ceram Soc* 70:15–22
83. Kwon OJ, Yoon DN (1981) Closure of isolated pores in liquid-phase sintering of W-Ni. *Int J Powder Metall* 17:127–134
84. Shaw TM (1986) Liquid redistribution during liquid-phase sintering. *J Am Ceram Soc* 69:27–34
85. Huppmann WJ, Riegger H (1975) Modeling of rearrangement processes in liquid-phase sintering. *Acta Metall* 23:965–971
86. Huppmann WJ, Riegger H, Kaysser WA, Smolej V, Pejovnik S (1979) Elementary mechanisms of liquid-phase sintering. 1. Rearrangement. *Zeitschrift Fur Metallkunde* 70:707–713
87. Huppmann WJ (1979) Elementary mechanisms of liquid-phase sintering 2. Solution-reprecipitation. *Zeitschrift Fur Metallkunde* 70:792–797
88. Lee SM, Chaix JM, Martin CL, Allibert CH, Kang SJL (1999) Computer simulation of particle rearrangement in the presence of liquid. *Metals Mater Korea* 5:197–203
89. Kingery WD (1959) Densification during sintering in the presence of a liquid phase 1. Theory. *J Appl Phys* 30:301–306
90. Kingery WD, Narasimhan MD (1959) Densification during sintering in the presence of a liquid phase 2. Experimental. *J Appl Phys* 30:307–310
91. Takajo S, Kaysser WA, Petzow G (1984) Analysis of particle growth by coalescence during liquid-phase sintering. *Acta Metall* 32:107–113
92. Marion JE, Hsueh CH, Evans AG (1987) Liquid-phase sintering of ceramics. *J Am Ceram Soc* 70:708–713
93. Eremenko VN, Naidich YV, Lavrinenko IA (1985) Liquid phase sintering. Consultants Bureau, New York
94. Yoon DN, Huppmann WJ (1979) Grain-growth and densification during liquid-phase sintering of W-Ni. *Acta Metall* 27:693–698
95. Yoon DN, Huppmann WJ (1979) Chemically driven growth of tungsten grains during sintering in liquid nickel. *Acta Metall* 27:973–977
96. Kaysser WA, Zivkovic M, Petzow G (1985) Shape accommodation during grain-growth in the presence of a liquid-phase. *J Mater Sci* 20:578–584
97. Gessinge GH, Fischmei HF (1972) Modified model for sintering of tungsten with nickel additions. *J Less-Common Metals* 27:129–141
98. Gessinge GH, Fischmei HF, Lukas HL (1973) Model for second-stage liquid-phase sintering with a partially wetting liquid. *Acta Metall* 21:715–724
99. Gessinge GH, Fischmei HF, Lukas HL (1973) Influence of a partially wetting second-phase on sintering of solid particles. *Powder Metall* 16:119–127
100. Kang SJL, Kim KH, Yoon DN (1991) Densification and shrinkage during liquid-phase sintering. *J Am Ceram Soc* 74:425–427
101. Park HH, Cho SJ, Yoon DN (1984) Pore filling process in liquid-phase sintering. *Metall Trans A-Phys Metall Mater Sci* 15:1075–1080
102. Kang TK, Yoon DN (1978) Coarsening of tungsten grain in liquid nickel-tungsten matrix. *Metall Trans A-Phys Metall Mater Sci* 9:433–438
103. German RM (1995) Microstructure of the gravitationally settled region in a liquid-phase sintered dilute tungsten heavy alloy. *Metall Mater Trans A-Phys Metall Mater Sci* 26: 279–288
104. Liu YX, Heaney DF, German RM (1995) Gravity-induced solid grain packing during liquid-phase sintering. *Acta Metall Mater* 43:1587–1592
105. Bowen LJ, Weston RJ, Carruthers TG, Brook RJ (1978) Hot-pressing and alpha-beta phase-transformation in silicon nitride. *J Mater Sci* 13:341–350

106. Hu SC, Dejonghe LC (1981) Pre-eutectic densification in $\text{MgF}_2\text{-CaF}_2$. *Am Ceram Soc Bull* 60:385
107. Hu SC, De Jonghe LC (1983) Pre-eutectic densification in $\text{MgF}_2\text{-CaF}_2$. *Ceram Int* 9:123–126
108. Wu SJ, Dejonghe LC, Rahaman MN (1985) Subeutectic densification and second-phase formation in $\text{Al}_2\text{O}_3\text{-CaO}$. *J Am Ceram Soc* 68:385–388
109. Luo J, Wang HF, Chiang YM (1999) Origin of solid-state activated sintering in Bi_2O_3 -doped ZnO . *J Am Ceram Soc* 82:916–920
110. German RM, Munir ZA (1976) Enhanced low-temperature sintering of tungsten. *Metall Trans A-Phys Metall Mater Sci* 7:1873–1877
111. Zovas PE, German RM, Hwang KS, Li CJ (1983) Activated and liquid-phase sintering—progress and problems. *J Metals* 35:28–33
112. Shakhparonov MI, Durov VA (1979) Theory of collective reaction in liquid-phase 5. Collective reaction and vitrification. *Zh Fiz Khim* 53:2451–2455
113. Ruiz-Valdes JJ, Gorokhovskiy AV, Escalante-Garcia JI (2005) Vitrification in the $\text{BaO-B}_2\text{O}_3\text{-Al}_2\text{O}_3\text{-TiO}_2$ system containing small admixtures of PbO . *J Non-Cryst Solids* 351:2036–2041
114. Yang HT, Yang GT, Yuan RZ (1998) Vitrification and devitrification of MgO during sintering of $\text{Si}_3\text{N}_4\text{-MgO-CeO}_2$ ceramics. *Mater Chem Phys* 57:178–181